

Copyright
by
Shrawan Singhal
2012

**The Dissertation Committee for Shrawan Singhal Certifies that this is the approved
version of the following dissertation:**

Jet and Coat of Adaptive Sustainable Thin Films

Committee:

S. V. Sreenivasan, Supervisor

Roger T. Bonnecaze

Ofodike A. Ezekoye

Wei Li

C. Grant Willson

Jet and Coat of Adaptive Sustainable Thin Films

by

Shrawan Singhal, BTech, MSE

Dissertation

Presented to the Faculty of the Graduate School of

The University of Texas at Austin

in Partial Fulfillment

of the Requirements

for the Degree of

Doctor of Philosophy

The University of Texas at Austin

August 2012

Acknowledgements

I am grateful for the constant encouragement and support of my supervisor and mentor, Prof. S.V. Sreenivasan. I could not thank him less for his sound advice on technical matters. At the same time, his focus towards solving real problems served as a constant source of inspiration. I am also grateful to all my doctoral committee members, who have provided me with valuable insight from their diverse perspectives.

I also acknowledge the help and support of my colleagues in Prof. Sreenivasan's group, namely, Vik Singh, who has lent his advice on experimental matters and also helped out with SEM metrology and metal deposition, and Andy Yin, whose knowledge of the ins-and-outs of the roll-roll tool has been used to good effect! I would also like to thank Mike Miller, Sean Ahn, John Graves and Jason Farmer at Molecular Imprints, Inc., for machine training and supplying valuable equipment like the flexible superstrate and substrates, helping with substrate reclaiming as well as allowing me to bother them at any time during their busy schedules with not-so-urgent matters.

I am also extremely lucky to have had the company of some wonderful friends. They have motivated me and egged me on when it seemed all too easy to give up. I could not also be more grateful to my dearest parents for their selfless love and blessings. I know it was difficult for them to send me 10,000 miles away from home to pursue this degree. I am thankful to them for continuing to have faith in me, without expecting anything in return. Lastly, I express my most heartfelt gratitude to my lovely wife, who sacrificed her career for the sake of mine, and whose unending affection, support and belief in me has pushed me towards my goal.

This research was supported in part by the National Science Foundation Scalable Nanomanufacturing Program (NSF Contract No. ECCS-1120823), the DARPA Tip-Based Nanofabrication Program (DARPA Contract No. N66001-08-C-2040), the Texas Emerging Technology Funds Program, and by Molecular Imprints, Inc., Austin, Texas. The experimental work was conducted at Molecular Imprints Inc., Austin, TX and the Microelectronics Research Center (MRC) at The University of Texas at Austin, which is a member of the National Nanotechnology Infrastructure Network (NNIN).

Jet and Coat of Adaptive Sustainable Thin Films

Shrawan Singhal, PhD

The University of Texas at Austin, 2012

Supervisor: S. V. Sreenivasan

Deposition of nanoscale thickness films is ubiquitous in micro- and nano-scale device manufacturing. Current techniques such as spin-coating and chemical vapor deposition are designed to create only uniform thin films, and can be wasteful in material consumption. They lack the ability to adaptively prescribe desired film thickness profiles. This dissertation presents a novel inkjet-based zero-waste polymer deposition process referred to as Jet and Coat of Adaptive Sustainable Thin Films or J-CAST. The core of this process is built on an experimentally validated multi-scale fluid evolution model, based on extensions of lubrication theory. This model involves a nano-scale fluid film sandwiched between two flat plates: a compliant superstrate and a rigid substrate, with spatial topography on both surfaces. Accounting for the flexural elasticity of the compliant superstrate, and describing the temporal evolution of the fluid film in the presence of different boundary conditions reveals that instead of seeking process equilibrium, non-equilibrium transients should be exploited to guide film deposition. This forms the first core concept behind the process. This concept also enables robust full-wafer processes for creation of uniform films as well as nanoscale films with prescribed variation of thickness at mm-scale spatial wavelengths. The use of inkjets enables zero-waste adaptive material deposition with the preferred drop volumes and locations obtained from an inverse optimization formulation. This forms the second core concept

behind the process. The optimization is based on the prescribed film thickness profile and typically involves $>100,000$ integer parameters. Using simplifying approximations for the same, three specific applications have been discussed - gradient surfaces in combinatorial materials science and research, elliptical profiles with $\sim 10\text{km}$ radius of curvature for X-ray nanoscopy applications and polishing of starting wafer surfaces for mitigation of existing nanotopography. In addition, the potential of extending the demonstrated process to high throughput roll-roll systems has also been mentioned by modifying the model to incorporate the compliance of the substrate along with that of the superstrate.

Table of Contents

Chapter 1: Introduction.....	1
1.1. Motivation.....	2
1.2. Deposition of Uniform Thin Films	3
1.3. Deposition of Spatially Varying Films	6
1.4. Process Overview.....	8
1.5. Process Control	11
1.5.2. Process Optimization	12
1.5.3. Presence of Parasitics.....	15
1.6. Applications for Spatially Varying Films	16
1.6.1. Gradient Surfaces.....	16
1.6.2. Surfaces for X-ray optics	18
1.6.3. Polishing of Wafer Topography.....	20
1.7. Dissertation Structure.....	22
Chapter 2: Baseline Model Development and Validation	24
2.1. Model Development.....	24
2.1.1. Governing Equations	25
2.1.2. Boundary Conditions	28
2.1.3. Non-dimensional Problem Formulation	30
2.1.4. Analytical Solutions.....	31
2.1.5. Numerical Solution Procedure	35
2.2. Preliminary Experiments	38
2.2.1. Experimental Methods	38
2.2.2. Metrology Methods.....	39
2.2.3. Results.....	40
2.2.4. Inference	42
2.3. Validation of Baseline Model	46
2.4. Summary	53

Chapter 3: Deposition of Highly Uniform Films	54
3.1. Changing Process Time Scale	55
3.1.1. Reducing Thickness of Superstrate	55
3.2. Uniform Film Deposition with Thin Superstrate	56
3.2.1. Experimental Results	56
3.3. Uniform Films with High Volume Drops	60
3.3.1. Model Premise	60
3.3.2. Problem formulation	61
3.3.3. Solution and Results	64
3.3.4. Qualitative Experimental Validation	66
3.4. Summary	67
Chapter 4: Inverse Model and Validation for Varying Thickness Films	68
4.1. Preliminary Experiments	68
4.1.1. Metrology	68
4.1.2. Stepped Profile	69
4.1.3. Continuously Varying Profile	70
4.2. Inverse Model	72
4.2.1. Problem Formulation	72
4.2.2. Constraints	73
4.2.3. Initial Condition	75
4.2.4. Optimization Solver	77
4.2.5. Simplifying Approximations	78
4.3. Experimental Validation	80
4.3.1. Process Limits	80
4.3.2. Film Thickness Profiles for Validation	81
4.3.3. Convergence Analysis	82
4.3.4. Results	83
4.4. Performance Prediction	86
4.5. Summary	87

Chapter 5: Applications of JCAST	88
5.1. One-Dimensional J-CAST	88
5.1.1. Inverse Model Enhancement.....	88
5.1.2. Metrology.....	90
5.1.3. Gradient surfaces	90
5.1.4. Surfaces for X-ray mirrors	96
5.2. Two-Dimensional J-CAST	101
5.2.1. Inverse Model Enhancement.....	101
5.2.2. Metrology.....	104
5.2.3. Wafer Polishing Experiments	105
5.3. Summary	111
Chapter 6: Deposition of Uniform Films on Flexible Substrates	112
6.1. Web buckling.....	112
6.2. Thin Film Evolution Model	114
6.2.1. Basic Modeling.....	115
6.2.2. Qualitative Validation.....	118
6.3. Summary.....	123
Chapter 7: Conclusions	124
7.1. Intellectual Merit.....	124
7.2. Broad Impact.....	126
7.3. Future Work	126
References.....	129

List of Tables

Table 1.1: Outline of generic properties of various solution-based material deposition techniques ²²	5
Table 2.1: Experimental conditions and results from preliminary experiments for uniform thin film deposition.	38
Table 2.2: Summary of non-uniformity encountered in the experiments and the same predicted by the models.	53
Table 3.1: Experimental data with the thin 250 micron cored superstrate	58
Table 3.2: Simulation results for mesoscopic drop spreading model.	65
Table 4.1: Deviation of the experimental result from the model prediction as well as the prescribed variation.....	83
Table 5.1: Summary of RMS errors for linear gradient surface with different drop volumes using J-CAST.	95
Table 5.2: Summary of RMS errors for concave and convex elliptical one-dimensional profiles with different drop volumes using J-CAST.....	100

List of Figures

Figure 1.1: Illustration of J-CAST process for uniform films and for films with prescribed variation in thickness	9
Figure 1.2: Illustration of the Jet-and-Flash Imprint Lithography (J-FIL) process	10
Figure 1.3: Illustration of a basic control framework for thin film deposition using J-CAST	12
Figure 1.4: Examples of process defects captured by the inline camera..	12
Figure 1.5: Formation of satellite drops due to sub-optimal jetting	14
Figure 1.6: Illustration of the different aspects of typical substrate topography	16
Figure 1.7: Illustration depicting thickness-dependent dewetting	18
Figure 2.1: Illustration of flexed superstrate initiating spreading and merging of dispensed drops.....	24
Figure 2.2: Illustration of the superstrate-fluid-substrate sandwich.	26
Figure 2.3: Illustration of boundary conditions.	30
Figure 2.4: Illustration of film thickness evolution in the presence of unimodal topography..	32
Figure 2.5: Plot showing influence of substrate nanotopography and spread time on film thickness non-uniformity.	33
Figure 2.6: Plot of non-uniformity against spread time showing influence of bimodal topography with representative values of topography amplitudes	35
Figure 2.7: Plots of the standard deviation in the film thickness and mean film thickness for uniform film deposition.....	39
Figure 2.8: Illustration of the normal to flat direction along which all measurements have been taken..	40
Figure 2.9: Picture of a sample each from the respective preliminary experiment cases.	41
Figure 2.10: Plot showing the amplitude distribution for different spatial frequencies as measured across different line scans on the Zygo optical surface profiler	43

Figure 2.11: Film thickness non-uniformity variation with spread time and 1D nanotopography amplitude of 2.5 mm spatial wavelength for cases 0 and 1	45
Figure 2.12: Film thickness non-uniformity variation with spread time and 1D nanotopography amplitude of 2.5 mm spatial wavelength for case 3.....	45
Figure 2.13: Film thickness non-uniformity variation with spread time and 2D nanotopography amplitudes of 10nm and 14nm, of spatial wavelengths 4mm and 2mm, respectively, for mean film thicknesses of 22nm and 73nm.....	46
Figure 2.14: Mean film thickness across each wafer used for experimental validation ...	47
Figure 2.15: Standard deviation associated with the mean film thickness across each wafer used for experimental validation.....	47
Figure 2.16: Residuals between the actual and reconstructed data at the initial condition.	49
Figure 2.17: Pictures of the same wafer at the spread times of 30s (initial condition), 45s & 125s.....	49
Figure 2.18: Plots comparing the experimental results against each of the two model versions for the spread times of 45s and 125s.	50
Figure 2.19: Plots depicting experimental validation of the linearized model for uniform films.	51
Figure 2.20: Plot showing the evolution of non-uniformity for both model versions and experimental data.	53
Figure 3.1: Illustration of geometry of 250 um cored superstrate.	56
Figure 3.2: Plot showing the experimentally obtained mean film thickness and non- uniformity on 5 wafers with a 250 micron cored superstrate.	59
Figure 3.3: Uniform films deposited using the thin 250 micron cored superstrate.	60
Figure 3.4: Geometry of the system under investigation for the mesoscopic model.....	61
Figure 3.5: Comparison of experimental result and model prediction for drops of different volume and pitch for achieving a similar mean film thickness.	66
Figure 4.1: Initial experiment with drops of non-uniform pitch.....	70
Figure 4.2: Illustration of using multiple drop patterns to get a desired graded film.	71

Figure 4.3: Schematic illustrating the inverse model formulation.....	74
Figure 4.4: Example of a modeled initial film thickness profile formed after merging of drops spaced at varying pitch.....	77
Figure 4.5: Plot showing the convergence of a normalized error in the optimization scheme for three randomly generated film thickness profiles.	82
Figure 4.6: Inverse model validation test cases	84
Figure 4.7: Pictures of the samples for case 2 and case 3.....	85
Figure 4.8: Hypothetical case of 1 pl drop volume giving much better agreement between the model prediction and desired profile for the ultra-thin film case 6.	87
Figure 5.1: Demonstration of linear gradient surfaces for materials research applications.	93
Figure 5.2: Illustration of optimal drop pattern layout for linear gradient surface with 6pl and 30pl drops.....	94
Figure 5.3: Deviation from desired film thickness for the experimental data and model prediction.	94
Figure 5.4: Demonstration of ~10km radius of curvature convex elliptical film thickness profile generated using J-CAST.....	97
Figure 5.5: Illustration of optimal drop pattern layouts for convex film thickness profile.	98
Figure 5.6: Demonstration of ~5km radius of curvature concave elliptical film thickness profile generated using J-CAST.....	99
Figure 5.7: Illustration of optimal drop pattern layouts for convex film thickness profile.	100
Figure 5.8: Image of the concave profile generated with 6pl drops.	101
Figure 5.9: Surface topography of Wafers 1-3 (from top to bottom) measured before polishing.....	106
Figure 5.10: Surface topography of Wafers 1-3 (from top to bottom) measured after polishing.....	107

Figure 5.11: Plots of absolute difference of RMS deviation between pre- and post-polishing surface profiles and percentage improvement of flatness defined as the ratio of RMS difference with pre-polishing RMS deviation from mean flatness.	110
Figure 6.1: Illustration of buckling in a web under uniaxial tension	113
Figure 6.2: Plot showing variation of critical buckling load with varying web length. .	113
Figure 6.3: Illustration of superstrate-fluid-substrate sandwich for a flexible substrate.	116
Figure 6.4: Plot showing the ratio of time scale for flexible versus rigid substrate.	118
Figure 6.5: Images of various films deposited on the flexible substrate with varying superstrate thickness, mean film thickness and time.	122
Figure 6.6: Plot depicting the relative value of process time scale for 250um superstrate against the 700um superstrate for both flexible and rigid substrates with increasing tension.	123

Chapter 1: Introduction

Deposition of nanoscale (sub 100nm) thin films is ubiquitously used in the realm of micro- nano-scale manufacturing. It is a basic unit step required in almost every nano-manufacturing process, be it additive or subtractive¹, and used for fabricating a variety of devices including integrated circuits, optical components, displays and magnetic storage devices² in addition to emerging applications in the biomedical³ and energy^{4,5,6} sectors. The choice of deposition method for a particular application is often driven by the process, cost and tolerance demands of the concerned application, leading to the development of a plethora of such techniques. Most commercially available solutions for deposition of sub-100nm films are designed for films with uniform thickness. While this suffices for a substantial number of applications, the increasing relevance of nanotechnological approaches outside the domain of semiconductors has led to a unique requirement – that of nanoscale films with prescribed variations in thickness across much larger spatial scales. This has spawned variations and modifications of existing techniques, wherein additional hardware is used to achieve the prescribed variation. There are hardly any techniques that have the capability and versatility to cater to uniform as well as spatially varying films within the same setup. To address this need across a broad variety of applications, a single process solution for both uniform films and films with prescribed spatial variation of thickness has been developed and investigated in this dissertation. The core of this research is built around the development of fundamental insights into a multi-scale fluid-structure problem that has been used to guide the design of the process. The study requires understanding and controlling fluid behavior over disparate length scales exceeding ratios of 10^6 . The resulting analytical

formulations, coupled with inverse optimization schemes, have led to the creation of a novel thin film deposition technique that is versatile, adaptive and sustainable.

In this chapter, the motivating guidelines behind the development of the thin film deposition technique have been laid out in Section 1.1, following which a brief survey of existing deposition methods has been carried out in Section 1.2 for uniform films and in Section 1.3 for films with prescribed spatial variation of thickness. An overview of the developed process is given in Section 1.4, while Section 1.5 discusses relevant process control aspects. Finally, Section 1.6 discusses a few representative areas where the process is potentially applicable, with Section 1.7 discussing the structure of the dissertation.

1.1. MOTIVATION

The cost of a manufacturing process is typically driven by speed (or throughput), tool complexity, cost of consumables, substrate cost, and the downstream processing (such as annealing, etching, developing, etc.) required. Hence, in order to lower cost, the direction to move must be towards high speeds, less complex tools, near-zero waste of consumables, and low-cost substrates. Deposition of thin films is no exception to this rule. While the choice of substrate, rigid or flexible, is governed by the overall desired process (wafer-based or in a roll-roll configuration), the pursuit of high throughput, low complexity and near zero material waste is still valid for a unit step of thin film deposition. This forms the motivating guidelines for this research.

To the best of the author's knowledge, there are no thin film deposition techniques that can deposit uniform films with high throughput and zero material waste, while also achieving the stringent uniformity targets demanded by the end applications and doing so over a broad range of film thicknesses on both rigid and flexible substrates.

The situation is similar for adaptively varying thin films, which also requires additional control over the spatial variation of film thickness. Hence, there is space for a thin film deposition solution that can cater to the demands of uniform nanoscale films across a broad range of thicknesses (~10nm-1000nm) as well as carry the same level of control for films with prescribed spatial variation in thickness, with zero waste and high throughput.

The development of a design and control framework for such a process cannot only rely on empirical models. Given that the motivation is to cater to widely varying film thicknesses for which the process must operate robustly under differing conditions, it is imperative to have a sound, experimentally validated physical basis along with optimized process parameters with minimal influence of parasitics to obtain the desired output. This research has, thus, followed the path of developing and validating physical models and then using the models to (i) optimize process parameters, (ii) identify and minimize the influence of random parasitics, and (iii) obtain the desired output with zero material waste and high throughput. Before discussing the process in further detail, it is instructive to review existing nanoscale thin film deposition options for both, uniform as well as spatially prescribed thickness.

1.2. DEPOSITION OF UNIFORM THIN FILMS

There are a variety of techniques that are currently being used to deposit nanoscale uniform films, both from solution and from vapor. Vapor-based techniques, such as Chemical Vapor Deposition (CVD) and its variants, are typically more expensive than solution based methods due to the need for more complex chambers, vacuum environments, exhaust controls and high material consumption⁷. Spin-coating (SC) is the industrial workhorse for depositing films from solutions. Several studies have been conducted on SC detailing the effect of different parameters on the uniformity of

deposited films^{8,9,10,11}. SC processes lead to significant material waste as the solution is spun-off beyond the edge of the substrate. In addition the solutions are dissolved in solvents that evaporate leading to material loss. Overall, about 95% of the material is wasted in SC processes¹². Another aspect of SC is that the nanoscale thickness control is disrupted when the deposition is done over pre-existing topography^{13,14,15,16}.

With the need for more sustainable processes, inkjetting has also become an attractive technique for material deposition as well as inexpensive patterning due to its direct write, ‘maskless’ nature. Compared to SC, it results in much lower material consumption, and hence, has been used for the fabrication of a range of devices like Thin Film Transistors (TFTs), RFIDs, and Photovoltaic (PV) cells¹⁷. However, due to the presence of a substantial vapor-liquid interface in the dispensed drops, evaporation and gradients in surface tension can cause local film thickness non-uniformity leading to the infamous ‘coffee-ring effect’^{18,19}. Moreover, film thickness uniformity is also influenced strongly by the volume of the individual drops; the surface properties of both, the dispensed fluid as well as the substrate; and the spacing between consecutive drops, or the drop pitch, which needs to be low enough to allow the drops to spread and merge^{20,21}. Hence, in spite of having remarkably low material consumption, the above factors make process control for inkjet-based deposition of large area uniform nanoscale thickness films, challenging. Different aspects of ink-jetting, spin-coating and other solution-based material deposition techniques have been summarized in Table 1.1.

The presence of flexible substrates in roll-roll configurations puts additional constraints on film deposition. Most flexible substrates are incompatible with high temperature processing, thereby rendering many vapor-based processes, including CVD, unusable. Deposition on R2R flexible substrates is usually carried out using one or more solution-based techniques that have been outlined in Table 1.1. However, most of these

processes do not have the inherent accuracy to achieve nanoscale control on the film thickness uniformity and are typically applicable only for films > 100nm thick^{22,23}. It must be noted that SC, the workhorse of the semiconductor industry, is incompatible with R2R systems.

Table 1.1: Outline of generic properties of various solution-based material deposition techniques²².

Technique	Ink waste	Pattern	Speed	Ink preparation	Ink viscosity	Wet thickness (um)	R2R compatible
Spincoating	5	0	-	1	1	0-100	No
Doctor blade	2	0	-	1	1	0-100	Yes
Casting	1	0	-	2	1	5-500	No
Spraying	3	0	1-4	2	2-3	1-500	Yes
Knife-over-edge	1	0	2-4	2	3-5	20-700	Yes
Meniscus	1	0	3-4	1	1-3	5-500	Yes
Curtain	1	3	4-5	5	1-4	5-500	Yes
Slide	1	3	3-5	5	1-3	25-250	Yes
Slot-die	1	1	3-5	2	2-5	10-250	Yes
Screen	1	2	1-4	3	3-5	10-500	Yes
Ink jet	1	4	1-3	2	1	1-500	Yes
Gravure	1	2	3-5	4	1-3	5-80	Yes
Flexo	1	2	3-5	3	1-3	5-200	Yes
Pad	1	2	1-2	5	1	5-250	Yes

Ink waste: 1 (none), 2 (little), 3 (some), 4 (considerable), 5 (significant). Pattern: 0 (0-dimensional), 1 (1-dimensional), 2 (2-dimensional), 3 (pseudo/quasi/2/3-dimensional), 4 (digital master). Speed: 1 (very slow), 2 (slow<1m/min), 3 (medium 1-10m/min), 4 (fast 10-100m/min), 5 (very fast 100-1000m/min). Ink preparation: 1 (simple), 2 (moderate), 3 (demanding), 4 (difficult), 5 (critical). Ink viscosity: 1 (very low<10cP), 2 (low 10-100cP), 3 (medium 100-1000cP), 4 (high 1,000-10,000cP), 5 (very high 10,000-100,000cP).

1.3. DEPOSITION OF SPATIALLY VARYING FILMS

While the deposition of uniform nanoscale films is common in several disciplines, including semiconductor manufacturing, the deposition of spatially varying films has been the subject of research and development only recently, with limited commercially available options. Such films can also facilitate generation of freeform surfaces. The focus on applications has been treated separately in Section 1.6. In general, if cost-effective versatile deposition methods for varying thickness films become available, it can enable a host of potentially new applications. In this section, a short survey of representative deposition methods for spatially varying films has been carried out to establish the state-of-the-art before describing the new process in detail. Similar to deposition of uniform films, methods for varying film thickness come in two primary flavors - solvent-based and vapor-based. Solvent based deposition techniques include modifications and variants of existing approaches, e.g., knife-edge coating, inkjet-based and electrochemical deposition, while vapor-based techniques are also enhancements of existing methods like CVD.

Flow coating has been developed at NIST as a velocity-gradient knife-edge coating process^{24,25}. A drop of the polymer solution is deposited on the substrate which is moved at constant acceleration. The competition between friction drag as a result of the velocity gradient action of the substrate and the capillary forces due to the stationary knife-edge placed $\sim 200\mu\text{m}$ above the substrate during the substrate motion creates a thickness gradient of the film. Subsequent evaporation leads to the realization of sub-micron thickness films. Thin polystyrene films with range even in the sub-100 nm regime have been demonstrated using this apparatus, but it is unclear whether films in non-monotonic profiles can be obtained using the same. Inkjet-based deposition of spatially varying films is similar in concept to inkjet-based patterning²⁶. It has been carried out by

dispensing ~100 pl drops using a single nozzle tip attached to a high-resolution motion stage that can precisely map desired locations on the substrate. However, after dispensing, substantial amount of evaporation is induced to ensure the film thicknesses desired for the application, which is the screening of biosensors for enzyme activity. A variation of electrochemical deposition has also been used, in which varying thickness poly-electrolyte films have been deposited using spatially tunable electric field gradients²⁷. In addition, variable salt etching of polyelectrolyte films where the amount of material removed is controlled spatially to realize thin film thickness gradients has also been demonstrated²⁸. However, such techniques may not have the film thickness range and resolution required to be applicable for a broad spectrum of areas. A more detailed presentation of deposition methods for films with graded thicknesses has been given in Figures 2.2 and 2.3, and Tables 3.1 and 3.2 in reference²⁹.

The deposition of ultra-thin films with functional gradients is an active area of research in the biomedical domain related to studying various factors involved in tissue engineering. To this end, biomimetic films have been fabricated by a layer-by-layer (LBL) assembly process, wherein it is possible to impart functional gradients at a molecular level and higher to screen events such as protein adsorption and cell adhesion³⁰. The LBL techniques mainly proceed through a combination of various surface interactions, including electrostatic forces, van-der-Waals forces, hydrogen bonds etc. Grafting of polymer molecules on functionalized substrates with temperature gradients also results in thickness gradients³¹.

In addition to the above mentioned methods, vapor-based techniques are also available, primarily for depositing inorganic films with varying thicknesses³². These techniques mostly employ a motion-controlled mask to generate the required thickness profiles^{33,34,35}, or use a discretized shower head with control over each shower unit³⁶.

Such methods have limited film thickness variations that can be achieved and often require a change in hardware to generate a variety of profiles, thus constraining their versatility across various applications.

1.4. PROCESS OVERVIEW

Building on the idea of using ink-jets for film deposition, a novel process called Jet and Coat of Adaptive Sustainable Thin Films or J-CAST has been developed in this research. J-CAST uses inkjets to dispense accurate sub-40 picoliter sized droplets of a UV-curable monomer on the substrate. The basic process is similar for deposition on rigid and flexible substrates. A rigid substrate is typically chucked with vacuum, while a flexible substrate is held under tension during the deposition process.

The substrate surface is pre-treated with an ultra-thin 1-3 nm layer of an adhesion layer (AL) that acts to enhance the spreading of the monomer. Using a bank of multiple inkjet nozzles and dispense passes, the desired substrate area can be covered with the required drops in a few seconds, while retaining control over the volume and location of each dispensed drop. Following drop dispense, a flexible blank fused silica superstrate that has been bowed with the help of a pressure on its passive side, is brought down such that first contact on the drops is made by the active side. This initiates a front that quickly spreads outward merging with the drops along the way and thereby creating a contiguous fluid film. On a rigid substrate, the first contact happens at a point close to the center and the front spreads radially outwards, whereas on a flexible substrate, the first contact happens along a line close to one edge and spreads horizontally to cover the substrate.

This substrate-fluid-superstrate “sandwich” is then allowed to evolve for a desired duration called the spread time, following which the monomer is cured by exposure to UV light through the template. The template is then separated from the sandwich leaving

the thin polymer film on the substrate. The process has been illustrated in Figure 1.1. This process is similar to Jet-and-Flash Imprint Lithography (J-FIL)^{37,1}, (Figure 1.2) and can be carried out on a large area J-FIL tool such as the Imprio 1100 for wafers and a newly developed LithoFlex tool for J-FIL on flexible substrates in a R2R configuration. This allows the J-CAST process to substantially leverage a tool infrastructure developed for imprint lithography.

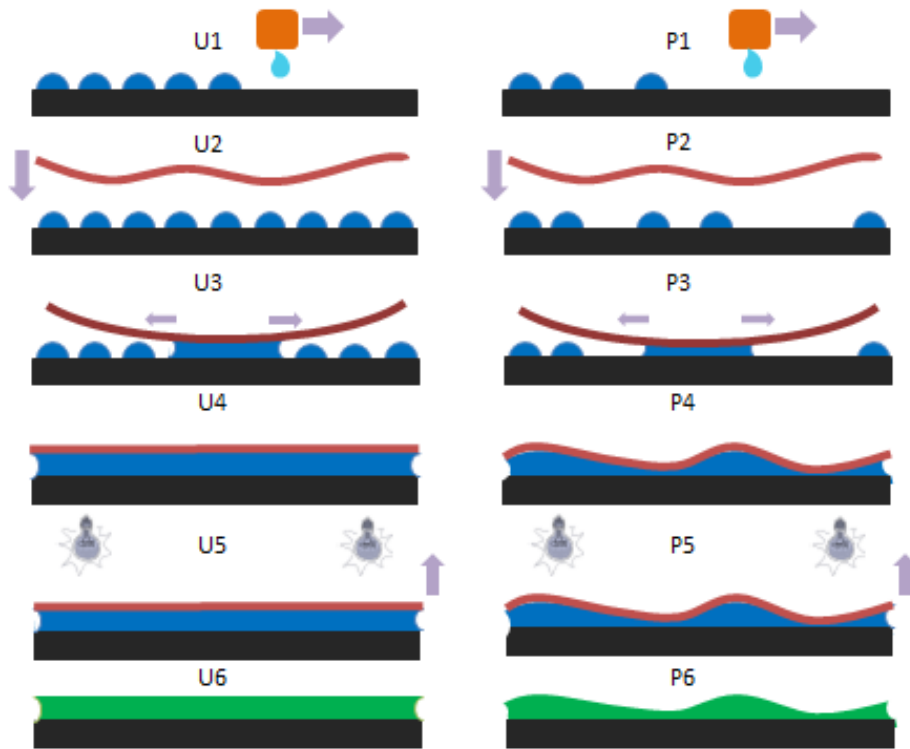


Figure 1.1: Illustration of J-CAST process for uniform films (labeled as U) and for films with prescribed variation in thickness (labeled as P). In step 1, inkjetting of the material on the substrate is shown. For uniform films, equi-spaced drops are dispensed. For prescribed variation of film thickness, the drops are not equi-spaced. Their optimal locations are derived from an inverse optimization framework. In step 2, a flexible superstrate, which need not be optically flat, is brought down on the dispensed drops to initiate a fluid front as shown in step 3. The drops merge to form a contiguous film and the superstrate-fluid-substrate sandwich is allowed to evolve to a non-equilibrium transient state, as shown in step 4. After UV-exposure, the superstrate is separated, as in step 5, leaving the polymer film behind.

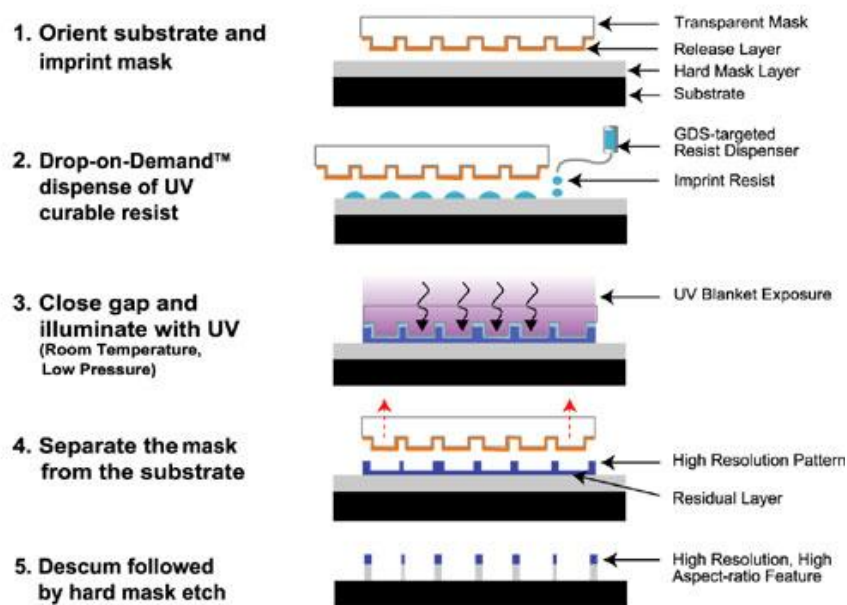


Figure 1.2: Illustration of the Jet-and-Flash Imprint Lithography (J-FIL) process. (Courtesy: Molecular Imprints, Inc.)

There is, however, a key challenge specific to J-CAST that has not been addressed in the imprint lithography literature. The typical monomer thickness dispensed at the end of an imprint lithography process is sub 20 nm. This is deliberately kept thin to allow follow-on de-scum etching and subsequent pattern transfer of nanostructures into the underlying substrate. However, the basic aim of the J-CAST process is to allow for the liquid to adopt a desired spatial profile. This would imply average film thicknesses that can be greater than 100 nm, and local film thicknesses as high as 1µm leading to a different flow regime altogether. At sub-20nm film thicknesses, the flow is viscous dominated that does not allow rapid re-distribution of the fluid. However at film thicknesses approaching a micron, the flow re-distribution is rapid thereby requiring precise control to not compromise the essential value of adaptive material deposition.

The primary difference between J-CAST and stand-alone inkjetting is that the dispensed drops in J-CAST are then coerced by another flat plate to make them spread

and merge into a contiguous film. This gets rid of the problems with stand-alone inkjetting as the fluid film is now sandwiched between two flat plates. This confines evaporation to only the outer perimeter of the film, where there is a vapor-liquid interface, which is substantially smaller in area than that for stand-alone inkjetting. The forced spreading and flowing of drops under the squeezing action of the top plate also prevents the occurrence of uniformity-disrupting effects like the ‘coffee-ring’^{18,19}.

1.5. PROCESS CONTROL

Attaining the desired output after J-CAST requires a robust process control framework that can optimize the process for the differing conditions under which it must operate. Such a process control framework works best if based on experimentally validated physical models that can predict the behavior of the system and also capture the influence of relevant process parasitics for mitigation of the same. As illustrated in Figure 1.3, process settings are based on the desired application and the substrate configuration (rigid or flexible). These settings, coupled with the input of parasitics such as substrate topography (explained later in Section 1.5.3) are based on offline process optimization enabled by the validation of physical models. Although robust model-based and inline metrology enabled real-time process control is desirable, the current setup only has a rudimentary version of the same. The inline monitoring is mainly done visually through a camera, which is useful for detecting large-scale process defects like the presence of particles and inkjet drop volume miscalibration, examples of which are shown in Figure 1.4. Subsequent to deposition using J-CAST, offline film thickness metrology is undertaken which is used to further optimize process settings. This forms the basic process control framework. Details of important aspects of the same have been discussed in the ensuing sections.

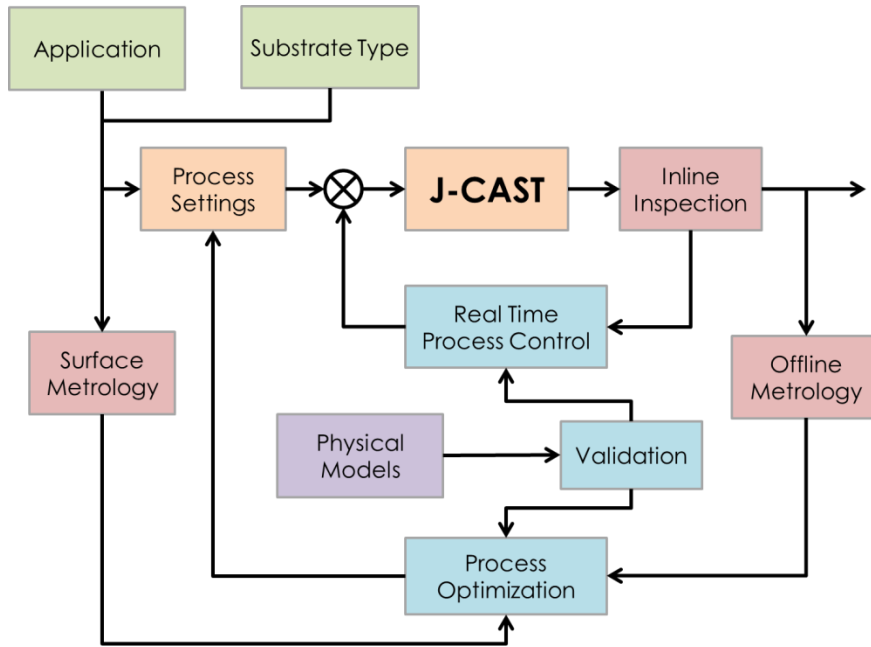


Figure 1.3: Illustration of a basic control framework for thin film deposition using J-CAST

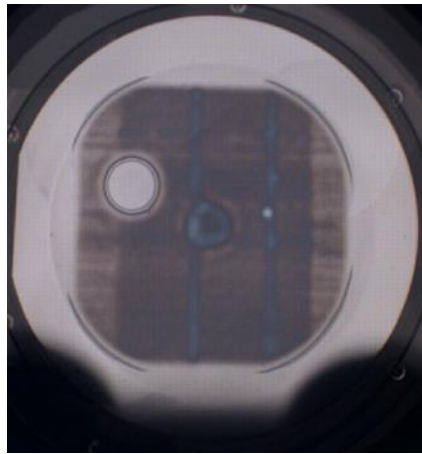


Figure 1.4: Examples of process defects captured by the inline camera. The blue features represent inkjet drop volume and location perturbations caused by misfiring of one or more nozzles. The circular feature on the left is because of the presence of a particle on the wafer which impedes in the spreading and merging of drops in its vicinity.

1.5.2. Process Optimization

J-CAST is a combination of several physical processes at widely varying length and time scales. The length scales range from film thickness (~10-100 nm) to the

dimensions of the substrate (~100 mm). At the same time, the time scales vary from milliseconds for the intra-drop surface phenomena, to seconds for the drops to merge to form a contiguous film, and to tens of seconds for the superstrate-fluid-substrate sandwich to evolve. This necessitates the use of multi-scale models that should ideally capture the following relevant physics: (i) accurate formation and inkjetting of drops, (ii) deformation of the superstrate and/or substrate; (iii) spreading of drops on the substrate; (iv) merging of the drops to form a contiguous film; (v) temporal evolution of the sandwiched fluid film, and (vi) stress relaxation in the substrate and superstrate after separation.

J-CAST relies on placing the appropriate amount of material where desired. For this purpose, reliable ink jetting is of paramount importance. This requires careful understanding of fluid rheological properties, ink jet geometry and environmental factors such as humidity and temperature³⁸. Inkjetting of drops with accurate volume and at the prescribed location can only take place if these conditions are well controlled so as to ensure that no satellite drops are formed (Figure 1.5). Given the significant complexity of the physics and the large number of possible sources of variability, a study of inkjet drop formation and subsequent dispensing is mostly done empirically with the help of experimental calibration for the given nozzle and material combination. For the purpose of J-CAST in this work, the fluid material used, MonomatTM, is a proprietary UV-curable resist from Molecular Imprints, Inc. and is already optimized and calibrated for the inkjet system installed in the tool infrastructure (Imprio 1100 and LithoFlex). Future uses of J-CAST with different materials will, however, need a thorough calibration to ensure reliable inkjetting and can be done on an inkjet test bed installed in the facility.

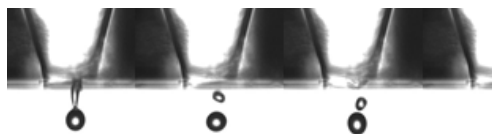


Figure 1.5: Formation of satellite drops due to sub-optimal jetting. (Courtesy: Vik Singh)

Like drop dispensing, the spreading and merging steps are also primarily experimentally driven. There are models available for the motion and merging of contact lines on both rigid and flexible substrates^{39,40,41,42,43,44}. But, these models mostly rely on expensive numerical simulations for even a small number of drops and are also not directly applicable for a fluid film sandwiched between two plates. This precludes the use of these models in a high-throughput process control framework where the fluid film is composed of several thousand drops. Hence, the optimization of this step is carried out through a careful design of experiments by varying the pressure field and temporal pressure gradient applied on the superstrate to achieve a near constant fluid front velocity and to ensure that there are no stable air pockets. Once optimized, these values of the pressure field and gradient can be repeatedly used in most cases without further optimization, unless a significant alteration to the merging characteristics is desired.

The evolution of the thin fluid film formed after all the drops have merged till UV exposure is the mainstay of this work. Exploiting the dynamics of this process can lead to a spectrum of evolutionary behaviors. This has been depicted in significant detail in Chapter 2. After thin film evolution, UV exposure followed by separation of the superstrate from the sandwich is carried out. UV exposure initiates cross-linking of the photo-acids in the resist thereby leading to polymerization of the fluid film. This cross-linking also leads to a slight shrinkage in volume. These steps are also not modeled explicitly, as the resist used has already been optimized for these phenomena.

1.5.3. Presence of Parasitics

The presence of process parasitics can corrupt the desired film thickness profile. Probably, the most important parasitic is the topography of the substrate and the superstrate. As seen in Figure 1.6, the topography of any surface can be classified in three broad categories, depending upon the amplitude and spatial wavelength of the same: (i) nominal shape, (ii) nanotopography and (iii) roughness. The nominal shape is given by the largest spatial wavelengths, typically $> 20\text{mm}$ with height variations typically from $0\text{-}10\text{mm}$. For spatial length scales of $\sim 1\text{-}20\text{mm}$, height variations, usually $\sim 100\text{nm-}1\text{micron}$, at this spatial wavelength range are classified as nanotopography^{45,46}. Roughness is classified for lower spatial wavelengths with much smaller height variations. While the nominal shape of a substrate surface is usually decided by the nature of wafer preparation and the tooling and chucking infrastructure used in the same, roughness is usually mitigated by standard polishing techniques. It is the intermediate nanotopography that is probably the most critical surface topography parameter for this work and as will be seen in later sections, has the most significant impact on the evolution of the thin film sandwich.

Flexible substrates are desirable because of their low costs and compatibility with R2R processes. However, such low-cost substrates usually have significant surface topography variations due to the inability to accommodate complex and expensive polishing processes in their cost structure. An example of such substrates would be thin ($\sim 100\mu\text{m}$) plastic sheets, e.g. poly-ethylene terephthalate or PET, used in conventional R2R manufacturing systems like paper processing for their ability to be processed at high speed and low cost. These variations can compromise the desired process control. Hence, it is important to mitigate the influence of substrate topography, but without compromising with the objective of a low-cost solution.

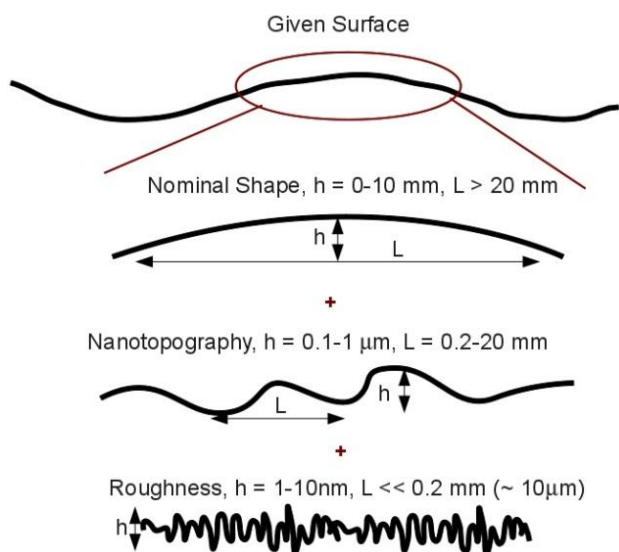


Figure 1.6: Illustration of the different aspects of typical substrate topography

1.6. APPLICATIONS FOR SPATIALLY VARYING FILMS

While the deposition of uniform films has several applications related to the fabrication of commonly used devices, the deposition of spatially varying films has some novel applications that have been discussed herewith. These are by no means an exhaustive list of applications for J-CAST.

1.6.1. Gradient Surfaces

Gradient surfaces represent a continuous change in one or more material properties over space, thus permitting the exploration of an immense set of experimental conditions²⁹. The influence of entire parameter spaces can be captured simultaneously on a single specimen, leading to faster materials experimentation with less waste. In fact, combinatorial approaches of materials characterization are often used interchangeably with ‘high throughput experiments’, bringing out the power and utility of these techniques to the experimental material scientist. This simultaneous expression of

material behavior can be amplified by combining more than one gradient on the same specimen, leading to even greater savings. The properties of interest for gradient surfaces can be chemical (for example: composition, wettability etc.) as well as physical (for example: temperature, film thickness etc.). Such surfaces can be used for characterizing and screening of material properties as well as for driving process-related phenomena. For example, with thickness gradients alone, all the above objectives can be achieved. Graded block copolymer film thicknesses can help in understanding and characterizing the morphology or dewetting of block copolymers as a function of film thickness (Figure 1.7). At the same time, the same thickness gradients can be useful in the discovery and screening of sensing materials such as fluorescent dyes with respect to a given sample. Moreover, the spatially varying interfacial energies that are concomitant with films of prescribed nanoscale thickness variation can be used to enhance or disrupt the motion of drops of certain materials. Hence, it can be seen that even with film thickness gradients alone, there is tremendous opportunity for such surfaces, particularly in the biomedical, pharmaceutical and biomaterials domain, where there is a need for high-throughput and cost-effective creation of gradient libraries.

There are two main challenges to using gradient surfaces in scientific analyses. The first is creating such surfaces and the second is using these surfaces as a reliable platform for experimentation. In general, gradient surfaces can be created by harnessing natural phenomena or by using what are known as gradual processes to deliver the spatial gradient through a mediating instrument. Gradients are ubiquitous in nature and thus, relying on the forces of nature can deliver, for example, concentration gradients through diffusion or temperature gradients through conduction. However, natural processes can be prohibitively slow, especially for polymers with massive molecules. Also, uncontrolled perturbations can lead to variations in the desired gradient. Hence, natural

processes are not particularly favored when it comes to reliable generation of gradient surfaces. The second approach is more commonly used and has been discussed previously in Section 1.3. The idea there is to use the motion of the specimen itself or use a mask or mediating tool in a controlled fashion to deliver the spatial gradient. For example, controlled UV exposure with the help of a mediating mask can generate wettability gradients on a surface pre-treated with a functional wetting agent that can be used to study the motion of drops of different materials on the same specimen. However, the lack of versatility of a given mask for generating an entire library of gradients and the need for new masks for novel profiles impedes the universal applicability of this technique. Direct, maskless, multi-source co-deposition through CVD and laser ablation is another option for generating gradients in composition, particularly for inorganic materials. This is not amenable for polymer materials due to their incompatibility with high temperature processing.



Figure 1.7: Illustration depicting thickness-dependent dewetting

1.6.2. Surfaces for X-ray optics

Imaging of X-rays has been a very useful tool in the astronomical and medical domains. Recently, there has been a thrust towards enabling nanoscale imaging using X-rays, particularly for the purpose of nanoscopy⁴⁷. Reliable nanoscopy using X-rays can potentially have significant impact in the fields of biomedical imaging, semiconductor manufacturing and material identification among others. X-rays offer advantages over state-of-the-art electron-beam microscopes because of their ability to penetrate deeper into the sample and their versatility in imaging different materials. However, there are

significant technical challenges towards reliably achieving the nanoscale resolution required for truly enabling nanoscopic-based applications. Most of these challenges stem from the stringent requirements for fabricating the focusing and/or imaging optics for X-ray nanoscopes. These requirements are amplified when it comes to reflective optics for hard x-rays, as compared to zone plates for soft x-rays.

Reflective optics for X-rays relies on metal-coated mirrors for focusing purposes. They are mostly used for hard X-rays given the challenges involved in using zone plates for the same. However, reflective mirrors must use grazing incidence, i.e., near zero incidence angles, to achieve the desired resolution and focus, although this requirement is relaxed for multilayer mirrors that rely on interference related reflection. This is because the index of refraction for X-rays is given as $n = 1 - \delta - i\beta$, where δ and β are related to atomic scattering⁴⁸, with δ being of the order of 10^{-5} . This results in critical angles of approximately 2 degrees, 0.6 degrees and 0.1 degrees for an iridium sample with X-rays of energy 1, 10 and 100 keV, respectively, to achieve total external reflection. Given this constraint, it can be imagined that these mirrors require stringent spatial control over the surface roughness and figure ($\sim\lambda/10$), which is analogous to nanotopography for wafers. The wavelength of X-rays is $<10\text{nm}$, which implies that the desired spatial control is $<1\text{nm}$. Any perturbation in roughness and figure above this tolerance limit can cause undesired scattering effects^{49,50,51}. Hence, adaptive figure correction is an important element for getting the desired quality of the optical elements^{52,53,54}. Moreover, the desired profile of a mirror surface is usually a conic section (parabolic, hyperbolic or elliptical), such that an arrangement of multiple such mirrors can achieve the desired focusing properties. Such profiles have been demonstrated by vacuum based preferential coating or differential deposition techniques on surfaces that are not nominally conic sections^{35,55}. J-CAST, potentially, has the ability to do both, correct for figure

imperfections as well as adaptively modify the figure to resemble conic section surfaces by depositing films with appropriate spatial variations in thickness.

1.6.3. Polishing of Wafer Topography

Given that the topography and roughness of any surface can present problems for further processing of the substrate, several techniques have evolved over many years to mitigate these. There are three basic techniques briefly described here.

Grinding, lapping and polishing are routinely used in manufacturing facilities to remove roughness on a variety of substrates, including metals, glasses, semiconductors, optics and ceramics. Depending upon the quality and roughness of the final surface finish, the mechanical properties of the substrate and the irregularities or longer-range topography, one or more of these processes can be used to achieve the desired objective. They rely on mounting the substrates on rotating wheels or jigs and using abrasive particles of varying sizes to correct for the roughness and topography. While grinding is used for coarse-level correction with high speeds and large particles, lapping and polishing and their variants can produce much finer surface finishes of precision optics quality

At this point, it is instructive to look at a high-end application requiring excellent surface quality, namely the fabrication of mask blanks for Extreme Ultra-Violet Lithography (EUVL), which is carried out with 13.5 nm wavelength light. Both the mid-spatial frequency roughness (MSFR) and the high-spatial frequency roughness (HSFR) need to be less than 0.15 nm (at an effective spatial wavelength of 10 μ m). Moreover, the topography variation on the substrate also has to be less than 32 nm peak-valley (PV) over an area of 36 sq. in^{56,57,58}. Current global mask blank polishing techniques, both batch and single-sample, can push the present 500 nm peak-valley (PV) flatness levels

down to 100 nm PV, but they are not sufficient to reach the levels for EUVL. Techniques such as Magneto-Rheological Finishing (MRF) and Ion Beam Figuring (IBF) have been suggested to correct for the flatness in EUVL mask blanks⁵⁷. However, both these techniques suffer from very slow turn-around times either due to the inherently low throughputs or due to additional polishing steps required to continuously correct for the flatness. Such techniques are therefore costly and are limited only to parts that can command very high value.

Spin on Glass and Etch back is one technique used for micron scale device manufacturing. As the name implies, a glass dielectric is spin-coated on the substrate followed by etching in a chemistry that ensures equal etching rates for both the sacrificial glass and the underlying film or substrate material⁵⁹. Photoresists may also be used instead of glass. However, the global planarity that can be achieved by this technique is limited. Also, planarization over a large isolated topographical feature has been studied for the reverse-tone J-FIL process, also known as JFIL-R¹³. This relies on surface tension and capillary effects to smoothen a spin-coated Si containing film that can be etched to obtain a smooth profile. Imprint lithography based planarization has also been dealt with in the literature^{60,61}.

To meet the stringent requirement of planarity in submicron device technologies Chemical Mechanical Polishing (CMP) is the most widely used polishing technology. It uses a combination of abrasive laden chemical slurry and a mechanical pad for achieving planar profiles. The biggest concern with CMP is the dependence of material removal rate on the pattern density of material, leading to the formation of a step between the high density and low-density. The step shows up as a long-range thickness variation in the planarized film, similar in scale to the nanotopography of the surface. Preventive techniques like dummy fill and patterned resist can be used to reduce the variation in

pattern density. These techniques increase the complexity of the planarization process and significantly limit the device design flexibility. CMP has been demonstrated on non-flat surfaces as well. However, the material and hardware required for planarizing such substrates are different from those required for planar surfaces, hence limiting flexibility across different profiles.

Contact Planarization (CP) has been reported as an alternative to the CMP processing^{62,63,64}. A substrate is spin coated with a photo curable material and pre baked to remove residual solvent. An ultra-flat surface or an optical flat is pressed on the spin-coated wafer. The material is forced to reflow. Pressure is used to spread out material evenly and achieve global planarization. The substrate is then exposed to UV radiation to harden the photo curable material. Although attractive, this process is not adaptive as it does not account for differences in surface topography of the wafer and the optical flat, nor can it address all the parasitics that arise during the process itself. Also, using a high-viscosity material slows down the reflow and limits the throughput that can be achieved. J-CAST is a potential adaptive alternative for wafer polishing, as it can deposit films of varying thickness to compensate for the topography of any wafer and get a nominally flat top surface.

1.7. DISSERTATION STRUCTURE

The structure of the dissertation has been given herewith. Chapter 2 details the development and experimental validation of a baseline model for the J-CAST process. It outlines the basic physical phenomena involved, the dependence on various parameters and different applicable boundary conditions. Chapter 3 uses the findings of the baseline model to demonstrate the deposition of highly uniform films using J-CAST. A variant of the baseline model to understand the non-uniformity inherent in the drop spreading step

has also been discussed. In Chapter 4, the model-based enhancement and optimization of J-CAST has been mentioned for films with prescribed spatial variation in thickness. This is accompanied by an experimental validation of the same. Chapter 5 carries the J-CAST process forward with a demonstration of representative applications in the generation of gradient surfaces, surfaces for X-ray mirrors as well as polishing of wafers. In Chapter 6, the implementation of J-CAST for deposition of uniform films in flexible substrates has been discussed. This is enabled by a modification of the baseline model developed in Chapter 2. Chapter 7 has the concluding remarks and scope for further work.

Chapter 2: Baseline Model Development and Validation

This section outlines the path taken to develop and validate a model that captures the primary physics in the problem of confined thin film evolution. The baseline model has been developed to understand the mechanics after the drops have merged to form a contiguous “macroscopic” film. Preliminary experiments done to understand the influence of basic process parameters have been followed by a detailed description of the experimental validation.

2.1. MODEL DEVELOPMENT

A baseline model can be constructed incorporating the two primary phenomena observed in the process, thin film fluid flow and elastic bending of the fused silica superstrate. In the physical process, the superstrate is held only at its periphery by vacuum while a uniform air pressure is applied along its back passive surface to flex it sufficiently. This flexing helps initiate small-area contact of the front active surface of the superstrate with the drops dispensed close to the center on the substrate, resulting in a radially spreading front that merges the drops and forms the contiguous film. The temporal evolution of this superstrate-liquid-substrate “sandwich” prior to UV exposure is the mainstay phenomenon under consideration. The silicon substrate is considered rigid as it is held by a vacuum pin chuck.

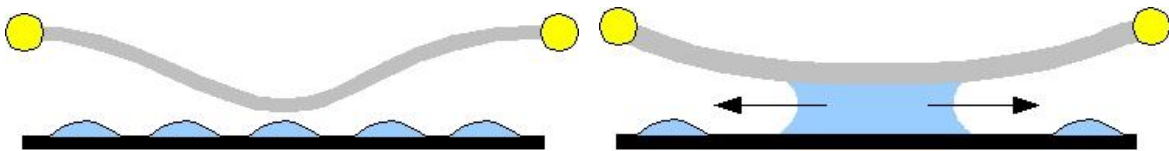


Figure 2.1: Illustration of flexed superstrate initiating spreading and merging of dispensed drops.

2.1.1. Governing Equations

The desired nominal fluid film thickness in J-CAST is $\sim 10\text{nm}-1\mu\text{m}$, whereas the substrate is spread over $\sim 100\text{mm}$. Fluid flow in domains that have much larger lateral length scales compared to height (thin films) can be solved using the lubrication approximation which assumes that the flow is predominantly parallel to the surface and the normal pressure gradient is zero^{65,44,66}. From conservation of momentum, this gives:

$$\frac{\partial p}{\partial x} = \mu \frac{\partial^2 u}{\partial z^2} \quad \dots 2.1$$

where μ is the viscosity, u is the velocity field and p is the pressure field. Integrating the above equation in z , or the thickness co-ordinate gives a parabolic velocity profile as:

$$u = \frac{1}{2\mu} \frac{\partial p}{\partial x} z^2 + c_1 z + c_2 \quad \dots 2.2$$

The continuity or volume conservation equation is given by:

$$\frac{\partial h}{\partial t} + \frac{\partial}{\partial x} \int_0^h u \, dz = 0 \quad \dots 2.3$$

Combining equation 2.2 and the continuity equation 2.3 with boundary conditions of no slip, i.e., $u = 0$, at both the top deformable surface ($z = h$) and the bottom rigid substrate ($z = 0$), gives the thin film evolution equation as:

$$\frac{\partial h}{\partial t} = \frac{1}{12\mu} \frac{\partial}{\partial x} \left(h^3 \frac{\partial p}{\partial x} \right) \quad \dots 2.4$$

where h is the local film thickness. This equation 2.4 describes the flow of the liquid confined between the two surfaces under the action of a gradient in pressure. At the same time, it is also known that the top surface can flex and deform in bending under the action of a pressure field. The deformation is described using classical thin plate bending mechanics⁶⁷ as:

$$p = D \frac{\partial^4 w}{\partial x^4} \quad \dots 2.5$$

$$D = \frac{Eb^3}{12(1-\nu^2)} \quad \dots 2.6$$

where D denotes the flexural rigidity of the superstrate, w is the superstrate deformation field, b is the superstrate thickness, E and ν are the Young's modulus and Poisson's ratio, respectively, of the superstrate material. It is assumed that deformation due to bending is dominant over that due to in-plane tension and is the primary manifestation of strain energy. This approximation is valid as there is no applied in-plane stresses. However, when the process is carried out on flexible substrates, membrane tension has to be included in the analysis, as the strain is then carried mostly by applied tension due to the low rigidity of these substrates. This will lead to a modification of the governing equations, which will be covered later in Section 6.2

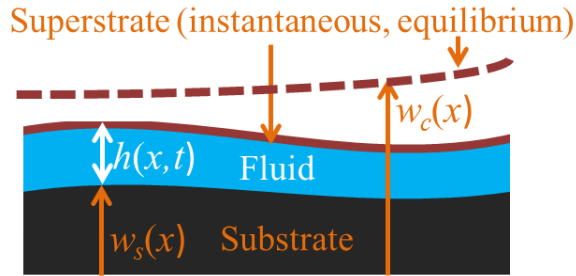


Figure 2.2: Illustration of the superstrate-fluid-substrate sandwich.

Assuming that the substrate and superstrate topography are given by $w_s(x)$ and $w_c(x)$ respectively, the deformation field at any instant of time can then be written as $w = h + w_s - w_c$ as shown in Figure 2.2. Ideally, the substrate topography should be expressed in body-fitted co-ordinates for the substrate to allow for the lubrication assumption of zero flow normal to the substrate to be valid⁶⁸. However, given that polished wafers are nominally flat with negligible slopes locally, the lubrication approximation with fixed orthogonal co-ordinate system to express the substrate

topography is valid*. Hence, a coupling between the pressure field and the fluid film thickness is obtained by combining equations 2.5 and 2.6 with equation 2.4. Extending the one-dimensional system to two dimensions, the overall governing equation is given as:

$$\frac{\partial h}{\partial t} = \frac{D}{12\mu} \vec{\nabla} \cdot (h^3 \vec{\nabla} \nabla^4 (h + w_s - w_c)) \quad \dots 2.7$$

There have been a few investigations in the literature, studying the coupling of thin film fluid pressure with other physical phenomena, including capillary pressure, disjoining pressure and even elastic bending^{69,70,71,72,73,74,75}. The influence of substrate topographical features on related thin film flows has also been investigated in the literature^{76,77,78,79,80,81,82,41}. To the best of the author's knowledge, no prior investigation has been conducted for the non-static physical case involving a sandwiched thin film in the presence of topography at the scale of the J-CAST process.

Unless otherwise mentioned, the default co-ordinate system used for analyzing the governing equation are polar co-ordinates with the radial co-ordinate expressed in r and the angular co-ordinate expressed in θ . As can be seen, the governing equation is nonlinear, sixth order in space and first order in time, implying that six boundary conditions and one initial condition are required to specify the problem completely. The initial condition is straightforward and describes the thickness profile of the fluid film just after all the drops have merged. The boundary conditions are discussed next.

* It must be noted that the primary emphasis of this work is towards nanotopography, which has a spatial wavelength of 0.2mm-20mm and amplitude of ~100nm for polished wafers. This allows for the slope to be negligible locally and permits the use of a global orthogonal co-ordinate system.

2.1.2. Boundary Conditions

Given the presence of a solid-liquid-vapor interface at the boundary, $r = R$, there are a number of boundary conditions possible. The exact nature of the boundary conditions varies with the problem under consideration. These conditions have been divided in two broad categories: (i) Fluid flow related and (ii) Superstrate bending related.

Fluid-flow related boundary conditions specify the value of the pressure or its gradient or both at the periphery. These arise because of the presence of a meniscus and are given by the following:

- i. Pressure differential at fluid interface: $\Delta p(R, t) = \gamma \vec{\nabla} \cdot \hat{n} \sim \gamma \nabla^2 h(R, t)$, where γ is the surface tension of the fluid and $\nabla^2 h$ approximates the curvature of the interface and can be expressed in terms of the contact angles of the resist with the superstrate and the substrate. If the shape of the interface is approximated as a circular arc, the pressure differential is given by $\Delta p(R, t) \sim -\gamma \Phi / h(R, t)$, where $\Phi = 2(\cos(\phi_s) + \cos(\phi_c))$ with ϕ_s and ϕ_c being the contact angles at the substrate-liquid-air and superstrate-liquid-air interface, respectively (Figure 2.3). However, the effect of this condition is usually confined close to the boundary* and does not show up in the bulk.
- ii. Pinned meniscus (zero flow): $\vec{\nabla} p \cdot \hat{n} = 0$. This condition is well-approximated when the meniscus is pinned by the presence of a raised feature, known as ‘mesa’⁸³, on the superstrate. The pinning causes a pressure build-up at the interface, reducing its

* A quick scaling analysis reveals that the length scale across which the interfacial pressure is active, can be given as: $R_p \sim \left(\frac{Dh_R^2}{2\gamma}\right)^{0.25}$, where h_R is the thickness of the fluid film at the interface. For $h_R < 100\text{nm}$, $R_p < 1\text{mm}$, suggesting that this effect is most closely felt at the boundary and may not be seen in the bulk of the film.

curvature and reaching an unstable state, which is relaxed only when the contact line traverses the feature step⁶⁵. This boundary condition has been illustrated in Figure 2.3.

Boundary conditions associated with the bending of the superstrate are given by the deformation, slope, bending moment and shear force on the superstrate at the meniscus location. Some of these conditions are:

- i. Zero deformation or constant height, h_0 , at outer edge: $h(R, t) = h_0$
- ii. Prescribed slope: $\vec{\nabla}h \cdot \hat{n}$, at the boundary. This is given by the overall film thickness profile.
- iii. Shear force: $D\vec{\nabla}\nabla^2h \cdot \hat{n} = -\gamma \sin(\phi_c)$. The shear force on the superstrate is given the unbalanced out-of-plane component of the liquid-air surface tension and relates to the contact angle with the superstrate, as shown in Figure 2.3. The in-plane component of the surface tension is balanced by the surface energies of the superstrate-liquid interface and the superstrate-air interface.

In addition to the boundary conditions, there are dynamic and kinematic constraints that the system can have. These are given by conservation of volume, which assumes negligible losses due to evaporation*, and the application of a constant force on the superstrate as given below:

- i. Constant normal force, F_N , over the active area, A , of the superstrate: $\int_A p dA = F_N$
- ii. Volume conservation: $\int_A h(r, t) dA = V$

* The assumption of negligible evaporation losses is valid for J-CAST, as the liquid-vapor boundary is present only at the outer periphery. This is in contrast with stand-alone inkjetting as has been discussed in Section 1.2.

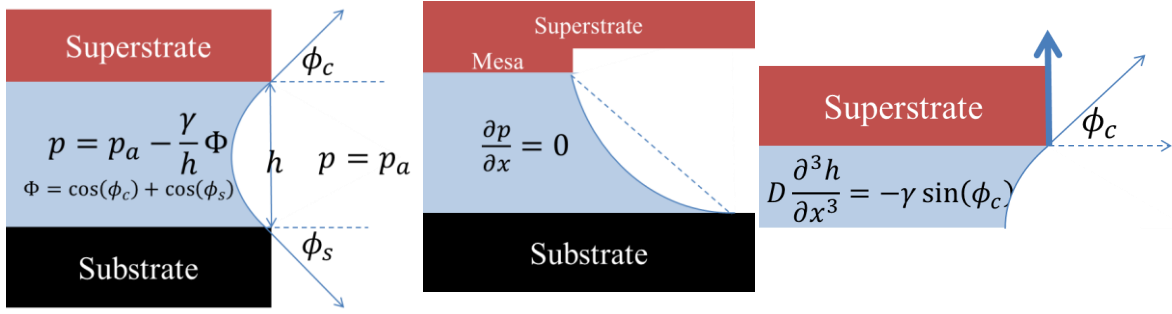


Figure 2.3: Illustration of the following boundary conditions (from left to right): Pressure drop at interface, zero flow due to pinned meniscus and shear force on superstrate. For the pinned meniscus, the dotted line represents the extreme case of zero curvature. For the shear force, the bold arrow indicates the unbalanced component of the surface tension that causes the shear force, while the dashed arrow indicates the balanced component of the same. All illustrations have been made in 1D Cartesian co-ordinates for clarity.

2.1.3. Non-dimensional Problem Formulation

Non-dimensionalization of the governing equation 2.7 can be done by scaling the quantities as follows:

$$\tilde{h} = \frac{h}{h_0}, \tilde{w}_s = \frac{w_s}{h_0}, \tilde{w}_c = \frac{w_c}{h_0}, \tilde{x} = \frac{x}{R}, \tilde{t} = \frac{Dh_0^3 t \pi^6}{12\mu R^6}$$

where $\tilde{\zeta}$ represents the non-dimensional form of the quantity ζ , and R and h_0 are the length scale of the area where the film is deposited and the mean film thickness respectively. Hence, the governing equation becomes independent of scale as:

$$\frac{\partial \tilde{h}}{\partial \tilde{t}} = \vec{\nabla} \cdot \left(\tilde{h}^3 \vec{\nabla} \tilde{h}^4 (\tilde{h} + \tilde{w}_s - \tilde{w}_c) \right) \quad \dots 2.8$$

Although the exact nature of boundary conditions varies with the system under consideration, useful properties of the macroscopic system can be extracted by assuming the spatial boundary conditions to be symmetric and homogeneous. These boundary conditions are given by zero slope, zero shear force and zero flow at the periphery, as given below:

$$\vec{\nabla} h \cdot \hat{n} = \vec{\nabla}^2 h \cdot \hat{n} = \vec{\nabla}^4 h \cdot \hat{n} = 0 \quad \dots 2.9$$

where \hat{n} is the outward normal from the periphery. A symmetric system is an approximation of an infinite spatial domain, which is useful in characterizing the bulk physics of the system in the absence of defined boundary conditions. Given that the actual nonlinear fluid flow related boundary conditions typically exert an influence up to less than 2mm inside the bulk from the periphery, these can be neglected to simplify the system. Moreover, as will be discussed in Section 2.2.2, the film thickness metrology setup has a spot size of ~ 1.5 mm. Therefore, even if these boundary conditions were used, there is insufficient resolution to characterize and validate film thickness profiles close to the boundary. Hence, the use of these boundary conditions is an added expense with minimal added value.

Although symmetry boundary conditions are a mathematical approximation, they are also physically realizable in the system under consideration. A perfectly wetting liquid has zero contact angle which gives rise to zero shear force. The assumption of zero slope at the outer edges holds well if the flow is pinned⁸³, while zero slope is also valid if the desired film thickness profile does not vary at the edge.

2.1.4. Analytical Solutions

A generic analytic solution of equation 2.8 with symmetry boundary conditions is not feasible given the nonlinearity of the problem. However, for the special case of single-mode perturbation in substrate nanotopography, an analytical solution is possible that can give insight into the behavior of the system. For illustration purposes, the coordinate system is chosen to be one-dimensional Cartesian. Expressing the film thickness and superstrate and substrate topography as follows:

$$\tilde{h}(\tilde{x}, \tilde{t}) = 1 + H(\tilde{t})\cos(\pi\tilde{x}) \quad \dots 2.10$$

$$\tilde{w}_s(\tilde{x}) - \tilde{w}_c(\tilde{x}) = W\cos(\pi\tilde{x}) \quad \dots 2.11$$

After plugging the above equations 2.10 and 2.11 in equation 2.8, the time evolution of the film thickness perturbation mode, $H(\tilde{t})$, is given as:

$$\dot{H} = -\frac{1}{4}(4 + 3H^2)(W + H) \quad \dots 2.12$$

where the dot represents the time derivative. The solution to the ordinary differential equation 2.12 is given by:

$$A \log \left(\frac{H(\tilde{t})+W}{H(0)+W} \right) + B \log \left(\frac{\sqrt{3}H(\tilde{t})+2i}{\sqrt{3}H(0)+2i} \right) + C \log \left(\frac{\sqrt{3}H(\tilde{t})-2i}{\sqrt{3}H(0)-2i} \right) = -\frac{3}{4}\tilde{t} \quad \text{where } A = \frac{3\sqrt{3}}{4+3W}, B = \frac{3(W\sqrt{3}i-2)}{4(4+3W)}, C = -\frac{3(W\sqrt{3}i+2)}{4(4+3W)}. \quad \dots 2.13$$

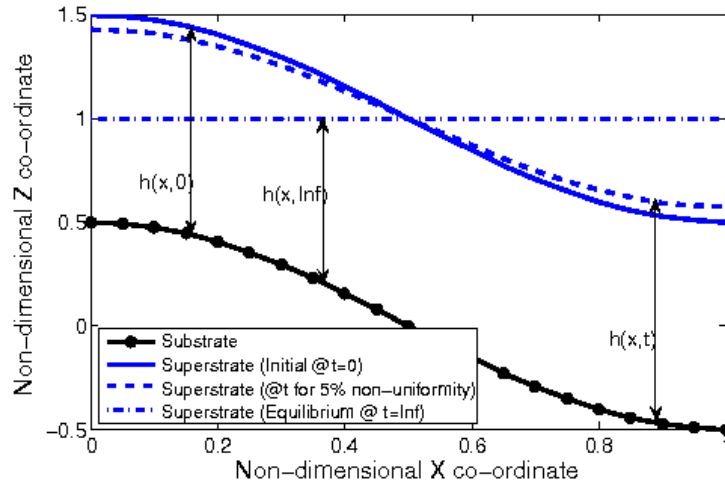


Figure 2.4: Illustration of film thickness evolution in the presence of unimodal topography. The topography is assumed to be manifested in the substrate rather than the superstrate for this case.

For an initial condition of $H(0) = 0$, i.e., a perfectly uniform film, the evolution of the film thickness, driven by the presence of substrate topography, has been illustrated in Figure 2.4. The non-uniformity is defined as the ratio of the standard deviation in the film thickness with the mean film thickness. From the results in Figure 2.5, it can be seen that higher nanotopography amplitude, W , leads to greater corruption of the initial uniformity in the same amount of time. The encountered non-uniformity also increases

with increasing time, as expected, with the equilibrium solution being the farthest from uniformity as $H(\infty) = 1 - W$.

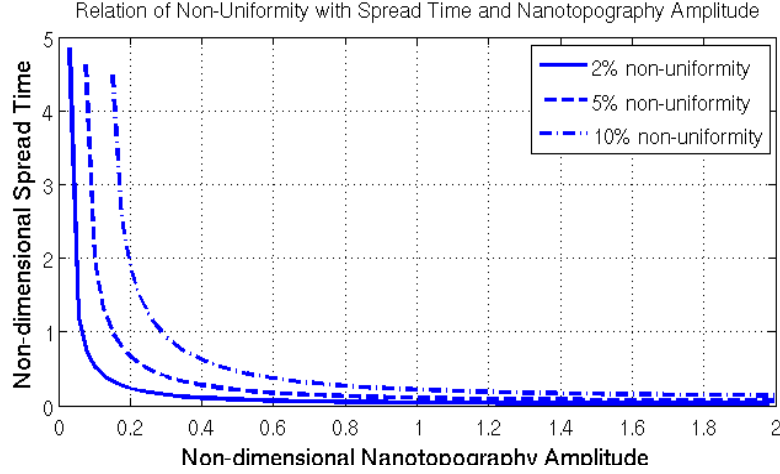


Figure 2.5: Plot showing influence of substrate nanopography and spread time on film thickness non-uniformity.

Increasing number of perturbation modes necessitates the use of approximations to the governing equation for obtaining analytical solutions. First order properties of the governing equation 2.8 can be obtained by conducting a linear analysis with $\tilde{h}(\tilde{r}, \tilde{t}) = 1 + \tilde{\epsilon}(\tilde{r}, \tilde{t})$ where $\|\tilde{\epsilon}\| \ll 1$. A similar study has been conducted in the literature for a fourth order thin film equation⁸⁴. Substituting in equation 2.8 and neglecting higher order terms for $\tilde{\epsilon}$, the linearized equation is given by:

$$\frac{\partial \tilde{\epsilon}}{\partial \tilde{t}} = \tilde{\nabla}^6(\tilde{\epsilon} + \tilde{w}_s - \tilde{w}_c) + 3\tilde{\epsilon}\tilde{\nabla}^6(\tilde{w}_s - \tilde{w}_c) + 3\tilde{\nabla}^2\tilde{\epsilon}\cdot\tilde{\nabla}^4(\tilde{w}_s - \tilde{w}_c) \quad \dots 2.14$$

Similar to unimodal perturbations, the special case of bimodal topography and film thickness perturbations can be considered as follows, with the assumption that the superstrate is perfectly flat:

$$\tilde{\epsilon}(\tilde{x}, \tilde{t}) = E_1(\tilde{t}) \cos(\pi\tilde{x}) + E_2(\tilde{t}) \cos(2\pi\tilde{x}) \quad \dots 2.15$$

$$\tilde{w}_s(\tilde{x}) = W_1 \cos(\pi\tilde{x}) + W_2 \cos(2\pi\tilde{x}) \quad \dots 2.16$$

Upon plugging the above equations 2.15 and 2.16 in the linearized equation 2.14 and using orthogonalization to extract the eigenmodes, the evolution of the film thickness perturbation modes is given as:

$$\dot{E}_1 = -(E_1 + W_1) + \frac{3}{4}(-64E_1W_2 + 2E_2W_1) \quad \dots 2.17$$

$$\dot{E}_2 = -64(E_2 + W_2) - 3E_1W_1 \quad \dots 2.18$$

For the general case, the system of ODEs in equations 2.17 and 2.18 has been solved for analytically, assuming a perfectly uniform initial film, i.e., $E_1(0) = 0$ and $E_2(0) = 0$. From the results in Figure 2.6, it can be observed that the presence of higher-frequency topography, W_2 , can drastically corrupt the uniformity of the evolving fluid film. The saturation observed is associated with the maximum possible non-uniformity that can be encountered given the topography amplitude. With only low-frequency topography, the non-uniformity increases more slowly, thereby, making it easier to obtain uniform films, but more difficult to get the flat profile of the superstrate. This can explain why low-frequency topography, i.e., nanotopography, is difficult to eliminate in fluid-based polishing processes like Chemical-Mechanical Polishing or CMP, as compared to high-frequency topography akin to surface roughness. Hence, there is a need to address the challenge of mitigating low-frequency topography from the point of view of wafer polishing. For the purpose of uniform film deposition, however, the need is conflicting. The aim, here, is to control the signature of higher-frequency topography, so that the obtained film thickness uniformity is not corrupted within short process time scales.

At the same time, it must also be noted that contrary to the assumption in this section, no superstrate surface is perfectly flat. Similar to substrate topography, superstrate topography can also lead to non-uniformity in the evolving fluid film. Getting a signature from the superstrate topography is undesirable from any process perspective,

whether polishing or deposition. The influence of this parasitic also needs to be mitigated.

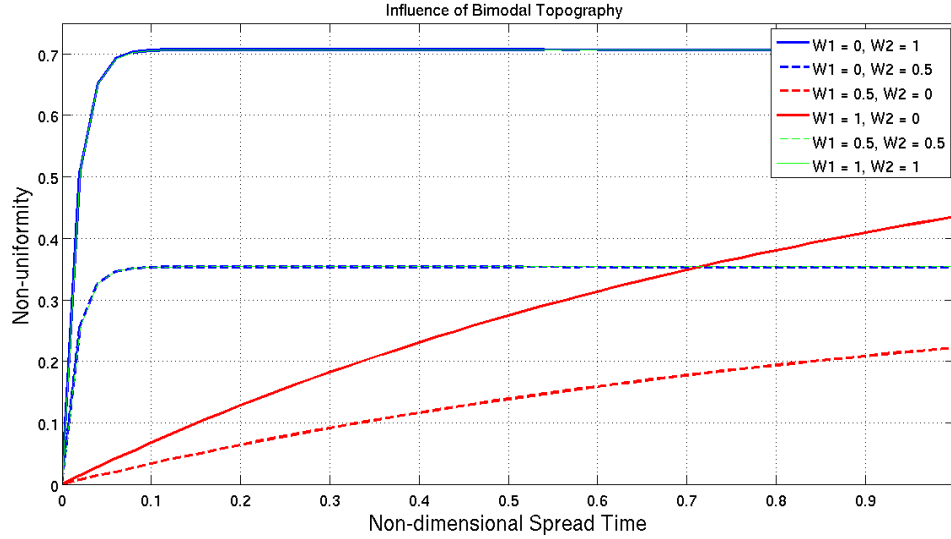


Figure 2.6: Plot of non-uniformity against spread time showing influence of bimodal topography with representative values of topography amplitudes

2.1.5. Numerical Solution Procedure

Given the non-linearity of the governing partial differential equation, a numerical solution was sought by discretization in the spatial and temporal domain. For the spatial grid, spectral methods were preferred over finite difference schemes. This is because spectral methods have exponential global accuracy compared to finite difference schemes⁸⁵. This is important as resolving the sixth-order spatial derivative would require a much finer spatial grid with finite difference schemes. Moreover, spectral methods also combine easily with symmetry boundary conditions and lead to solutions that employ simple separation of variables. The drawback with spectral methods, however, is that their formulation can be more complex compared to finite differences. Because of their reliance on global basis functions, these methods may not accurately resolve locally steep gradients that, however, are not manifested in the system under consideration.

By using spectral methods, the governing partial differential equation is converted into a set of ordinary differential equations. The general approach chosen is similar to the Galerkin formulation, which approximates the solution as:

$$h(r, t) = \eta(r) + \sum C_n(t) \Psi_n(r) \quad \dots 2.19$$

In the above equation, $\eta(r)$ captures information from the boundary conditions and other time-independent spatial constraints, $\Psi_n(r)$ is a spatial eigenfunction with the corresponding n^{th} eigenvalue, and $C_n(t)$ is the corresponding time-dependent coefficient. Some typical eigenfunctions include trigonometric expansions for Cartesian co-ordinates and Bessel functions for radial co-ordinates⁸⁶. For homogeneous boundary conditions, $\eta(r) = 0$, thereby leading to a variable-separated form for equation 2.19. Exploiting the orthogonality of the eigenfunctions, the individual coefficients, are extracted as:

$$C_n(t) = K(R) \int_0^R h(r, t) \Psi_n^*(r) dr \quad \dots 2.20$$

where $K(R)$ is a value dependent on R , and Ψ_n^* is the corresponding orthogonal function to Ψ_n . For example, in a single Cartesian dimension, $\Psi_n = e^{\frac{inx}{R}}$ is a possible eigenfunction. Then, $K(R) = \frac{2}{R}$ and $\Psi_n^* = e^{-\frac{inx}{R}}$. This formulation leads to a system of ordinary differential equations that can yield the temporal evolution of the coefficients, $C_n(t)$.

Like spatial discretization, there are several options available for time stepping as well. These methods can be broadly categorized as explicit and implicit schemes⁸⁵. Explicit schemes use historical and current data to evolve the system at the next time step, such that the value of the variable at the next time step is solved for explicitly. As a representative example, a first-order accurate discretization has been given below for the system, $\frac{d\zeta}{dt} = f(\zeta)$, to highlight the concept:

$$\frac{d\zeta}{dt}_{t=t_n} \sim \frac{\zeta(t_{n+1}) - \zeta(t_n)}{\Delta t} = f(\zeta(t_n)) \Rightarrow \zeta(t_{n+1}) = \zeta(t_n) + f(\zeta(t_n)) \Delta t \quad \dots 2.21$$

These schemes are simple to devise and solve for. However, for partial differential equations, the maximum time-step required to obtain a stable temporal solution is coupled with the smallest spatial step as $\Delta t_{max} \propto \Delta x_{min}^n$, where n is the highest order spatial derivative. The proportionality is defined as per the Courant-Friedrich-Levy or CFL number constraint⁸⁵. For the system under consideration, $n = 6$. This implies that the maximum allowable time step that can be used is drastically reduced if the spatial grid is made fine to resolve the sixth-order derivative accurately. Clearly, even though the solution scheme is simple, explicit schemes for this system can be a substantial burden computationally, unless the spatial grid is coarse. Hence, it becomes all the more reasonable to use spectral methods for spatial discretization as these schemes can yield the solution within the desired tolerance values with a much coarser grid than finite difference schemes.

On the other hand, for implicit time-stepping schemes, the value of the variable at the next time step is not known at the end of a time step calculation. Using the same dummy system, a first order implicit scheme can be constructed as follows:

$$\frac{d\zeta}{dt}_{t=t_n} \sim \frac{\zeta(t_{n+1}) - \zeta(t_n)}{\Delta t} = f(\zeta(t_{n+1})) \Rightarrow \zeta(t_{n+1}) - f(\zeta(t_{n+1}))\Delta t = \zeta(t_n) \quad \dots 2.22$$

It is easily observed that the value of $\zeta(t_{n+1})$ is not known explicitly for each time step. The advantage of this scheme is that the stringent CFL number constraint, that is present for explicit methods, is no longer valid. This allows much larger time steps that can ease the computational burden. An implicit construction leads to an algebraic equation for each time step that must be solved for to get the temporal evolution. For non-linear $f(\zeta)$, as is present for the current system, solving this algebraic equation may need an iterative numerical procedure itself, which can increase the computational expense and negate the benefits of a larger time step. As will be discussed in the ensuing sections, both explicit

and implicit schemes have been used in this work as defined by the associated spatial grid.

2.2. PRELIMINARY EXPERIMENTS

The analytical solutions of simplified models provide insight into the behavior of the system. To support this insight, qualitative verification of the model predictions has been done with the help of preliminary experiments.

2.2.1. Experimental Methods

The primary purpose of the preliminary experiments was to understand how final film thickness uniformity in the presence of common wafer topography is affected by the following process control parameters: superstrate thickness, average film thickness and spread time

The choice of these parameters was governed by the ease with which these could be changed. Increasing the mean film thickness meant either dispensing more volume or similar volume drops spaced closer together. Blank fused silica substrates of two different thicknesses - 0.525mm and 0.7mm - were chosen for varying superstrate thickness. The spread time was changed by delaying or hastening UV exposure. Table 2.1 details the values of the parameters used in these experiments.

Table 2.1: Experimental conditions and results from preliminary experiments for uniform thin film deposition.

Case #	Superstrate thickness (μm)	Target film thickness (nm)	Spread time (s)	Obtained film thickness mean (nm)	Obtain film thickness std. dev. (nm)	Obtained non-uniformity
0	700	26	100	22.45 +/- 0.8	0.98 +/- 0.09	4.37 %
1	700	26	<u>10</u>	21.42 +/- 1.64	0.77 +/- 0.2	3.59 %
2	<u>525</u>	26	100	20.79 +/- 0.99	0.77 +/- 0.1	3.70 %
3	700	<u>78</u>	100	73.11 +/- 0.58	3.78 +/- 0.31	5.17 %

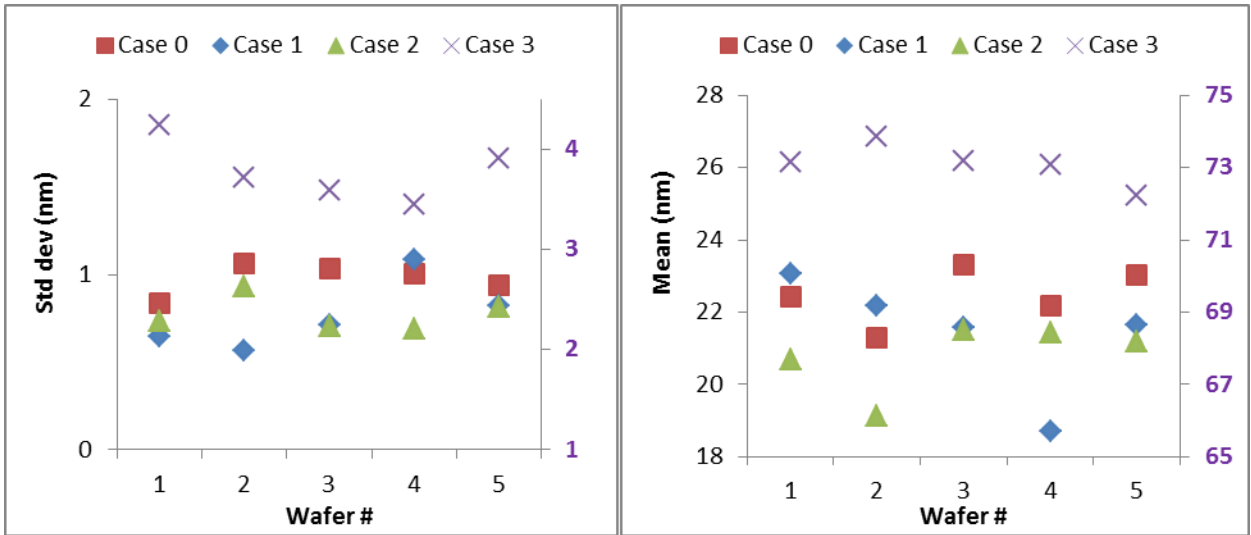


Figure 2.7: Plots of the standard deviation in the film thickness (left) and mean film thickness (right) for each of the 5 samples considered for the analysis. The results for case 3 should be read off the y-axis on the right, whereas the same for cases 0, 1 and 2 should be interpreted from the y-axis on the left.

2.2.2. Metrology Methods

The thickness of the film was measured on a MetroSol VUV optical film thickness measurement system, which has a spot size of 1.5 mm diameter. The film thickness was measured along the imprint area diameter (typically 60 mm) that is normal to the wafer flat at a pitch of 1 mm, leading to 61 measurement points. As explained in Figure 2.8, this direction is chosen since it is not corrupted by noise due to variability caused by the operation of different nozzles. In other words, drops are dispensed by the same inkjet nozzle along this line and hence, film thickness metrology in this direction represents a more accurate picture of the process result.

For analysing film thickness uniformity, a statistical procedure using Chauvenet's criterion was used to reject outliers from the data and to report the mean and standard deviation in the measurements⁸⁷. Chauvenet's criterion defines an acceptable range of the data around the sample mean, given the number of measurements. Specifically, all points

that fall within a probability band of $1 - \frac{1}{2N}$ around the mean value, μ , should be retained and the rest rejected as outliers, assuming that the sample distribution is Gaussian. For 61 sample points, this comes out to a probability of 0.9918 around μ , which for a two-tailed Gaussian distribution, corresponds to a maximum tolerance of 2.64 times the sample standard deviation, σ . Hence, any measurement value falling outside the band of $\mu \pm 2.64\sigma$ is rejected as an outlier. This procedure is conducted only once and not repeated again.

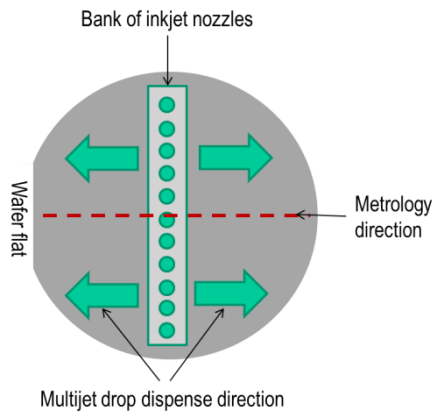


Figure 2.8: Illustration of the normal to flat direction along which all measurements have been taken. Since the bank of inkjet nozzles or multijet scans the wafer in the direction parallel to the flat to dispense drops the same nozzle dispenses along the normal to flat direction. Hence, there is little variability in this direction, as compared to the parallel to flat direction where there can be variability due to different nozzles dispensing drops.

2.2.3. Results

The departure from uniformity is estimated by the obtained non-uniformity, i.e., the ratio of standard deviation with the mean film thickness. Five samples for each case were analyzed as shown in the plots in Figure 2.7. Table 2.1 reports the obtained mean film thickness and standard deviation along with their deviation across the 5 samples. The film thickness for each case is the average of the mean film thickness of each of the 5 samples considered. Similarly, the standard deviation is the average of the standard

deviation in the film thickness of the 5 samples for each case. The obtained non-uniformity is the ratio of the obtained standard deviation average with the obtained mean film thickness average. For cases 1, 2 and 3, the parametric change from the nominal case 0 has been underlined.

The baseline case 0 has been chosen as the 26nm* uniform film thickness with a 0.7mm thick superstrate evolved for 100 seconds. As is observed, lowering the spread time to 10 seconds (case 1) and superstrate thickness to 0.525mm (case 2) helps reduce the non-uniformity. On the other hand, increasing the film thickness to 78 nm† (case 3) increases the non-uniformity. This is corroborated visually in Figure 2.9. An increase in non-uniformity is correlated with an increase in the granularity of the image, thereby suggesting that even though equal volume of drops were dispensed, significant fluid redistribution takes place that corrupts the inherent uniformity in the films.⁸⁸

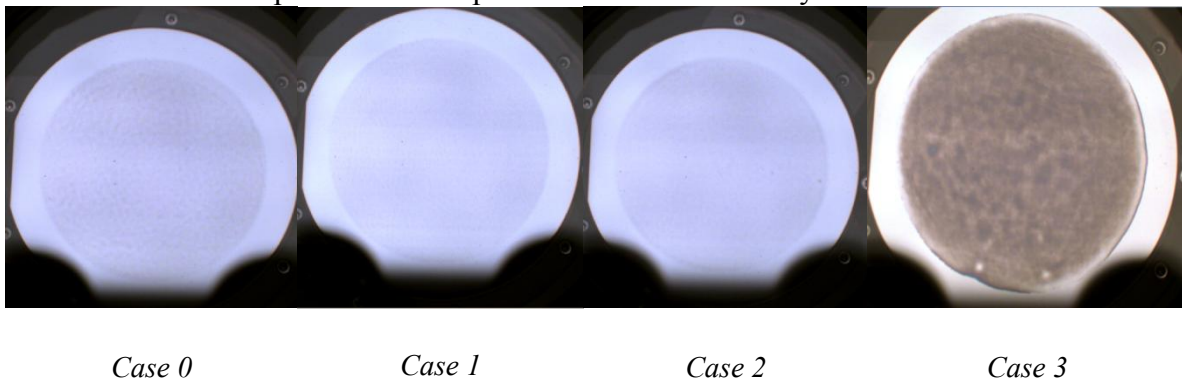


Figure 2.9: Picture of a sample each from the respective preliminary experiment cases.

* A film of 26nm target thickness is usually obtained by dispensing 6pl drops at a pitch of 422.5 μ m. In the given experiment, partial clogging of the inkjet nozzles resulted in a lower than expected thickness of ~21nm.

† Similarly, a 78nm thick film is usually obtained by dispensing 6pl drops at a pitch of 253.5 μ m. Here, too, the obtained lower than expected mean value of ~73nm was attributed to partially clogged nozzles.

2.2.4. Inference

From the preliminary experiments, it is evident that increasing the fluid film thickness, h_0 , superstrate thickness, b , and spread time, t , increases the obtained non-uniformity. Moreover, analytical results of the simplified models in Section 2.1.4 suggest that an increase in non-dimensional time, \tilde{t} , leads to an increase in the non-uniformity, irrespective of the amplitude(s) of the underlying topography. From non-dimensionalization, it can be seen that the characteristic process time scale is given as:

$$\tau = \frac{144R^6\mu(1-\nu^2)}{\pi^6Eb^3h_0^3} \quad \dots 2.23$$

The ratio of spread time with this time constant leads to non-dimensional spread time, which, thereby depends on all the process parameters of interest as:

$$\tilde{t} = \frac{\pi^6Eb^3h_0^3t}{144R^6\mu(1-\nu^2)} \quad \dots 2.24$$

This non-dimensional spread time brings out a powerful relationship between the process parameters and the tendency for fluid re-distribution. Increasing the thickness of the superstrate, mean film thickness or process spread time increases this non-dimensional spread time, leading to rapid re-distribution of the fluid and compromising uniformity. Hence, the qualitative trend given by the simplified analytical models agrees well with the experimentally obtained results.

The non-dimensional spread time also brings out the relative sensitivity of each process parameter. For example, the dependence on superstrate thickness is cubic. This implies that a three-fold reduction in thickness can make a 27 fold reduction in the value. For the same re-distribution characteristics, this implies that a thicker film can be tolerated. Moreover, the process window is lengthened, thereby, making it possible to capture the transients without the influence of parasitic topography that would otherwise have been impossible with the thicker superstrate. The other important inference that can

be derived is that the non-dimensional spread time is strongly dependent (sixth-order) on the wave number. Perturbations with larger length scales or shorter wave numbers decay slower than perturbations with smaller length scales or larger wave numbers. This is expected as the superstrate tries to attain its equilibrium flat configuration and dissipates its strain energy through the viscosity of the liquid. The smaller wavelength perturbations indicate higher strain energy in the superstrate, thus driving it towards equilibrium faster. It should also be noted that although capillarity influences the initial spreading and merging of dispensed drops, the surface tension of the liquid does not influence the non-dimensional spread time, as it is a boundary effect.

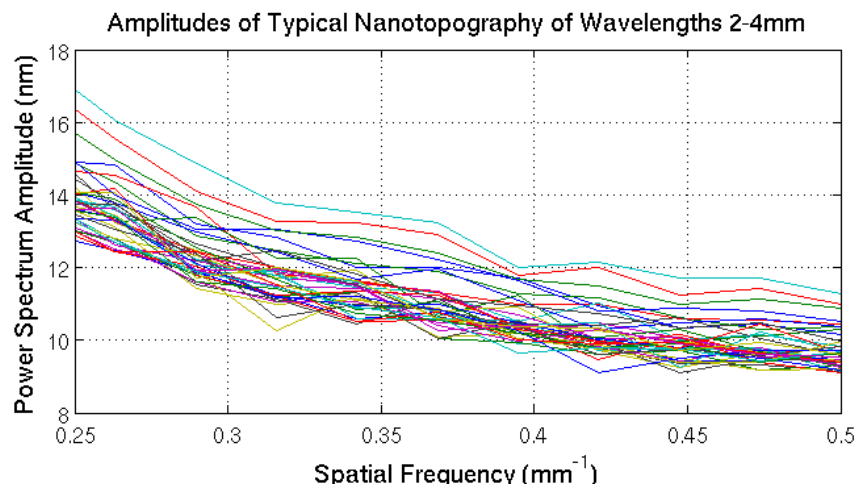


Figure 2.10: Plot showing the amplitude distribution for different spatial frequencies as measured across different line scans on the Zygo optical surface profiler

Given the influence of each process parameter on the non-dimensional spread time, the analytically obtained results were also compared quantitatively with the experimentally obtained values of non-uniformity. Since the film thickness measurements were done at a pitch of 1mm, the minimum wavelength for analyzing nanotopography amplitude was set at 2mm. Measurement of nanotopography was undertaken on a Zygo

optical surface profiler. It is capable of higher lateral resolution metrology, but was deliberately constrained for this analysis. Figure 2.10 shows the power spectrum amplitudes of nanotopography wavelengths ranging from 2mm - 4mm for typical wafer scans on the Zygo. These amplitudes vary from about 10nm - 15nm.

As an example for comparing the results for unimodal topography in equation 2.13, a spatial wavelength of 2.5mm was chosen. Plugging in the process parameters for the nominal case 0 and case 1 (Table 2.1) reveals that 2% non-uniformity is encountered in ~ 100 s of spread time for nanotopography amplitudes of ~ 10 nm. Although the deviation from uniformity is under-estimated, it is close to that seen in the preliminary experiments. Similarly, for case 3, about 8% non-uniformity is encountered in ~ 100 s of spread time for the same nanotopography amplitudes. This is an over-estimation of the deviation from uniformity. Extending the above comparison to the results for bimodal topography of wavelengths 2mm and 4mm reveals that the non-uniformity for all cases is of the same order of magnitude, but over-estimated. Hence, it was concluded that although the simplified models give a good estimate of the corruption of uniformity, controlled validation of the full-blown thin film evolution model, with the associated substrate topography, was needed to establish the parametric dependence on non-uniformity. This requires simulating the complete nonlinear system numerically using the procedure described in Section 2.1.5.

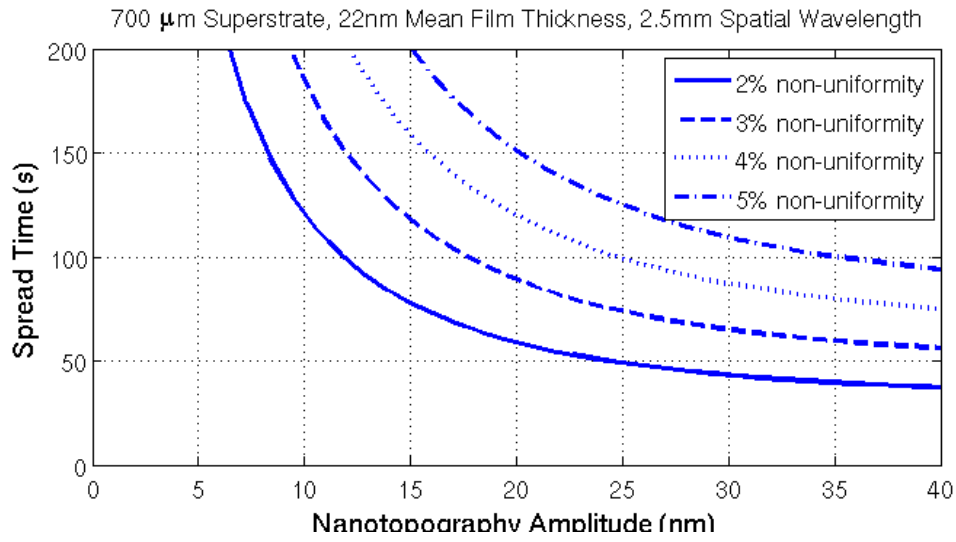


Figure 2.11: Film thickness non-uniformity variation with spread time and one-dimensional nanotopography amplitude of 2.5 mm spatial wavelength for cases 0 and 1

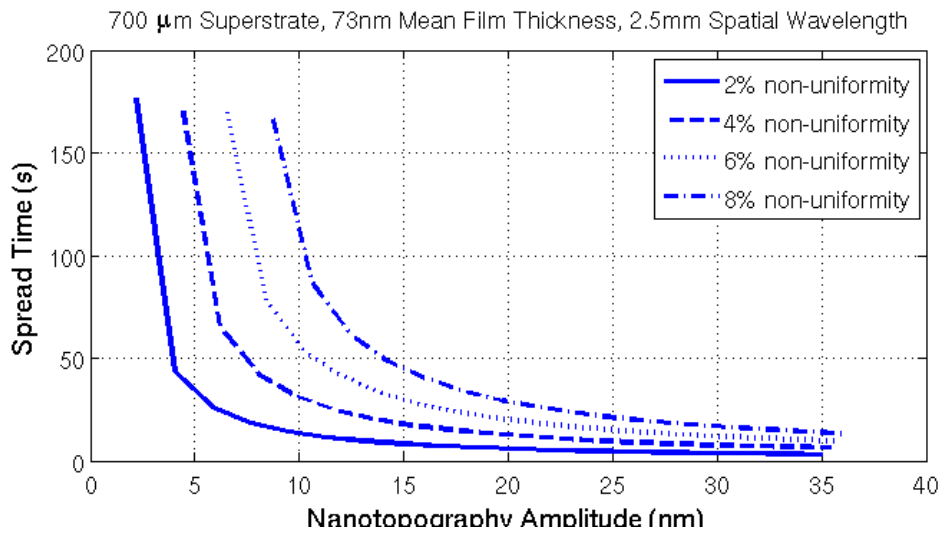


Figure 2.12: Film thickness non-uniformity variation with spread time and one-dimensional nanotopography amplitude of 2.5 mm spatial wavelength for case 3

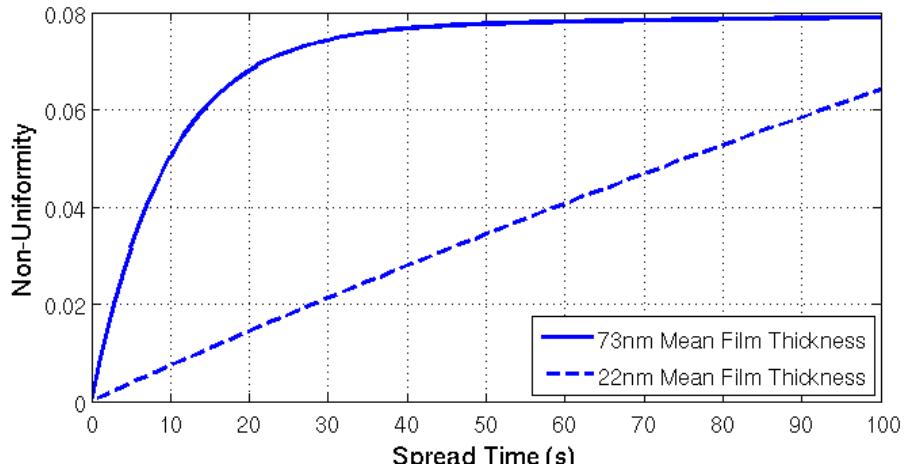


Figure 2.13: Film thickness non-uniformity variation with spread time and two-dimensional nanopography amplitudes of 10nm and 14nm, of spatial wavelengths 4mm and 2mm, respectively, for mean film thicknesses of 22nm and 73nm

2.3. VALIDATION OF BASELINE MODEL

For validating the thin film evolution model, a set of experiments were conducted with the same superstrate thickness, same target film thickness and with a superstrate having a raised mesa edge which pinned the fluid at the outer boundary thereby approximating a zero-flow homogeneous boundary condition. The experiments were conducted on thirteen single-side polished 4” Si wafers. Three different spread times of 30s, 45s and 125s were chosen. The topography of each of the thirteen substrates was measured on a Zygo optical surface profiler.

To prevent variability in substrate topography from corrupting the results, the experiments were conducted on the same set of thirteen substrates. The mean film thickness and standard deviation for each of the 13 wafers and spread time have been plotted in Figure 2.14 and Figure 2.15, respectively. The substrates were reclaimed, i.e., the cured polymer was removed using wet polymer etching after each spread time experiment. The first spread time point, i.e. 30s, was used as the initial condition for the thin film evolution model in two different versions: (i) Linearized model (equation 2.14)

without topography, i.e., $w_s = 0$ and $w_c = 0^*$, for which no verification is required as it has an analytical solution and (ii) Full nonlinear model with topography (equation 2.8). Numerical verification for a similar nonlinear model with non-homogeneous boundary conditions has been shown in Section 3.3.3.

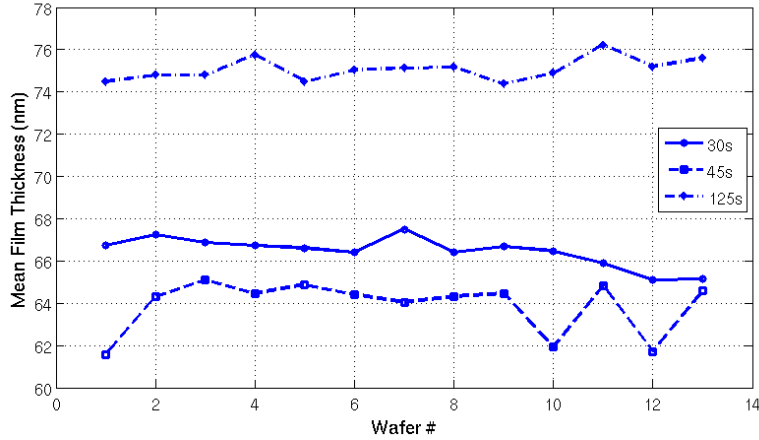


Figure 2.14: Mean film thickness across each wafer used for experimental validation

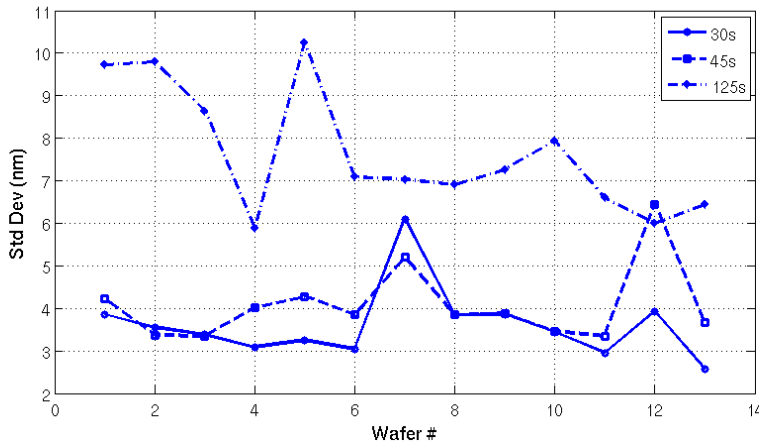


Figure 2.15: Standard deviation associated with the mean film thickness across each wafer used for experimental validation.

* The solution for the n^{th} perturbation eigenmode in the absence of any topography is given as: $E_n(\tilde{t}) = E_n(0)\exp(-n^6\tilde{t})$

To incorporate the effect of film thickness variation in the angular direction, the model was modified to include the presence of these variations by augmenting the pure radial eigenfunctions as follows:

$$\Psi_{mn}(r, \theta) = J_n(k_m r) e^{in\theta}, \text{ such that } h^*(r, \theta, t) = \sum_{m=1}^M \sum_{n=1}^N H_{mn}(t) \Psi_{mn}(r, \theta) \quad \dots 2.25$$

where $J_n(k_m r)$ is the n^{th} order Bessel function of the first kind with the m^{th} eigenvalue and $e^{in\theta}$ represents the eigenfunction for the angular co-ordinate, and $h^*(r, \theta, t)$ is the reconstructed film thickness profile using the spectral expansion. Metrology was conducted on the same 121 sites for each wafer at each spread time, so as to maintain consistency. Given that each spread time experiment was performed at different times, random experimental and metrology errors were a concern. To this end, the film thickness and wafer topography metrology information at each of the 121 measurement sites was averaged across all 13 wafers for each spread time. This site-averaged case for the spread time of 30s was set as the initial condition along with the site-averaged substrate topography as input.

The maximum number of eigenmodes was decided by the metrology recipe. The 121 measurement locations were distributed such that there were 12 equi-spaced locations along the radial co-ordinate for each angle, with 10 equi-spaced angular steps for each radius. Adding a location at the origin gave the total of 121 locations. Given this spatial distribution of the measurement locations, $M = 12$ eigenmodes were chosen for the radial co-ordinate and $N = 10$ for the angular co-ordinate. Following this choice of number of eigenmodes, $h^*(r, \theta, t)$ was computed using the averaged experimental data, $h(r, \theta, t)$ and compared against it for the initial condition of $t = 30\text{s}$, as verification of the spectral expansion exercise. The residuals between the reconstructed and actual data are plotted in Figure 2.16, and are as small as machine precision. This implies that there is no

error in the transformation of the data into the spectral domain and serves as a simple verification exercise for the same.

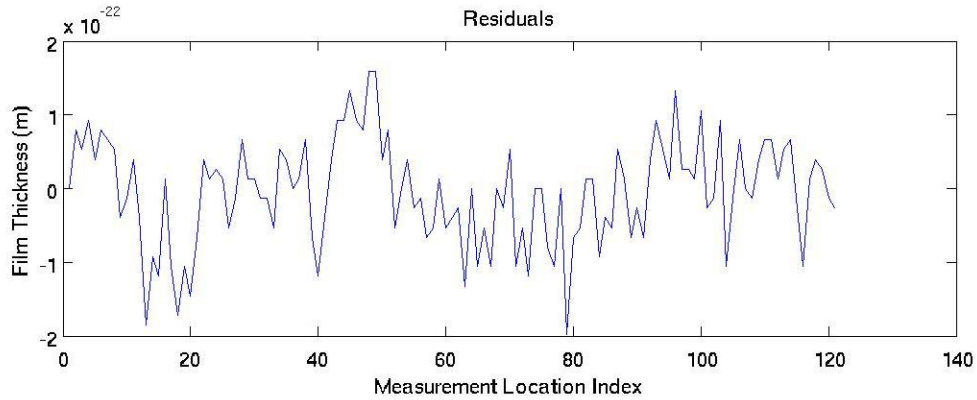


Figure 2.16: Residuals between the actual and reconstructed data at the initial condition.

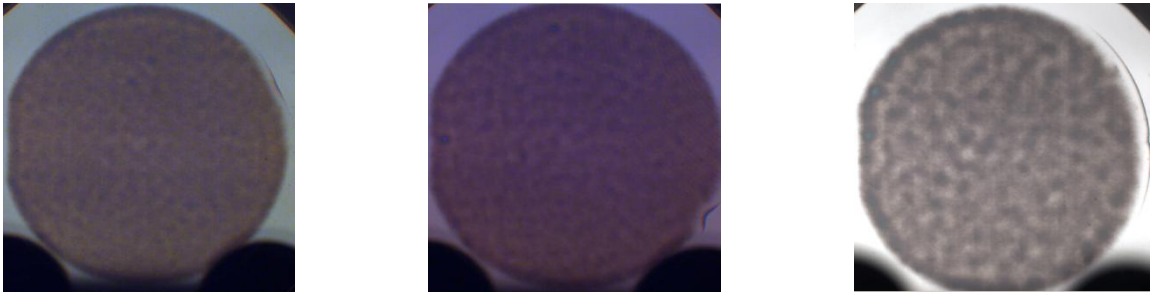


Figure 2.17: (From L to R) Pictures of the same wafer at the spread times of 30s (initial condition), 45s & 125s

The initial condition at 30s was evolved to 45 s and 125 s using the two models described earlier and then compared against site-averaged experimental data. Example pictures of the same wafer at the three different spread times have been shown in Figure 2.17. The results from the two different model versions along with the experimental results have been plotted in Figure 2.18, while wafer contour maps of the model predictions and experimental results have been shown in Figure 2.19.

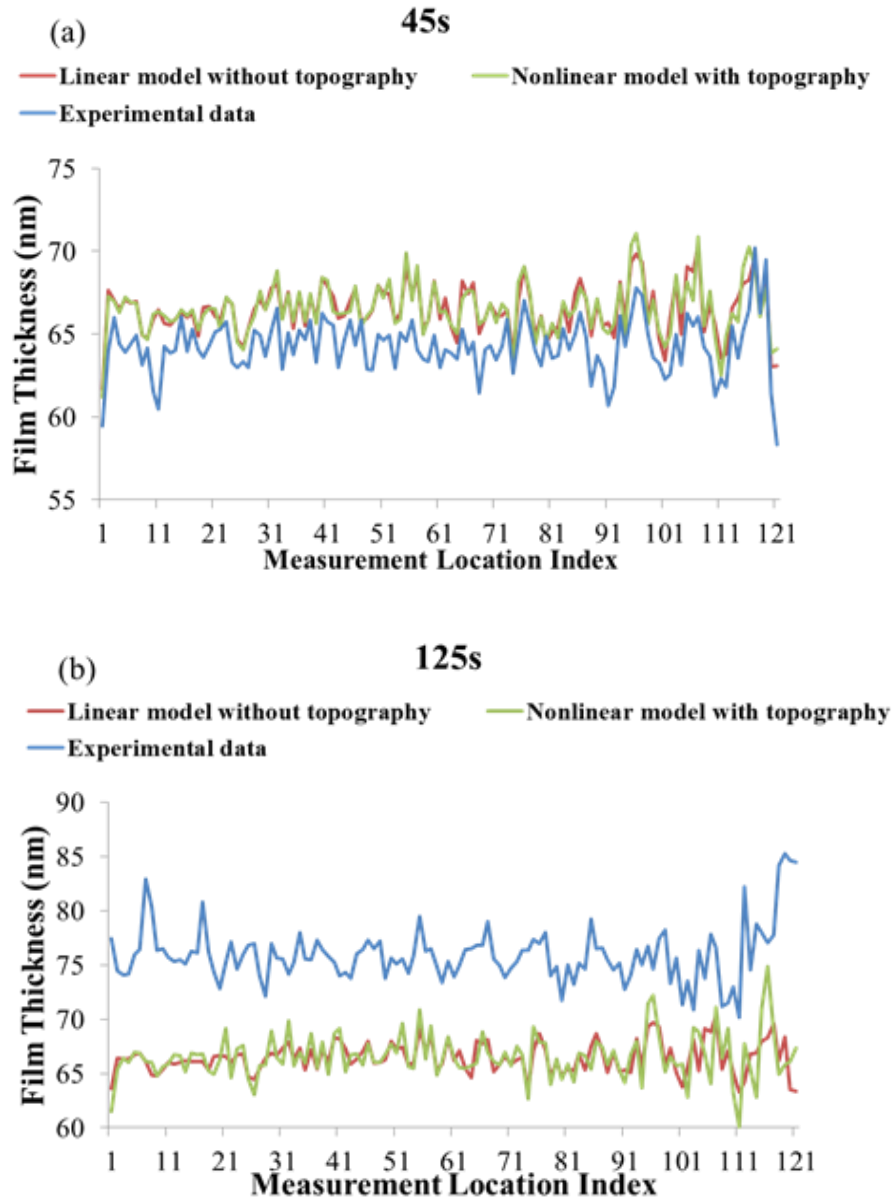


Figure 2.18: Plots comparing the experimental results against each of the two model versions for the spread times of (a)45s and (b)125s. The initial condition for the models is the film thickness obtained at a spread time of 30s.

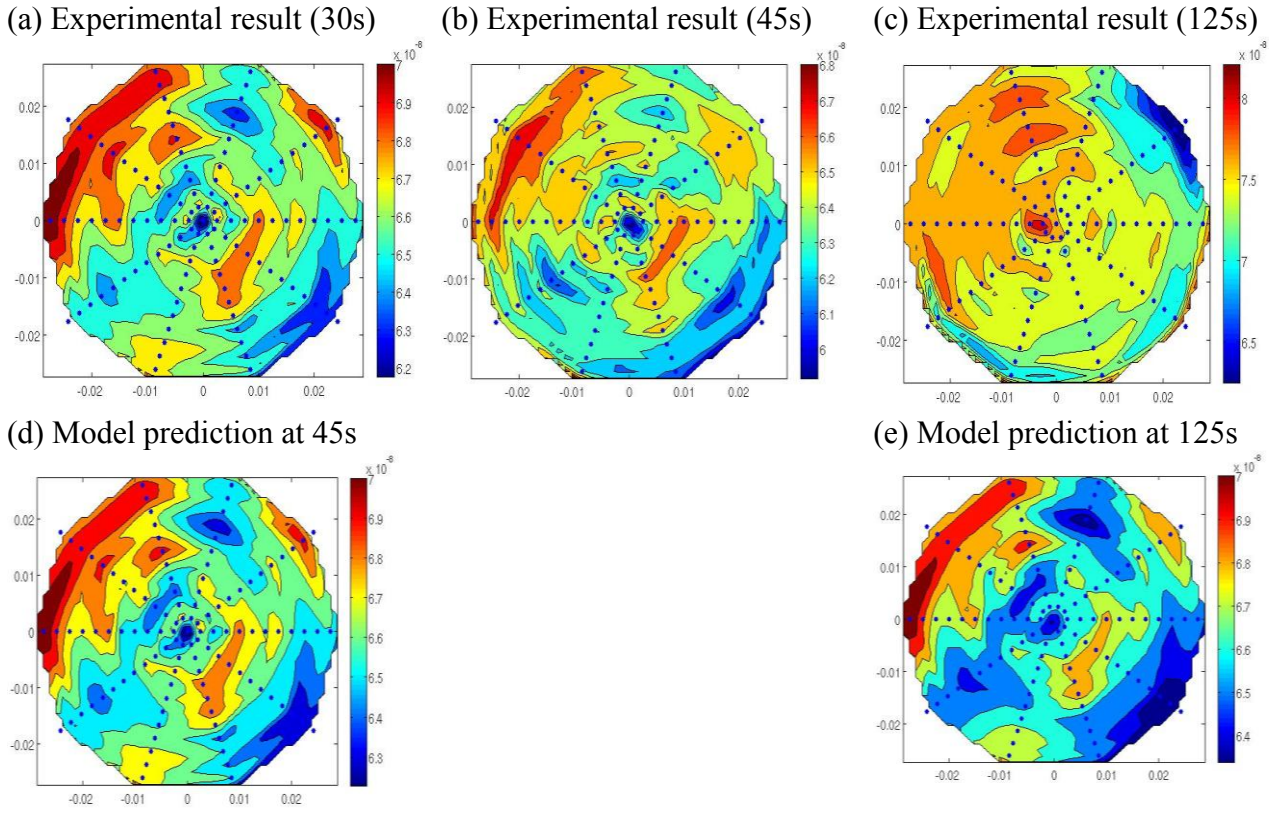


Figure 2.19: Plots depicting experimental validation of the linearized model for uniform films. For the contour plots, the blue dots indicate the metrology sites. The measurement locations are indexed from the center radially outwards. Measurement location index 1 is the origin, 2-11 at a radius of 2.5 mm spaced every 36 degrees, 12-21 at a radius of 5 mm with the same angular pitch, and so on.

Although the spatial trends agree well with the experimental data, it is also observed that due to uncontrolled perturbations in the inkjet dispenser, the experimentally obtained mean film thicknesses across the three spread times were different. Accurate comparison of the model prediction against the experimental data requires the mean film thickness to be the same. Hence, for each of the two spread times of 45 s and 125 s, the mean offset with the initial condition of 30s was first calculated. This offset was ~ 2 nm for the 45 s case and ~ 10 nm for the 125 s case. Then, the experimental data of 30s was corrected using the respective mean offsets, and set as the initial condition for model

evolution to the respective spread times. Following this correction, the RMS error is reduced significantly to ~ 1.2 nm and ~ 3 nm for the 45 s and 125 s cases respectively, for both model versions. These values are less than 5% of the mean film thickness, which is also the scale of variability observed when performing the wafer-wafer averaging of the film thickness profile.

The evolution of non-uniformity is summarized in Table 2.2. From the results, it can be seen that the experimental data matches well with both versions of the model for the lower spread time of 45s. However, for the higher spread time of 125s, the linearized model without topography does not agree well with the experimental data. In fact, as can be seen from Figure 2.20, the non-uniformity decreases with increasing spread time for the linearized model without topography, which is expected. The same for the nonlinear model with topography shows increasing non-uniformity with increasing spread time, which corroborates with the experimental data. Hence, the full nonlinear model without topography is a closer match to the actual physical scenario. But, if the spread time is kept 'small', i.e., less than 20s relative to the initial spread time of 30s in this case, the difference between the two models is $\sim 0.2\%$, which is of about 10% of the nominal non-uniformity. This is desirable as the linearized model without topography can be solved analytically thereby drastically reducing computational complexity. Hence, for substrates with similar nanotopography profiles, it suffices to use the linearized model without topography. The model is thus deemed validated.

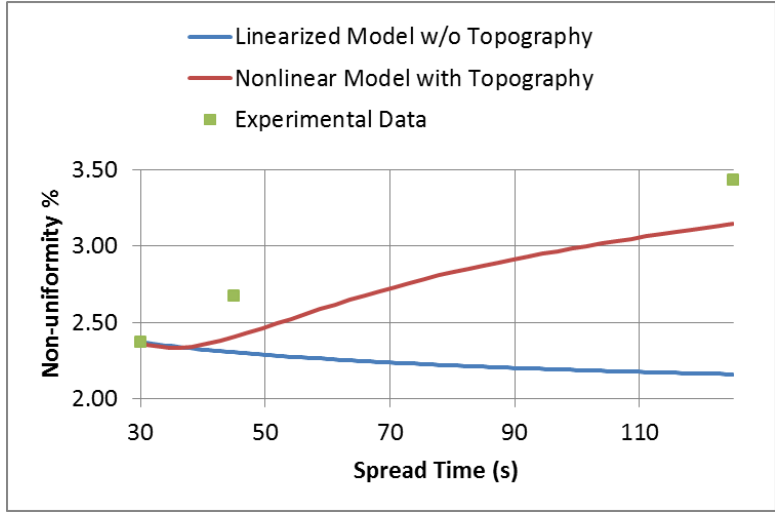


Figure 2.20: Plot showing the evolution of non-uniformity for both model versions and experimental data.

Table 2.2: Summary of non-uniformity encountered in the experiments and the same predicted by the models.

	Experimental	Linearized Model w/o Topography	Nonlinear Model w/ Topography
t = 30s	2.37 %	Initial Condition	
t = 45s	2.67 %	2.30 %	2.40 %
t = 125s	3.43 %	2.16 %	3.14 %

2.4. SUMMARY

In this chapter, a baseline model for the superstrate-fluid-substrate sandwich has been developed. The influence of various process parameters on the temporal evolution of the system has been captured with the help of a characteristic process time scale. Analytical solutions for special cases of the system have been obtained to reveal the influence of parasitic topography on the evolution dynamics. Appropriate numerical procedures for solving the nonlinear system have been identified, with the help of which experimental validation of the system has been successfully conducted.

Chapter 3: Deposition of Highly Uniform Films

After validation of the baseline model that can predict the time evolution of the substrate-fluid-superstrate sandwich in the presence of topography, it is important to test the conclusions of the model by depositing films of uniform thickness. The aim is to obtain substantially lower non-uniformity, with standard deviation of less than 2% of the mean film thickness, than that previously obtained in the preliminary experiments discussed in Section 2.2. Deposition of highly uniform nanoscale thin films with minimal waste has several applications, including, anti-reflection coatings for products like solar cells and bottom anti-reflection coatings (BARCs) for semiconductor devices^{89,90,91}. For solar cells, these coatings ensure that maximum light is trapped in the cell to enable maximum charge generation. In photolithography, BARCs are necessary to avoid formation of standing wave artifacts that corrupt critical dimensions of features. Moreover, anti-reflection coatings are sometimes needed as multiple layers, thereby strengthening the case for use of J-CAST to minimize fiscal and environmental cost.

The need for highly uniform films of ~100nm also arises in the area of biomedical engineering, where there is a need to produce monodisperse nanoparticles for efficient drug delivery. However, most bio-functional materials tend to be more viscous than the UV curable monomer used for this work. The high viscosity makes inkjetting of smaller volume drops difficult. Hence, these drops need to be spaced farther apart to ensure films of ~100 nm thickness, which can lead to undesired non-uniformity. A brief investigation has been conducted into the influence of drop spacing and volume on film thickness non-uniformity by extending the baseline model to study a simplified drop spreading process. The conclusions of the model have been qualitatively validated using simple experiments, thus enabling the use of J-CAST to generate uniform films with large drop volumes.

3.1. CHANGING PROCESS TIME SCALE

In the previous chapter, it was observed that reducing the non-dimensional spread time is necessary for reducing the non-uniformity stemming from the presence of parasitics like surface topography. Achieving the above by reducing the physical spread time is not desirable as it decreases the physical process control window. Hence, the more suitable approach is to increase the denominator or the process time scale, such that there is an automatic decrease in the non-dimensional spread time with physically realizable process times.

From equation 2.23, the process time scale can be reduced in the following possible ways: (i) increasing the fluid viscosity, (ii) reducing the mean film thickness, (iii) increasing the characteristic lateral length scale, (iv) reducing the Young's modulus of the superstrate material, and (v) reducing the thickness of the superstrate. Option (i) is not feasible given that the fluid properties have to be optimized for spreading, merging and photo-polymerization in conjunction with film evolution and these constraints can override the requirement of low viscosity. The mean film thickness and characteristic length scale in options (ii) and (iii) above are governed by the deposition requirement and hence, cannot be controlled as a process parameter. The superstrate material in option (iv) is optimized for transparency to UV light, drop spreading and separation from the polymerized film after cross-linking. Hence, the only feasible parameter that can be modified is the geometry of the superstrate by way of its thickness or option (v).

3.1.1. Reducing Thickness of Superstrate

A standard superstrate is made of fused silica and has a diameter of 150mm. Since fused silica substrates are not available off the shelf in thicknesses lower than 525 um, a customized superstrate was fabricated out-of-house. The central region of a standard 525 micron superstrate was cored out across a diameter of 80mm by a combination of etching

and polishing techniques, to a thickness of 250 μm . The cross section of the cored superstrate is given in Figure 3.1. This enabled the superstrate to retain its strength and rigidity at the edges where it is vacuum chucked, yet remain flexible close to the center where it actually contacts the fluid film.

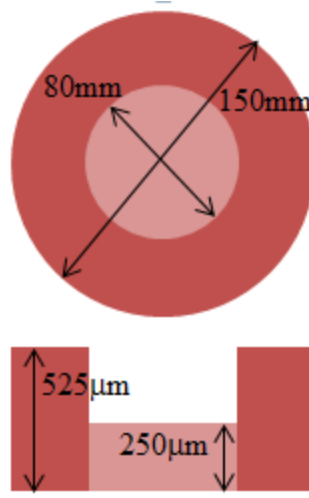


Figure 3.1: Illustration (not-to-scale) of geometry of 250 μm cored superstrate. The lighter region is where the superstrate interacts with the fluid.

3.2. UNIFORM FILM DEPOSITION WITH THIN SUPERSTRATE

Since it is expected that thin superstrates can lead to better film uniformity, a target standard deviation of less than 2% of the mean film thickness was chosen. This is upto 3X better than those obtained in the preliminary experiments with thicker superstrates. To this end, similar drop volumes of $\sim 6\text{pl}$ were dispensed and merged under the action of the thin 250 μm cored superstrate. The metrology was done similar to the procedure described in Section 2.2.2.

3.2.1. Experimental Results

Similar film thicknesses as obtained in the preliminary experiments with thicker superstrates were targeted with a thin superstrate. As can be seen from the results in

Table 3.1, the standard deviations obtained are much lower when compared with Table 2.1. The aim of the process is to enable robust deposition of highly uniform films of thicknesses ranging from $\sim 20\text{nm}$ – $\sim 1\mu\text{m}$. But, as predicted by the model, higher mean film thicknesses should increase the non-uniformity, which might compromise with the acceptable limit of $< 2\%$. Moreover, metrology becomes inconsistent and unreliable for thick films (above $\sim 150\text{ nm}$) due to local variations in thickness across distances comparable to the spot size of the measurement system. This problem has been overcome in the experiments using multiple film deposition steps. In other words, a low film thickness has been deposited multiple times such that the stack of multi-layer films of the same material gives the desired high film thickness. This preserves the uniformity of the multi-layer stack to levels comparable with low film thicknesses, given that for each film, the non-dimensional spread time is low.

Using this concept of multiple deposition steps, film thicknesses as high as $\sim 500\text{ nm}$ have been demonstrated with excellent uniformity. Given that multiple deposition steps lead to slower throughput, no more than 3 steps were used for any given film thickness. The results are given in Figure 3.2 and pictures of the wafers have been shown in Figure 3.3. Except for sample 4 with target mean of 25 nm , all other samples were within the target of 2% relative non-uniformity. Table 3.1 illustrates the fact that a high degree of uniformity can be obtained by using thin superstrates. This uniformity is preserved at very high film thicknesses by using multiple film deposition steps. A trend to note, however, is that the relative non-uniformity % is higher for smaller mean film thicknesses. This can be attributed to the adhesion layer (AL) deposition that is required prior to the deposition of the curable monomer film. The adhesion layer is deposited using a vapor-phase vacuum process with a target of close to 2 nm . As can be seen, there

is significant non-uniformity in the film thickness of only the adhesion layer. At smaller film thicknesses, this variability is not masked as well as it is at higher film thicknesses.

Table 3.1: Experimental data with the thin 250 micron cored superstrate

Target mean	0nm	25nm	70nm	78nm	139nm	139nm	417nm
Samples	10	5	5	5	5	5	5
TFD steps	0	1 x 25nm	1 x 70nm	2 x 39nm	1 x 139nm	2 x 70nm	3 x 139nm
Obtained mean	1.88 +/- 0.4	26.36 +/- 0.74	71.55 +/- 0.73	77.04 +/- 1.46	146.3 +/- 1.63	142.7 +/- 1.1	434.6 +/- 3.84
Obtained std. dev.	0.25 +/- 0.11	0.51 +/- 0.11	1.11 +/- 0.17	1.09 +/- 0.21	1.54 +/- 0.13	1.35 +/- 0.13	3.45 +/- 0.48
Non-uniformity %	13.0 +/- 4.06	1.93 +/- 0.4	1.55 +/- 0.25	1.41 +/- 0.3	1.05 +/- 0.09	0.94 +/- 0.09	0.79 +/- 0.11

It must be noted that determining the propagation of this non-uniformity from the adhesion layer to the deposited film is not feasible. It requires measuring the adhesion layer thickness prior to depositing the desired film and then measuring the deposited film thickness at the same sites. This process can introduce particles on the wafer prior to the desired film deposition, which can compromise the quality of the desired film as well as cause damage to the superstrate. Moreover, given the resolution of the wafer loading clamp as well as the motion stage on the metrology setup, it is impossible to precisely locate the same measurement sites after the wafer has been unloaded and reloaded. Techniques such as scribing are not desirable for location of a reference because of their propensity to introduce particles which are a source of defects.

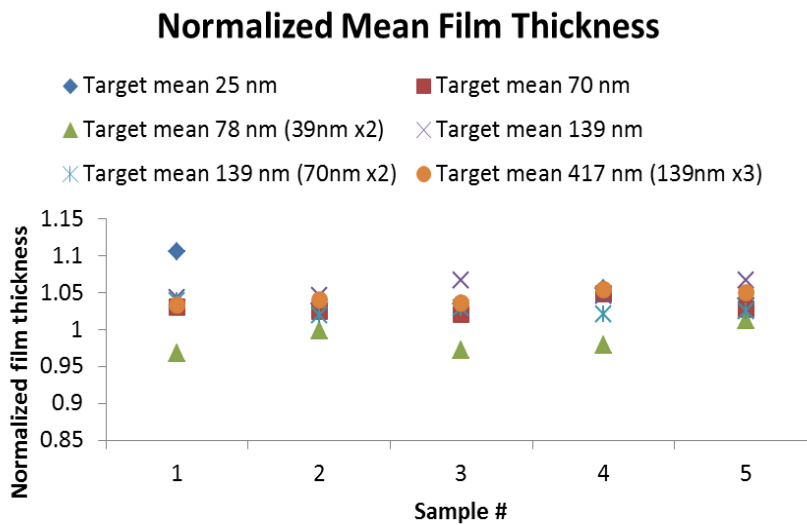
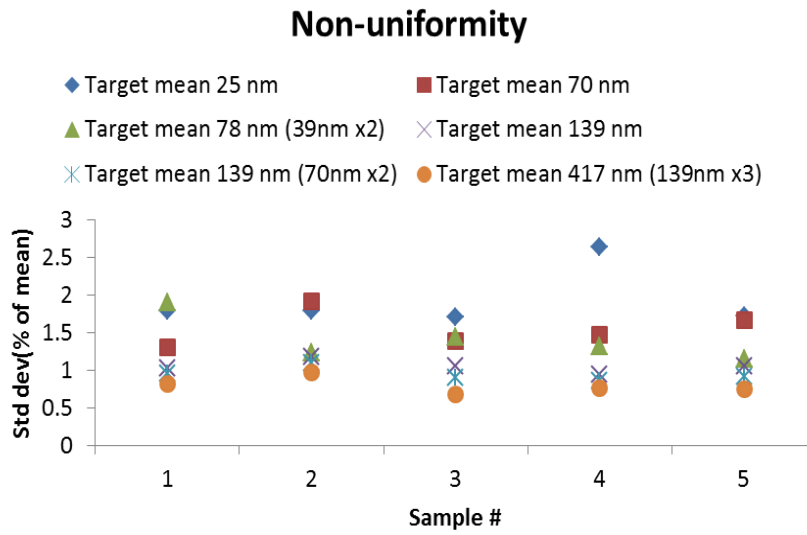


Figure 3.2: Plot showing the experimentally obtained mean film thickness and non-uniformity on 5 wafers with a 250 micron cored superstrate. The obtained mean film thickness has been normalized against the targeted value given in the legend for each case. As seen, its value is close to 1, which is what is expected. The standard deviation has been normalized against the obtained mean film thickness for each case to yield the non-uniformity. Except for sample 4 for a targeted mean of 25 nm, all other cases are below the desired 2% value.

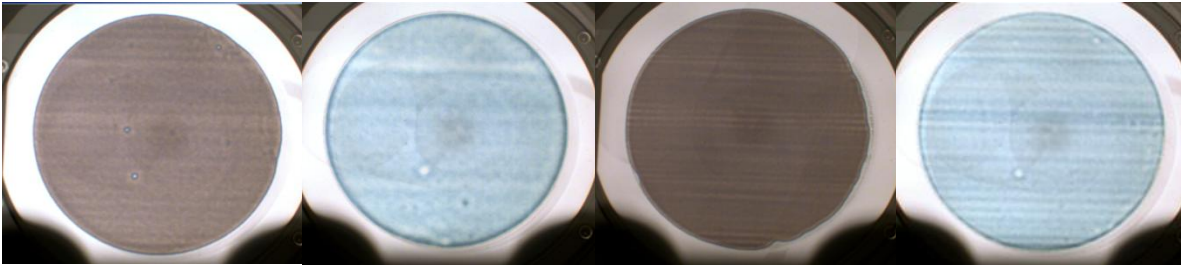


Figure 3.3: Uniform films deposited using the thin 250 micron cored superstrate. (L to R): 70nm, 139nm (all using a single deposition step) and 78nm and 139 nm using two deposition steps. The horizontal lines observed are artifacts of nozzle to nozzle variability in the multi-jet dispenser

3.3. UNIFORM FILMS WITH HIGH VOLUME DROPS

The previous section demonstrated J-CAST for highly uniform films with less than 2% non-uniformity. However, the drop volumes used were $\sim 6\text{pl}$, and as was discussed previously, there is a need in the biomedical area for uniform films of $\sim 100\text{nm}$ thickness with large volume drops $> 15\text{pl}$. Hence, as a preliminary test to understand process behavior at large drop volumes spaced farther apart, the J-CAST process was used with the UV-curable monomer for different drop volumes exceeding 15pl and the appropriate drop pitch to achieve film thicknesses of $\sim 70\text{nm}$. Since the inkjet is capable of dispensing only in steps of 6pl , multiple drop dispense steps were conducted prior to the coercing action by the superstrate. This exercise has been conducted by first extending the baseline model to understand the inherent non-uniformity in the spreading process.

3.3.1. Model Premise

Although the baseline model has been developed to understand the mechanics after the drops have merged to form a contiguous “macroscopic” film, it has also been extended to potentially capture the “mesoscopic” process of individual drop spreading prior to merging. The goal of this modeling exercise is to understand if the source of the non-uniformity lies in the steps prior to the formation of the contiguous film.

Given the wetting nature of the fluid and its low contact angle on both substrates, the radius of a drop ($\sim 100 \text{ um}$) tends to be much larger than the height ($< 1 \text{ micron}$), validating the use of lubrication approximation to model thin film flow. Hence, the basic physics remain the same, i.e., thin film fluid flow confined by one rigid and one elastic substrate. The spreading of individual drops can be construed as the driving of contact lines by the wetting characteristics of the fluid as well as the coercing of the superstrate. It must be noted that the merging process cannot be captured by this model, as it violates the basic lubrication assumption of negligible pressure gradients in the thickness direction. For more details on contact line motion and merging, one can refer to the following references^{92,39}.

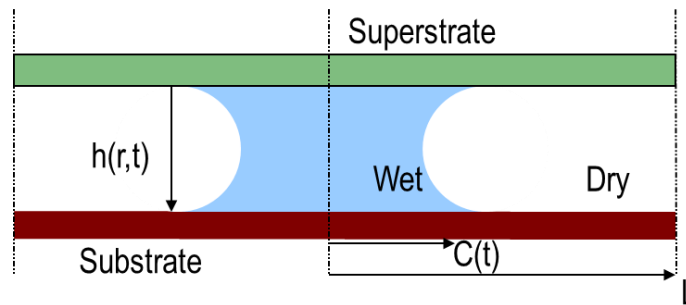


Figure 3.4: Geometry of the system under investigation for the mesoscopic model. A single drop of fluid is confined between the top elastic superstrate and the bottom rigid substrate.

3.3.2. Problem formulation

For the sake of preliminary investigation, the system is modeled in axisymmetric radial co-ordinates as a periodic array of droplets at a constant pitch of a wetting liquid (small contact angle on both substrates) upon which a top surface with an initial flat profile is imposed as shown in Figure 3.4. It is also assumed that the system is symmetric about the half-pitch of a given period containing a single droplet, to further simplify the modeling effort. Thus, with the given geometry, it is easy to see that a given spatial half

period consists of two regions, one containing the liquid (wet region 1) and the other without any fluid (dry region 2), with a meniscus or contact line at the boundary. The profile of the contact line has been assumed to be constant in keeping with the static contact angles of the fluid on the superstrate and substrate.

Along with the local film thickness $h(r, t)$, the position of the contact line, $C(t)$, also evolves with time under a constraint of volume conservation, assuming no evaporation. Region 1 (labeled as wet in Figure 3.4) is governed by the sixth-order unsteady evolution equation 2.4, while it is assumed that region 2 (labeled as dry in Figure 3.4) obtains a profile consistent with zero pressure in equations 2.5 and 2.6. Given the order of the governing equations, one initial condition for the film thickness, eight boundary conditions in h for thin plate bending (four each for the two regions) and two more in p for the coupled evolution equation are required to adequately constrain the system. Since the edges of the domain are effectively lines of symmetry, the odd derivatives are zero. This yields the following boundary conditions, similar to those discussed in Section 2.1.3:

$$\begin{aligned} @r = 0, \frac{\partial h_1}{\partial r} = \frac{\partial \nabla^2 h_1}{\partial r} = \frac{\partial p}{\partial r} = 0 \\ @r = R, \frac{\partial h_2}{\partial r} = \frac{\partial \nabla^2 h_2}{\partial r} = 0 \end{aligned} \quad \dots 3.1$$

The subscript on h denotes the region in which the boundary condition holds. The fifth derivative of h_1 is the same as the pressure gradient. Since there is no fluid at $r = R$, a similar condition does not exist for the right symmetry edge. This takes care of five boundary conditions. The remaining five are obtained by conditions at the meniscus, i.e., $r = C$ in Figure 3.4. Four of these reflect continuity in the film thickness, slope (first derivative), bending moment (second derivative) and shear force (third derivative) at the contact line going from region 1 to region 2 as follows:

$$@r = C(t), h_1 = h_2, \frac{\partial h_1}{\partial r} = \frac{\partial h_2}{\partial r}, \nabla^2 h_1 = \nabla^2 h_2, \frac{\partial \nabla^2 h_1}{\partial r} = \frac{\partial \nabla^2 h_2}{\partial r} \quad \dots 3.2$$

The last condition is obtained from the Young-Laplace equation which relates the pressure differential across a meniscus to the curvature and surface energy, γ , of the interface. With a wetting liquid on both the substrate and the superstrate, this yields the following nonlinear condition:

$$@r = C(t), p = -\gamma f(\phi)/h_1 \quad \dots 3.3$$

Since region 2 is not acted upon by any pressure, the profile of the superstrate in region 2 is given by the following equation:

$$\nabla^4 h_2 = 0 \quad \dots 3.4$$

For axisymmetric geometry, this homogeneous equation 2.18 yields a solution of the form:

$$h_2 = b_0 + b_1 r^2 + b_2 \log(r) + b_3 r^2 \log(r) \quad \dots 3.5$$

For region 1, the formulation of the thickness profile at any given instant of time is more complicated as the pressure field is unknown. Now, it can be observed that with a constant pressure field in region 1, the thickness profile would essentially be given as:

$$h_1 = a_0 + a_1 r^2 + a_2 \log(r) + a_3 r^2 \log(r) + \frac{p_0 r^4}{64D} \quad \dots 3.6$$

Thus, it is fair to assume that the thickness is then given by the above equation, but superposed by an additional unknown function that represents the variation in the film thickness caused by a spatially varying pressure field. This unknown function is expressed as an eigenfunction expansion with Bessel functions. The series expansion is truncated to a maximum of N terms. The exact form of the eigenvalues of the series solution is not known yet. Hence, this yields the following form of the solution for h_1 :

$$h_1 = a_0 + a_1 r^2 + a_2 \log(r) + a_3 r^2 \log(r) + \frac{p_0 r^4}{64D} + \sum_{n=1}^N H_n(t) J_0(k_n r) \quad \dots 3.7$$

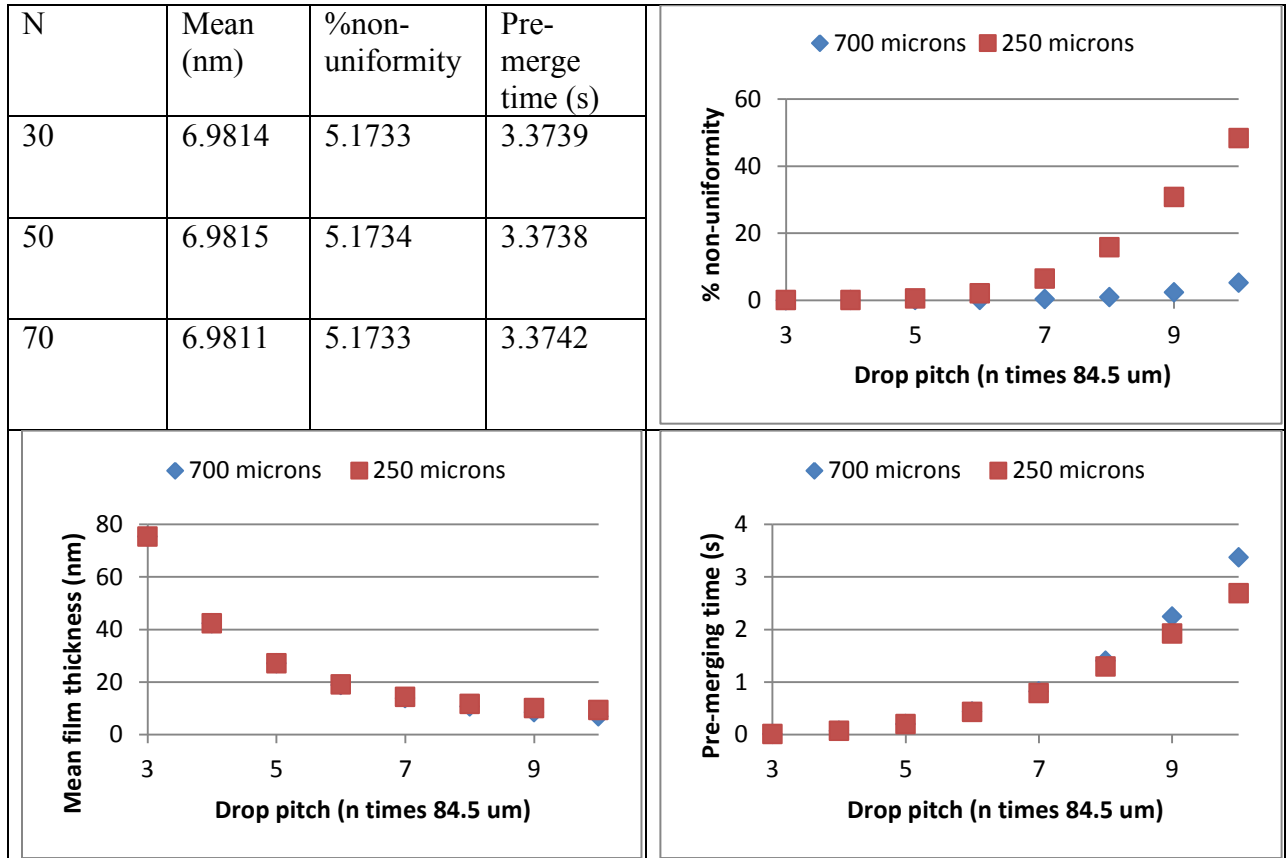
3.3.3. Solution and Results

The equations are then solved for an initial condition of a zero pressure flat superstrate profile. Similar to the procedure described in Section 2.1.3. This approach helps reduce the time evolution PDE into a system of ODEs in time, that have been solved using the ode15s solver in MATLAB, which is a 1st order explicit Runge-Kutta solver with variable time-stepping optimized for stiff systems. The simulation is stopped when $C = R$, i.e., when two neighboring drops are close to merging, or when the film thickness becomes 0, i.e., the superstrate comes in contact with the substrate, which is a singularity for thin film evolution. At every instance of time, strict volume conservation is also enforced, which gives the instantaneous value of the contact line position, or C .

Simulations were conducted by assuming the drop volume used in actual experiments, i.e., 6pl and drop pitch or R , corresponding to multiples of the nozzle pitch on the inkjet which is 84.5 μm . The initial spread is calculated by assuming that the dispensed drop takes on the shape of a spherical cap with an approximate contact angle of 9 degrees on the substrate and 25 degrees on the substrate. The influence of parametric variation in superstrate thickness along with drop pitch is studied through numerical simulation of the system. Since this system actually involves nonlinear boundary conditions, code verification was undertaken by increasing the no. of terms in the series expansion and checking for convergence. Results have been indicated in Table 3.2 below.

The key output metrics include: (i) mean film thickness, (ii) % non-uniformity or the ratio of standard deviation with mean film thickness, and (iii) time taken for neighboring drops to merge. While the mean film thickness and standard deviation help in understanding the inherent non-uniformity post-spreading and pre-merging, the time taken for the drops to merge (pre-merging time) helps in understanding the minimum time that a drop takes to merge with its neighbor after initial superstrate contact.

Table 3.2: (Top Left) Convergence analysis with increasing terms in the expansion for the case of 10x drop pitch and 700 micron superstrate; plots of %non-uniformity (Top Right), mean film thickness (Bottom Left) and pre-merging time (Bottom Right) with thick and thin superstrates with varying drop pitch.



The results indicate that the series does converge as there is little change in the numerical values with increasing terms. Also, from the plots in Table 3.2, drops spaced farther apart result in thinner films and take longer to merge, which is expected for both superstrates. However, the % non-uniformity is substantially different for thin and thick superstrates at sub-20nm films. The thin superstrate results in higher non-uniformity. This can be attributed to the fact that the work done to bend a thin superstrate is less than the same for a thick superstrate. With reducing film thickness, the capillary pressure is also increased, which is responsible for bending the superstrates. Hence, a significant

departure from the initial flat profile is seen as mean film thickness and superstrate thickness is reduced.

3.3.4. Qualitative Experimental Validation

Qualitative validation of the predictions of the mesoscopic model has been conducted through simple drop spreading experiments. Drop patterns of different pitch and volume were dispensed to obtain a mean film thickness of $\sim 70\text{nm}$. The spread time was kept close to zero and the contiguous fluid film formed after merging of the drops was immediately flood exposed. Metrology was conducted as described in Section 2.2.2. The experimentally obtained non-uniformity has been compared against the mesoscopic model prediction in Figure 3.5. As can be seen, the trend of increasing non-uniformity with increasing drop pitch is reflected in both the model and experiment. Thus, it can be said that the model qualitatively agrees with the experimental data.

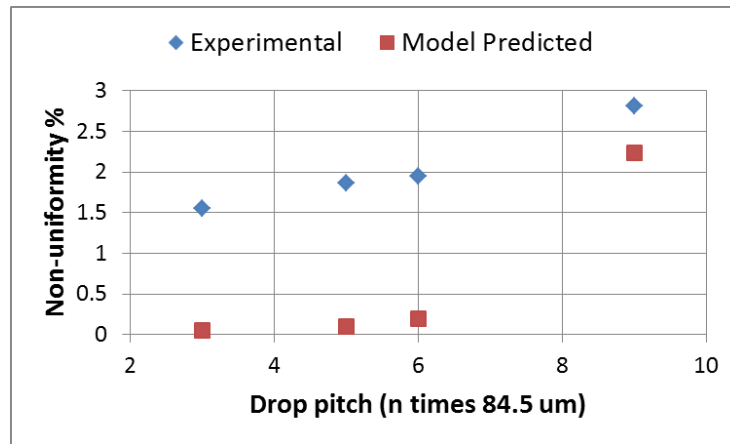


Figure 3.5: Comparison of experimental result and model prediction for drops of different volume and pitch for achieving a similar mean film thickness.

3.4. SUMMARY

In this chapter, the recommendations of the baseline model have been used to reduce the process time scale by thinning the superstrate to 250 μm . This helps achieve substantially more uniform films by slowing the influence of parasitic topography. Moreover, the baseline model has been extended to study the process of drop spreading. This has been used to analyze any non-uniformity encountered prior to the formation of the contiguous film. The model has also been experimentally validated to reveal decreasing uniformity with increasing drop pitch for the same target film thickness.

Chapter 4: Inverse Model and Validation for Varying Thickness Films

Unlike processes like spin-coating, inkjet-based deposition processes allow for spatial variations in thickness by controlling the volume and location of the dispensed drops. This has been exploited in the J-CAST process to obtain spatially prescribed nanoscale thin film profiles. The adaptive nature of the process has been enabled by validating an inverse model that can prescribe the location and volume of the dispensed drops to obtain a desired film thickness variation. This chapter details the work done in developing and validating the inverse model.

4.1. PRELIMINARY EXPERIMENTS

From deposition of uniform films, it was seen that drops of equal volume and spaced equally apart led to films with substantially lower non-uniformity with the thin substrate. However, it can be understood that changing the volume or spacing between drops at specific locations can lead to local variations in thickness. The purpose of the preliminary experiments was to observe the effect of having such local transitions in drop volume or pitch on the film thickness profile. Given that the baseline model in Section 2.3 was validated for nominally uniform films, it is also important to establish a basic validated process for non-uniform films. For the sake of simplicity, the transitions have been arranged such that the film thickness profiles vary concentrically in an axisymmetric co-ordinate system.

4.1.1. Metrology

Films with desired variation from uniformity have also been measured on the Metrosol deep UV film thickness metrology tool. The measurements were conducted at a pitch of 0.1mm, in both the normal to flat and parallel to flat directions seen in Figure

2.8. Unless otherwise depicted, the measurements in both directions have been averaged to give a mean profile across the radial direction.

4.1.2. Stepped Profile

The idea of the same drop pitch for uniform films across an area as large as 60mm diameter, has been extended to obtain a stepped film thickness profile. It was hypothesized that having multiple regions within the same 60mm diameter with each region having its own target uniform film thickness, would need different drop pitches across the different regions, but the same drop pitch within any given region. To this end, 4 concentric bands were sought, such that the nominal film thicknesses are 25nm, 75nm, 25nm* and 75nm† respectively and the transitions occur at diameters of 15mm, 30mm and 45mm.

The experiment was conducted on a 3” Si substrate with the thin 250um superstrate. As revealed by film thickness metrology, the mean film thickness across each concentric ring was as expected. However, the transition from one film thickness to the other, i.e., across concentric regions where the drop pitch was different, saw the occurrence of ripple like artefacts. These ripples corrupt the desired stepped profile. Hence, it is important to verify if these ripples were random experimental perturbations or had a physical basis as explained by the thin film evolution model given by equation 2.4. With an initial condition of a profile resembling a perfect square wave given by the desired variation and the corresponding locations of the drops with different pitch, the nonlinear baseline model was used to predict the final film thickness profile after the finite spread time used in the experiment. As can be seen from Figure 4.1, there is very

* A 25nm film can be obtained using 6pl drops with a pitch of 422.5um.

† A 75nm film can be obtained using 6pl drops with a pitch of 253.5um.

good agreement between the model prediction and the experimental data, confirming that the ripples stem from the physical process. This also solidifies the applicability of the forward thin film evolution model for situations involving nominally non-uniform films.

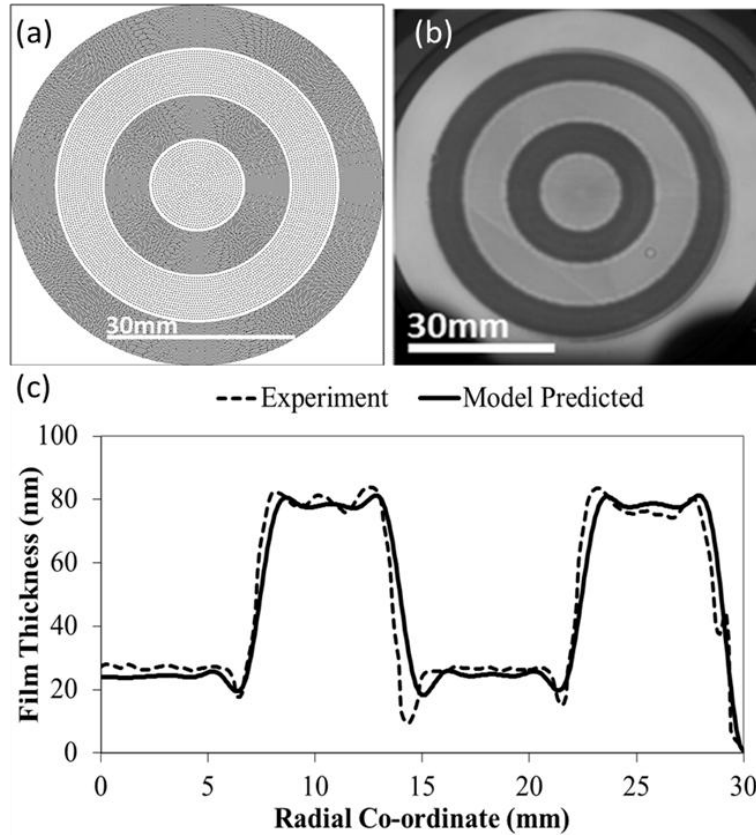


Figure 4.1: (a) The drop pattern with equal drop volume but unequal drop spacing for concentric rings of target mean 25nm (light) and 75nm (dark) thickness, (b) Picture of experimentally obtained film thickness, (c) Plot of the radial film thickness profile. The film thickness profile is affected by ripples due to the transient coupling between non-uniform drop pitch that can be predicted accurately using the thin film evolution model.

4.1.3. Continuously Varying Profile

Given that the ripples stem from the time evolution of film thickness transitions, a combination of such transitions was sought such that the final film thickness profile shows a continuous monotonic gradient. This exercise was done experimentally without

any insight from the model into the nature of the transitions required to get the desired gradient. The experimental result is given in Figure 4.2. Even when this film was allowed to evolve for a longer time such that the ripples have greater chance of being dissipated away, they are still observed, as shown in Figure 4.2. These ripples are spread across mm-sized areas. Given that these artefacts are a result of the fluid spreading and film evolution process, it should be possible to determine if they can be captured to get the desired film thickness profile. Essentially, the ripples are tantamount to a non-equilibrium state of the superstrate-fluid-substrate sandwich, the dynamics of which must be exploited to get the desired film thickness profile. This forms the motivation of the inverse model discussed in the next section.

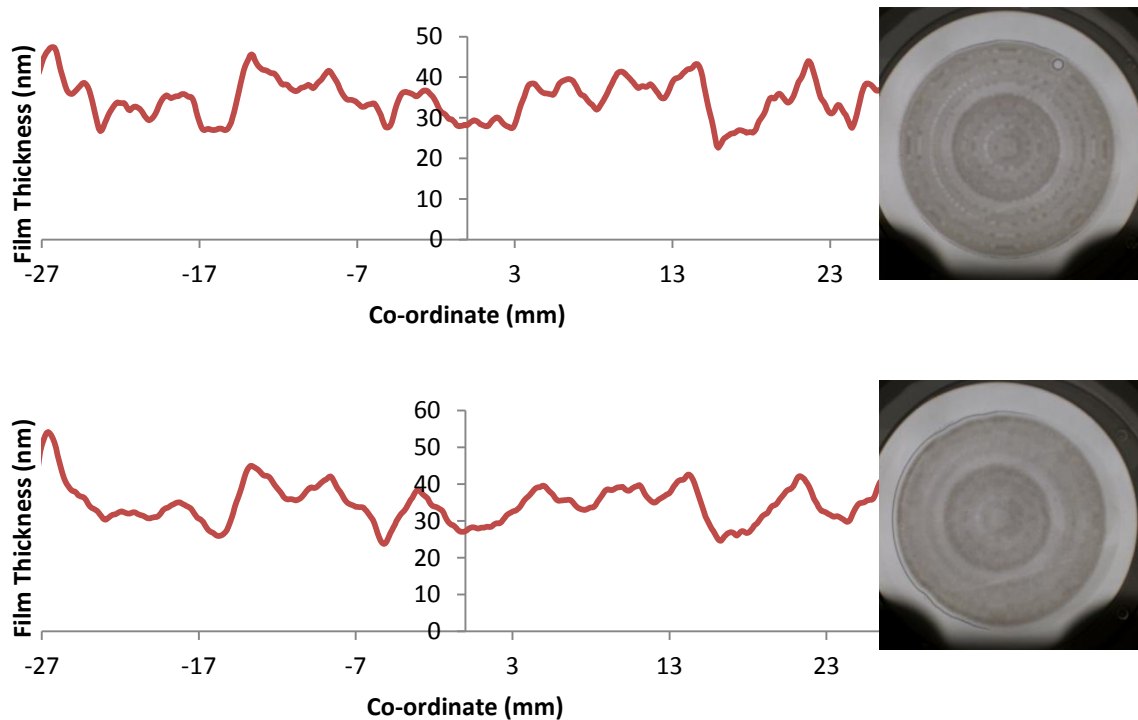


Figure 4.2: Illustration of using multiple drop patterns to get a desired graded film. The ripples are more pronounced with short spread time (top) and dissipate out at longer spread time (bottom).

4.2. INVERSE MODEL

The superstrate-fluid-substrate sandwich displays rich dynamical behavior that can be predicted using the forward model of equation 2.4, given an initial condition. However, given the dissipative nature and homogeneous boundary conditions for the system, the equilibrium state $t \sim \infty$ is always the same for any given initial condition. This equilibrium state is realized by the superstrate achieving a zero-deformation state with the fluid film thickness profile given by $h(x, \infty) = h_0 - w_s(x) + w_c(x)$, where h_0 is the mean film thickness. As can be seen, both superstrate and substrate topography determine the equilibrium film thickness profile.

For deposition of uniform films in Section 3.1, the need to move towards smaller non-dimensional spread times was asserted to minimize the influence of parasitic topography. For deposition of films with prescribed spatial variation, it is also desired for the system to be far removed from equilibrium, as equilibrium can only yield a single possible solution, which again is influenced only by the substrate and superstrate topography. Hence, with prescribed spatial variation of film thickness, the problem becomes one of finding the desired non-equilibrium transient such that the prescribed spatial profile is met. The use of thin superstrates, like the 250um cored superstrate, assists in lengthening the process window, such that there is greater room in the physical domain to capture the desired transient. This forms the basis of the inverse model type formulation which forms the core of this work on non-uniform films.

4.2.1. Problem Formulation

The inverse model formulation has several important aspects that culminate into obtaining the desired non-equilibrium transient. Achieving this desired non-equilibrium state first requires determining an optimum initial condition for the system and then, an optimum time to which this initial condition is evolved. Hence, the kernel of the

formulation is given by the validated forward model of equation 2.4, which gives the final profile given an initial condition. However, the initial condition of the system, itself, is a result of the spreading and merging of thousands of drops*. Prescribing the initial condition is, thus, tantamount to prescribing the volume and x and y location of each of these thousands of drops. Along with inkjet drop related parameters, the optimum time to which the system needs to be evolved also forms an output of the model. The primary inputs include the time-scale of the process, given by equation 2.23 and the associated system parameters, and any topography information. Figure 4.3 illustrates the flow of the inverse model formulation. Hence, overall, the inverse model can be setup as an optimization routine with the objective function given as a minimization of the error norm as follows:

$$f = \min \|h_d(r) - h(r, t)\|, \text{ where } h_d \text{ is the desired film thickness}$$

4.2.2. Constraints

The objective function is subject to several constraints stemming from the system hardware, as well as assumptions related to modeling of the process. The primary constraints are manifested in the discrete nature of the inkjet drop parameters, i.e., drop volume and location. The installed inkjet is capable of dispensing drops in integer multiples of 6pl, with a minimum of 6pl and a maximum of 42pl. At the same time, the locations of each drop are also discrete in nature, and have to be an integer multiple of the spacing or pitch between consecutive nozzles of the multi-jet dispenser. This value is 84.5 μm for the current inkjet. Given that the volume and x and y locations of each drop are desired outputs from the inverse model and that there are several thousand drops

* A uniform film with a target of 75nm thickness requires the dispensing of approximately 44,000 drops, each with volume of 6pl.

involved for a typical film thickness deposition, the number of these integer constraints is incredibly large. This drastically increases the complexity of the optimization and renders the problem highly nonlinear. Even though the objective function is a standard minimization of error norm, an analytical solution is not tractable because of the presence of these integer constraints.

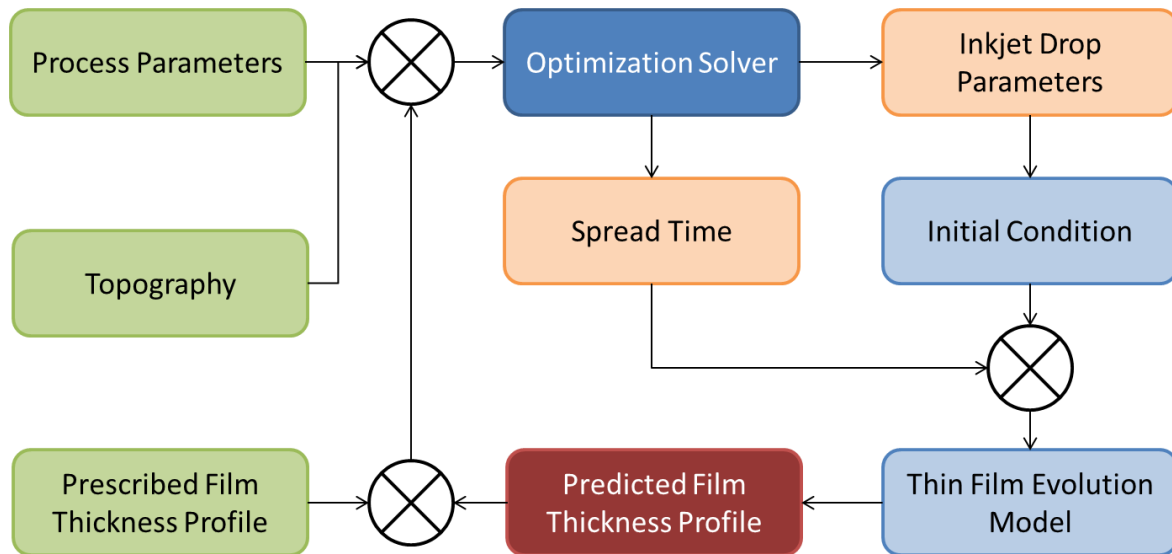


Figure 4.3: Schematic illustrating the inverse model formulation

The presence of at least one drop at the center of the substrate, where the superstrate first makes contact, is also set as a constraint on the solver. This constraint is important from a process control perspective and is not related to physical hardware. The absence of a drop at the center can result in hard contact of the substrate by the superstrate. This is undesirable as it may contaminate the superstrate. In addition, there are two inequality constraints that are also imposed on the optimization solver. They relate to the minimum film thickness seen for the initial condition as well as the final film thickness profile. Obviously, this minimum film thickness has to be greater than 0, and has been set as 2nm for the model to avoid hitting the absolute lower limit of 0.

4.2.3. Initial Condition

Given that the output of the inverse model is related to drop dispense parameters and not the initial film thickness profile, it is important to have an accurate prediction of the profile of the contiguous film formed immediately after merging of the drops. This is a critical element of the inverse model formulation. It dictates the fidelity of the forward model kernel, as an improper initial condition will lead to an improper final film thickness profile. However, the drop spreading and merging processes have not been explicitly captured in the forward model of equation 2.4, which basically predicts the evolution of the superstrate-fluid-substrate sandwich after formation of the contiguous fluid film. Hence, this step has been captured by way of a modeling approximation supported by experimental calibration.

The presence of a drop at a given location increases the local film thickness. This local film thickness profile has been approximated as an error function type variation supported by an effective drop volume. The effective drop volume captures parasitic losses given by phenomena such as evaporation, clogging of the nozzles and volume shrinkage of the film after UV curing and superstrate separation. This decreases the effective drop volume to a value lower than the dispensed volume. Calibration of this effective drop volume is critical, since it captures systematic and random perturbations. In a typical run, the effective volume for a 6pl is usually modeled as 4pl. The error function profile is imposed from neighboring drops, with a peak at the given drop location, $r = \rho$. It is essentially a smooth, continuous and differentiable approximation to the otherwise non-differentiable step function. A convolution of these error function type variations along the entire deposition area gives the desired initial condition, $h(r,0)$. The details for a representative case in axisymmetric co-ordinates have been given below in equations 4.1-4.3.

$$h_{\rho}(r, 0) = h^* \left[1 + 0.5 \operatorname{erf} \left(\frac{1}{k} \left[-r + \rho + \frac{np}{2} \right] \right) \right] \left[1 + 0.5 \operatorname{erf} \left(\frac{1}{k} \left[r - \rho + \frac{np}{2} \right] \right) \right] \quad \dots 4.1$$

$$h^* = \frac{V^*}{\pi \left(\rho + \frac{np}{2} \right)^2 - \pi \left(\rho - \frac{np}{2} \right)^2} \quad \dots 4.2$$

$$h(r, 0) = \sum_{\rho} h_{\rho}(r, 0) \quad \dots 4.3$$

where p is the nozzle pitch of 84.5 μm , n is the integer multiple of the nozzle pitch at which the drops are spaced, V^* is the effective drop volume and k is a characteristic length scale for the error function variation. This characteristic length scale gives a measure of the local slope in the initial film thickness profile. This slope is also dependent on the merging properties of the drops. For example, if the drops spread and merge rapidly, the slope is steeper, leading to a smaller value of this characteristic length scale. If, however, the spreading is more relaxed, this length scale is larger. Overall, it is experimentally calibrated as $\sim 0.5\text{mm}$ for axisymmetric co-ordinates.

A representative example of an approximated initial condition is given in Figure 4.4, where a transition from a film thickness of 75nm to 25nm is sought for one-dimensional Cartesian co-ordinates at $x = 2\text{mm}$ by changing the pitch of 4pl effective volume drops from 253.5 μm to 422.5 μm . The step function profile shows the film thickness variation if only the average film thickness obtained from the particular drop pitch at the given location is modeled. The error function profile depicts the modeled initial condition for the given drop pattern transitions and is a more accurate representation of the actual scenario.

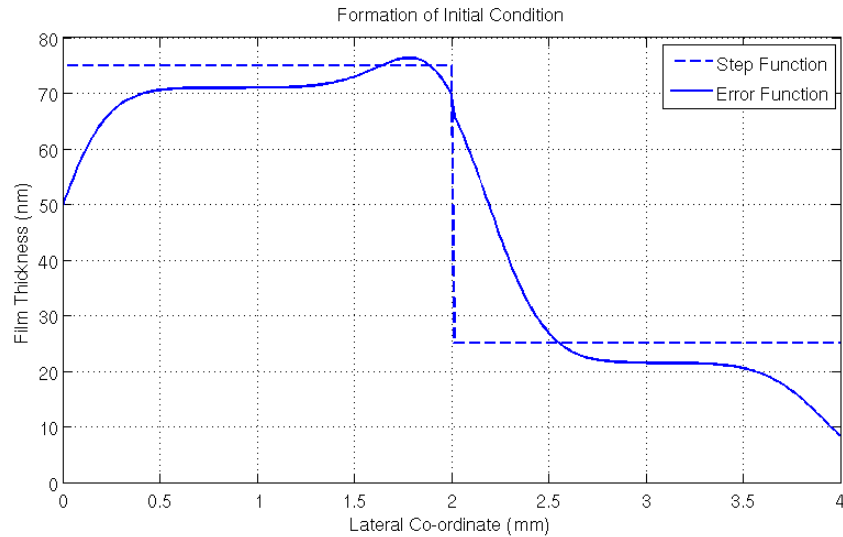


Figure 4.4: Example of a modeled initial film thickness profile formed after merging of drops spaced at varying pitch.

4.2.4. Optimization Solver

The large number of desired outputs coupled with nonlinear integer constraints precludes the use of analytical solutions for the optimization problem. Moreover, given the complexity of the system and the large parameter space, it is not possible to verify the existence of a global minimum. Hence, a stochastic approach to the optimization problem has been sought.

Genetic algorithms are a useful iterative search heuristic for solving highly nonlinear minimization problems such as the one at hand. They mimic the process of biological evolution and are based on the principle of “survival of the fittest”. A typical genetic algorithm requires the specification of a parent population of possible solutions. This initial population must satisfy the constraints set for the problem. At each successive iteration or generation, the algorithm repeatedly modifies the population of individual solutions. The algorithm randomly selects individuals from the current population as “parents”, with a bias towards breeding of fitter individuals. The “genes” or parameter

values of two such parents are then used to determine the genes of their “child”. This passing of genetic traits is again based on a stochastic random process and involves what are called inheritance, mutation and crossover. The effect of the same is that the children population is typically fitter than the parent population. This procedure also allows the solution to overcome wells of local minima. Over successive generations, the population "evolves" toward an optimal solution until a maximum number of generations or maximum allowable computational cost is reached. Genetic algorithms differ from classical optimization solvers in that they have a population of possible solutions rather than a single solution at each iteration. Also, the solution at the next iteration is not deterministic, implying that even with the same initial population, two different runs of a genetic algorithm procedure can yield two different solutions after the same number of generations. The genetic algorithm toolbox, inbuilt in MATLAB R2010 has been used for the minimization routine.

4.2.5. Simplifying Approximations

Even with a stochastic solver, the number of desired outputs is substantially high. As explained earlier, >10,000 drops need to be dispensed for a typical film deposition step. Each drop has three unique identifiers, volume and x and y locations, leading to a desired output of in excess of 30,000 parameters. This adds to substantial computational expense with added losses in performance fidelity due to the possible presence of several minima. Hence, to simplify the optimization process, the drop volume is held fixed at 6pl. In theory, a drop volume in multiples of 6pl can be achieved by dispensing a 6pl drop as many times. Dispensing multiples of the same drop volume leads to more consistent jetting than dispensing the specified volume at once. This allows reliable calibration for

the inverse model formulation to work. However, even after fixing the drop volume, there are still in excess of 20,000 desired output parameters.

Further simplification of the problem is achieved by coarse-graining of the drop pattern. This is done by first setting a desired number of sub-regions within the substrate area and then constraining the drops in each sub-region to have the same pitch or integer multiple of the nozzle pitch. This drop pitch is allowed to vary across different sub-regions, thus allowing for the desired film thickness variation to be achieved. Only the number of sub-regions is held fixed, while the solver has the freedom to choose where to place different sub-regions on the substrate. The sub-regions are also allowed to overlap with each other. This implies that the film thickness at a given location can result from a convolution of several different drop pitches. The nature of the sub-region varies with the co-ordinate system: for axisymmetric systems, each sub-region is in the form of an annular ring while for Cartesian co-ordinates, each sub-region is a rectangle. This coarse-graining allows for the number of output parameters to be drastically reduced, but also compromises with control over short-range film thickness profiles. The number of sub-regions is determined by the order of the spatial wavelength of the desired film thickness variation.

For viable use of adaptive thin film deposition in a high-throughput manufacturing environment, the genetic algorithm routine needs to arrive at a solution in reasonably quick time relative to the desired throughput. Hence, it is necessary to keep the optimization routine as well as the kernel model simple. This has been done by keeping the genetic algorithm population size at 50 and building the optimization around the linearized forward model with no nanotopography, for which an analytical solution is available, similar to equations 2.16–2.18 with all topography amplitudes as 0. It has been shown previously in Section 2.3, that experimentally, this approximation does not cause

significant error in the model prediction (cf. Figure 2.20), if the spread time is kept within 20s for a 700um superstrate, which converts to ~250s for the 250um superstrate if all other parameters in the process time scale (equation 2.23) are kept the same.

However, the linearized forward model is strictly applicable only for nominally uniform films and may not hold for prescribed thickness variation. Hence, after a run of the genetic algorithm routine, the output was tested with a single numerical simulation of the full non-linear model, which is substantially more computationally expensive than the linearized model. The time evolution of the nonlinear model was conducted using a 1st-order implicit scheme. It was preferred over explicit Runge-Kutta time-stepping used in Section 2.3, as the latter led to solution instabilities due to the fine spatial grid (see Section 2.1.5). If the spatially integrated root-mean-square (RMS) error between the desired film thickness profile and that obtained by non-linear evolution exceeded a desired value, the inverse model was run again with the initial population of the next run seeded by the solution of the previous run. This procedure was continued till the desired tolerance or maximum number of allowable iterations was achieved. Each iteration of the inverse model typically takes approximately 15 minutes on a standard quad-core workstation.

4.3. EXPERIMENTAL VALIDATION

The inverse model formulation involves several constraints, assumptions and simplifications. Experimental validation of the same is imperative to understand if this formulation is viable for adaptive deposition of thin films.

4.3.1. Process Limits

The process limits are defined by the peak-valley range of film thicknesses that can be deposited and measured reliably. It was seen in Section 3.2 that uniform films

with thickness greater than $\sim 100\text{nm}$ suffer from an undesirable non-uniformity stemming from parasitics such as substrate topography. This non-uniformity can be even more pronounced given that the optimal spread times required for getting the desired film thickness profile given by the inverse model can be substantially high, approaching even 100-200 seconds. Moreover, it can also render the approximation of a linearized forward model without topography invalid. Hence, it was decided to keep the peak film thickness at any location on the substrate lower than 100nm. From a metrology standpoint, it was also desirable to not have peak-valley film thickness variation of greater than 75nm. Variation beyond 75nm can cause the measurements to be unreliable, thus necessitating multiple measurement iterations and thereby, introducing more sources of error.

4.3.2. Film Thickness Profiles for Validation

With all these limits in place, it was decided to validate the inverse model for the following six film thickness profiles, where $r \in [0, R]$ and $R = 30\text{mm}$:

i. $h_d = 50 + 25 \cos\left(\frac{10\pi r}{R}\right) \text{ nm}$

ii. $h_d = 50 + 25 \cos\left(\frac{10\pi r}{R} - \pi\right) \text{ nm}$

iii. $h_d = 50 + 25 \cos\left(\frac{14\pi r}{R}\right) \text{ nm}$

iv. $h_d = 50 + 25 \cos\left(\frac{20\pi r}{R}\right) \text{ nm}$

v. $h_d = 50 + 25J_0\left(25.09\frac{r}{R}\right) \text{ nm}$, where J_0 is a zeroth order Bessel function of the first kind, and

vi. $h_d = 10 + 5 \cos\left(\frac{10\pi r}{R}\right) \text{ nm}$

Validation of these profiles is a demonstration of the versatility of the process in terms of different spatial wavelengths and amplitudes of film thickness variation. For example, between cases (i) and (ii), there is a phase shift of 180 degrees. This will serve as a test of whether the process is capable of handling both, a peak and a valley at the center or point of initial contact. Similarly, among cases (i), (iii) and (iv), different spatial wavelengths of film thickness variation can be tested. Along the same lines, different amplitudes can be tested between cases (i) and (vi). Case (v) is a special case involving a Bessel function type variation, which allows for continuous variation of amplitude and wavelength in the same deposition area.

4.3.3. Convergence Analysis

Prior to performing experimental validation, it is important to check if the inverse optimization framework leads to a converged solution. To this end, the iterative inverse optimization was run for three similar sinusoidal film thickness variations, but with randomly generated amplitude and wavelength. A normalized error between the desired and the model predicted profile was tracked at the end of each iteration. This has been plotted in Figure 4.5 for each of the three profiles.

From Figure 4.5, it can be seen that the normalized error decreases progressively and converges to a local minimum. Given the complexity of the problem, it is not possible to ascertain if the converged value is a global minimum. The maximum number of iterations in the optimization framework can be safely set to 10, as it appears to be a conservative bound within which convergence is achieved. Depending upon the application, a tolerance for the normalized error can also be set for determining convergence.

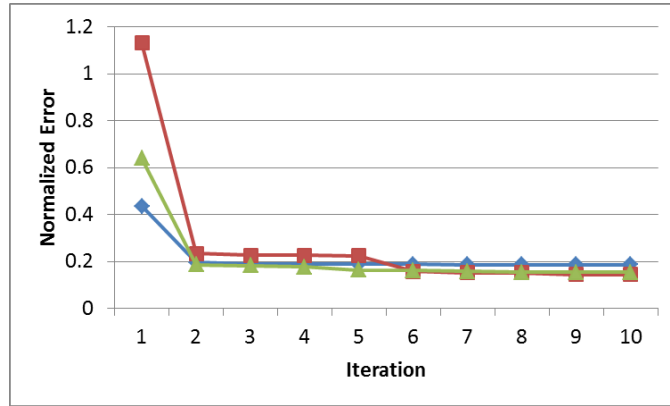


Figure 4.5: Plot showing the convergence of a normalized error in the optimization scheme for three randomly generated film thickness profiles.

4.3.4. Results

The results of the experimental validation for each of the six cases have been shown in Figure 4.6. Each plot compares the desired film thickness profile with the model predicted best profile and the experimentally obtained one. From the plots in Figure 4.6 and the data in Table 4.1, it can be seen that overall experimental data agrees quite well with the model prediction and the desired variation, especially matching the wavelength of the variation. There is a slight deviation in the film thickness close to the edges and the origin. The deviation at the edges is expected because of the zero flow boundary condition chosen in the model, whereas in practice, the boundary condition is a mix of interfacial pressure as well as loss in volume due to evaporation. Some sample pictures have been shown in Figure 4.7.

Table 4.1: Deviation of the experimental result from the model prediction as well as the prescribed variation

Case	1	2	3	4	5	6
RMS error b/w experiment & prescribed	5.1 nm	6.3 nm	10.1 nm	10.0 nm	5.6 nm	2.6 nm
RMS error b/w experiment & model	5.4 nm	6.2 nm	7.3 nm	8.1 nm	6.0 nm	2.2 nm

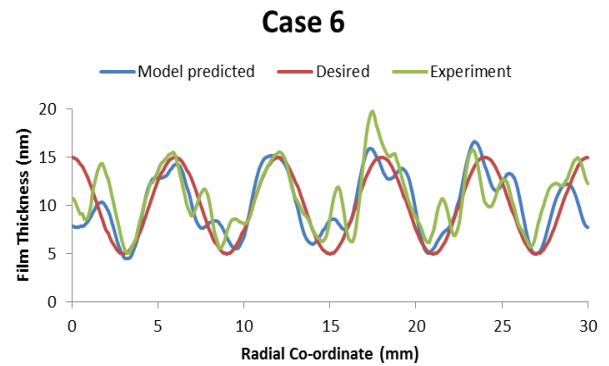
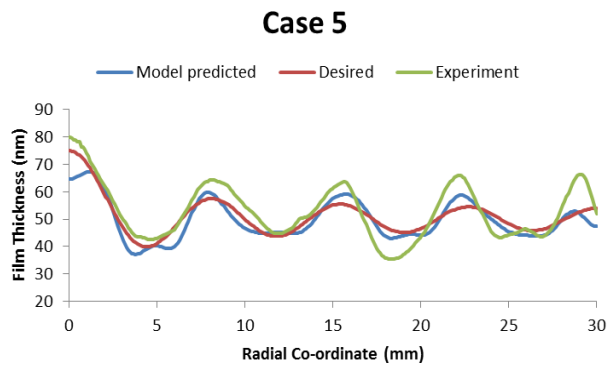
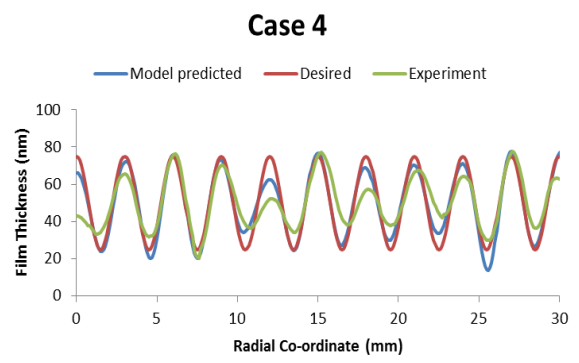
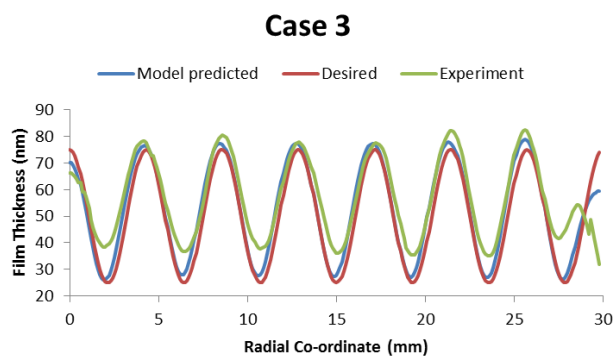
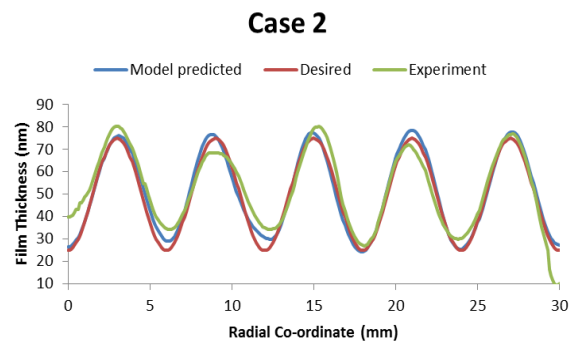
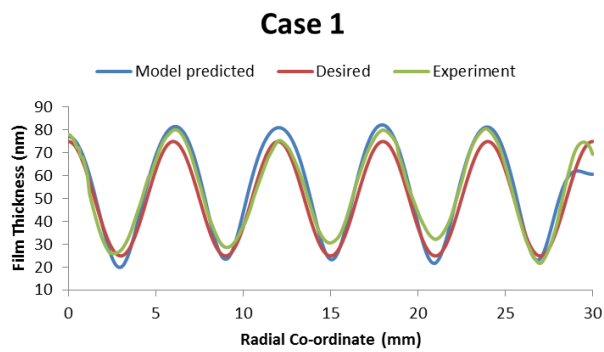


Figure 4.6: Inverse model validation test cases

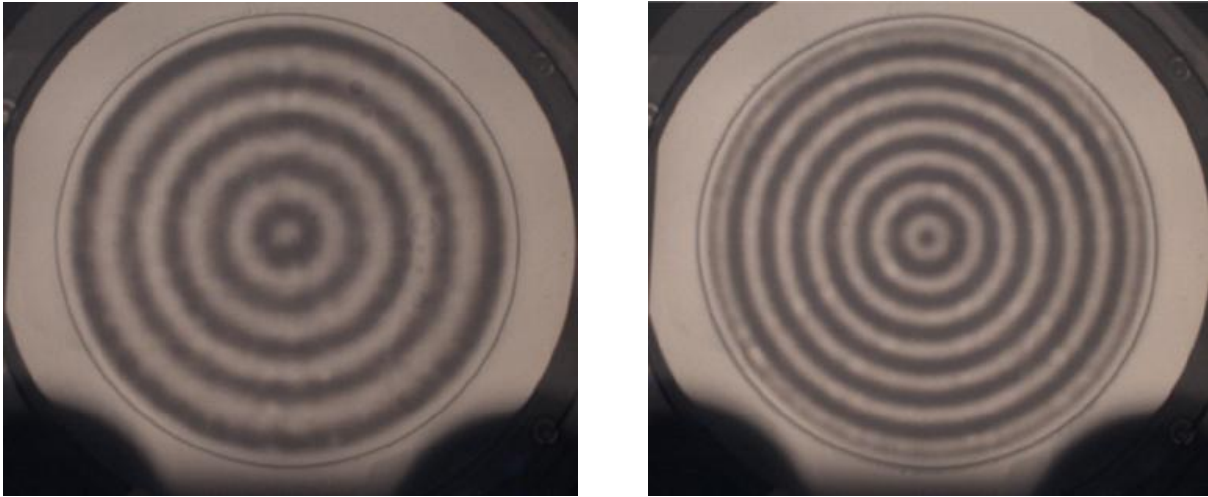


Figure 4.7: Pictures of the samples for case 2 (left) and case 3 (right). Higher film thickness corresponds to the darker region in the pictures. The concentric peaks and valleys are clearly visible.

While the model is indeed able to accurately predict the drop patterns required to at least achieve the same spatial trend with respect to the locations of the peaks and valleys, the actual nominal values at the peaks and valleys show some deviation. This is attributed to perturbations in the inkjet drop volume, which made case-case calibration of the drop volume quite elusive. This resulted in a systematic error, as observed at the valleys in case 3, but which is less prominent or negligible in case 2. Accurate calibration of the drop volume is imperative to obtain an accurate prediction from the inverse model. Hence, it became difficult to set global quantitative metrics for validation, even though qualitatively the experimental data exhibited the potential to match the model prediction.

In addition, for case 5, the error was attributed to the discrete nature of the drop volumes, preventing a continuous gradation in wavelength and amplitude, even as the spatial trends between the desired variation, model prediction and experimental result were matched. Case 6 was a special case with ultra-thin films. In this case, the model

itself was able to predict that the thickness profile would be in disagreement with the prescribed thickness profile, even for the spatial trends. The experimental result corroborated with this model prediction. Hence, this pointed to physical constraints in achieving the desired spatial variation in ultra-thin films. Thus, while the inverse model was validated against experiments for most cases in the bulk of the deposited area, it failed for the ultra-thin film case. To test the hypothesis of a physical constraint for the ultra-thin film case, the inverse model was used to generate desired drop patterns after relaxing one or more constraints during optimization.

4.4. PERFORMANCE PREDICTION

The inverse model validation process reveals that the experimental data matches well with the model prediction for most of the test cases. It was also seen that with continuous variation in amplitude and frequency, as exhibited by the Bessel function in case 5 the model prediction can be off the desired film thickness profile. The same is observed for the ultra-thin film in case 6. This can be attributed to the fact that the installed inkjet can only discrete drop volumes in steps of 6 pl, making minor changes to the film thickness profile difficult. Theoretically, if the inkjet was capable of dispensing drops at finer resolution, say, 1 pl, it might be possible to get better agreement between the model prediction and the desired film thickness profile. Finer drop resolutions also mean that drops will be spaced closer together to get the same thickness profile, thereby leading to better uniformity. Hence, it has been hypothesized that with finer drop resolution at 1 pl, it is possible to obtain better agreement between the desired profile and the model prediction. This hypothesis has been tested with the inverse model for case 6 with the ultra-thin film. The obtained profile has been plotted in Figure 4.8. Even with a finer drop pitch, a mismatch is observed, primarily confined to the center and the edge,

and the overall RMS error is to the tune of $\sim 12\%$. This is better than the $\sim 20\%$ error seen for the actual case 6. Hence, with a finer inkjet, it is possible to obtain better agreement and the inverse model can serve as a handy tool for the same.

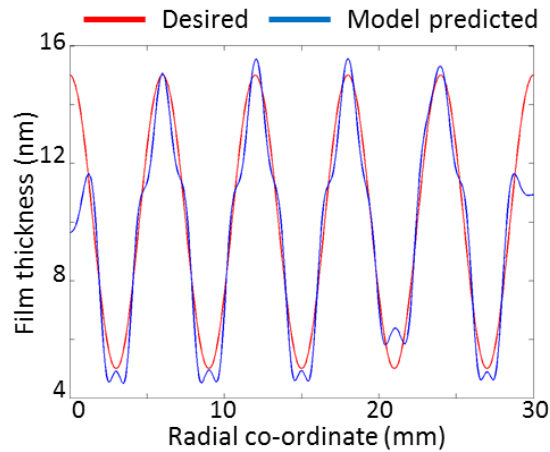


Figure 4.8: Hypothetical case of 1 pl drop volume giving much better agreement between the model prediction and desired profile for the ultra-thin film case 6.

4.5. SUMMARY

Following a discussion on uniform films in the previous chapters, this chapter introduces J-CAST for depositing films having prescribed variation in thickness with the help of an inverse optimization formulation. This is built around the validated thin film evolution model and is used to obtain optimum drop parameters and an appropriate spread time to capture the necessary transient that best approximates the desired profile. The optimization routine is subject to a number of integer constraints related to the physical system. Experimental validation of this inverse model has been done through a variety of non-monotonic thickness profiles. Limits of the process have also been identified, with the inverse model being used to predict the performance of the system with finer inkjet drop volumes.

Chapter 5: Applications of JCAST

Robust deposition of nanoscale films with prescribed variation of thickness can enable a variety of applications, not only in the area of film deposition²⁹ but also of freeform surface generation³². For the former, it is important to maintain the prescribed thickness, while for the latter; the aim is to achieve surfaces of desired profiles, irrespective of the thickness of the underlying film. Representative cases for both categories of applications have been demonstrated with the help of the inverse formulation of JCAST. However, to achieve the same, film thickness variations in Cartesian co-ordinates and not just in axisymmetric co-ordinates need to be enabled by JCAST. As opposed to radial drop pattern grids shown in the previous chapter, rectilinear or Cartesian grids, especially for intentionally non-uniform films, can have sub-optimal performance given that the preferential method of drop spreading and merging is through a radially moving front. Hence, in addition to enhancing modeling and simulation capabilities, the process recipes have also been optimized to ensure that experimentally, the process remains robust.

5.1. ONE-DIMENSIONAL J-CAST

Films with prescribed thickness variation in a single radial direction were demonstrated in the previous chapter. The knowhow gained in that exercise was extended to establish J-CAST for film thickness variations in a single rectilinear direction..

5.1.1. Inverse Model Enhancement

The inverse model formulation has been modified to incorporate the effect of using one-dimensional Cartesian geometry, while keeping the basic optimization solver, objective function and primary constraints the same as in the validation of axisymmetrically varying films. The deposition area is a square of side 50mm, centered

at the center of the wafer. The film thickness is prescribed to vary along the x co-ordinate, while remaining constant along any line parallel to the y -axis. After constraining the drop volume to be the same, this implies that the drop spacing is prescribed to vary only along the x co-ordinate. At any given x co-ordinate, the drop spacing in the y co-ordinate is constrained to be the same as that of the x co-ordinate. Thus, the coarse-graining algorithm in Section 4.2.2 is modified to incorporate sub-regions that are essentially rectangular strips extending along the full length of the y -axis. The beginning and ending x co-ordinates are outputs of the inverse model, similar to the inner and outer diameters for the annular sub-regions used in the axisymmetric formulation.

The capability of the optimization solver to handle one-dimensional Cartesian co-ordinates has been enhanced by modifying the eigenfunctions to be trigonometric, instead of the Bessel function type variations seen earlier. It must be noted that for axisymmetric co-ordinates, the desired variation extends from 0 to R , whereas for Cartesian co-ordinates, it extends from $-R$ to R , given that desired variation of film thickness may not be symmetric about the wafer center. With the grid step size being the same, this applies additional computational expense to the optimization solver as the number of eigenmodes is now increased two-fold. The boundary conditions for the simulations are symmetry at the two extremes, implying that the odd derivatives are zero, as given in Section 2.1.2. The characteristic length scale, k , for the formation of the initial condition is changed to ~ 400 μm , as the drop spreading characteristics are now different from the axisymmetric case. With this change, it is also necessary to constrain the minimum drop grid spacing to be 3 times the nozzle pitch. If the drop pitch is less than 3 times the nozzle pitch, it results in an over-estimation of the film thickness. This is because neighboring drops in grids of less than 3 times the nozzle pitch merge even before the application of the superstrate.

This changes the initial condition formation as the drops are no longer individually identifiable.

5.1.2. Metrology

Metrology is again conducted with the help of a deep UV film thickness measurement tool from Metrosol. The films are deposited such that they have prescribed variation along the direction normal to the wafer flat and constant thickness along any line parallel to the wafer flat. The metrology is conducted along 5 parallel lines in the direction normal to the wafer flat, such that each line captures the experimentally obtained film thickness variation and is spaced 10 mm away from the next line. There are 101 measurement points along each line with a 0.5mm distance between consecutive measurement locations. The experimentally obtained film thickness variation is the average of the data along the 5 measurement lines.

5.1.3. Gradient surfaces

Gradient surfaces for applications in materials research have been reviewed in Section 1.6.1. Although such surfaces can have a variety of graded surface properties, the variation of film thickness only is considered in this work. A representative gradient surface is chosen with a linear film thickness variation from ~25nm to ~100nm across a lateral distance of 50mm.

It must be noted that possible drop locations are discrete and not continuous. Therefore, obtaining a continuous monotonic grade from one end of the wafer to the next is non-trivial, as the model predicted profile is expected to show ripple-like variations, consistent with the discrete placement of drops. Moreover, in the absence of any topography, a linear film thickness profile introduces a situation similar to that of neutral equilibrium when using an implicit scheme to solve for the linearized governing equation

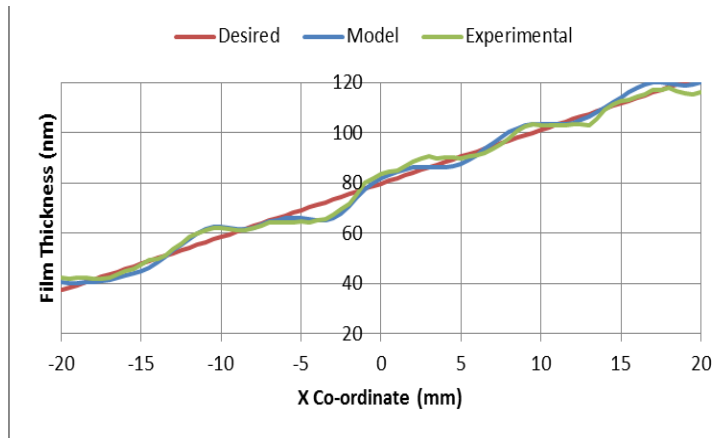
2.14. This is because the time derivative depends on the 5th and 6th order spatial derivative of the film thickness profile, which is zero for the desired linear variation. As can be seen, this forces the time derivative to also be zero. Given that the implicit solver numerically solves for nonlinear equations at a particular iteration, a time derivative approaching zero results in the lack of a well-defined gradient for the numerical solver to approach a solution. In reality, this situation does not exist because the presence of substrate or superstrate topography introduces a finite perturbation to the time derivative. Hence, to overcome this singularity, random substrate topography is introduced such that it is normally distributed about a zero mean and standard deviation of 1nm. This perturbation to the right-hand side of the equation 2.14 is sufficient to ward off the numerical problem, but introduces a potential source of error in the model predicted best fit. In order to best obtain the linear profile, a measurement of the substrate topography can be done to get a linear film thickness profile tailored for the given substrate. However, this has not been done for the purpose of this demonstration.

Given that gradient surfaces are typically required to simplify combinatorial experiments in materials science and research, it is important to verify if such surfaces can also be generated with large drop volumes. This is because functional fluids can tend to be more viscous and less amenable to inkjetting in small drops. To this end, the inverse model formulation has been used to generate drop locations with both 6pl drops and 30pl drops. The former is the nominal case, while the latter is used as a representative case for large drop volumes.

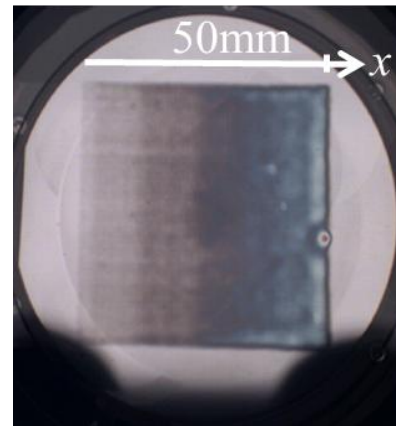
It must be noted that drops of volume equal to or higher than 30pl need to be spaced so far apart to achieve the desired film thickness values, that the merging characteristics can get altered. This prevents a direct comparison of the experimental result across the different drop volumes. The effective drop volumes are calibrated as

4.8pl and 28pl for both cases, respectively. The results, comparing the experimentally obtained data with the model prediction and desired profile have been shown in Figure 5.1. For the 30pl case, drop merging issues are visible at low thicknesses, in both the left side of the picture and the ripples close to the left end of the plot. Given that the sub-regions are allowed to overlap, the final film thickness, even for low values, is a convolution of drops being placed at different pitches. The maximum drop pitch output by the inverse model is 28 times the nozzle pitch or 2.366 mm. From the mesoscopic model introduced in Section 3.3, a single 30 pl drop spreading across this pitch can exhibit a substantial non-uniformity of 9.0nm standard deviation. As a comparison, the maximum drop pitch at a similar location for the 6pl drop is 14 times the nozzle pitch of 1.183mm, leading to a non-uniformity of 4.8nm standard deviation. This local non-uniformity is not as evident as the same for the 30pl case.

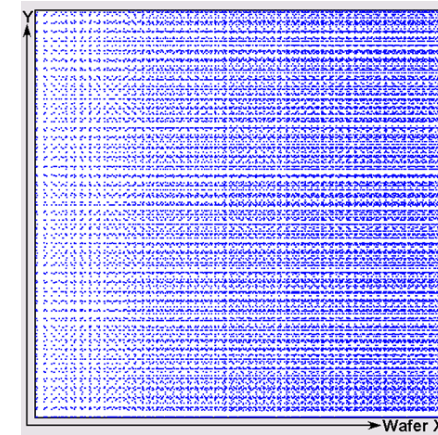
As can also be seen from the plots in Figure 5.1, there is very good agreement between the experimental result and the model predicted best profiles for both drop volumes. In essence, a linear gradient is approximated by the model prediction as a series of steps with increasing film thickness. However, the model predicted best profile matches the desired linear variation more closely for the smaller drop volume of 6pl than the larger drop volume of 30pl. This is expected as the drops are spaced farther apart to achieve a similar film thickness when their volume is higher. This increased spacing between consecutive drops causes the coarse-graining algorithm to select larger sub-regions with the same drop pitch, thereby, accentuating the steps more than in the case of the smaller sub-regions of 6pl drops. The presence of steps and the influence of coarse-graining are exemplified in Figure 5.2, where optimal drop pattern layouts with both 30pl and 6pl drops have been shown. It can be seen that with higher drop volume, the number of grains is reduced as the drop pitch is increased.



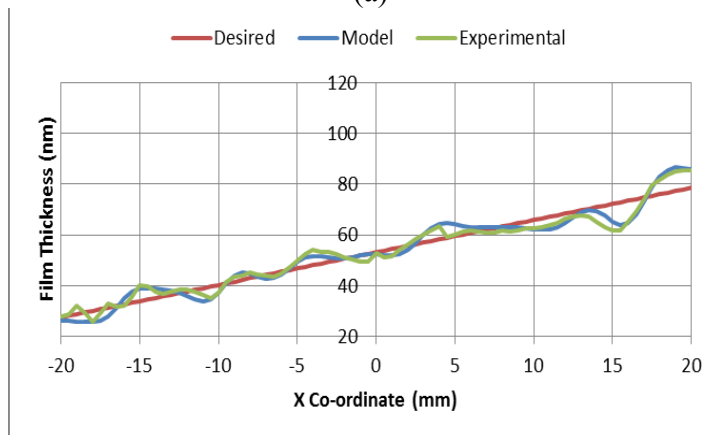
(a)



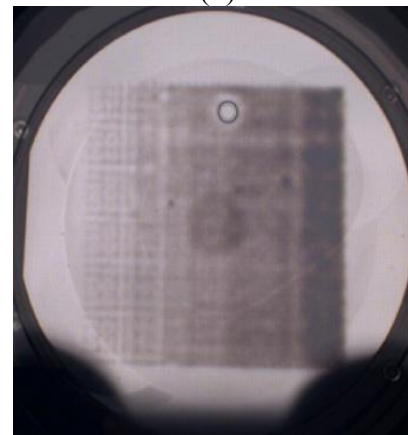
(b)



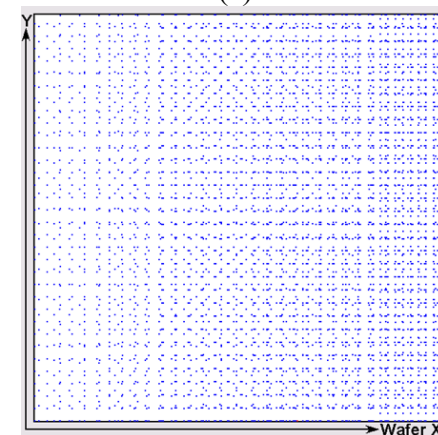
(c)



(d)



(e)



(f)

Figure 5.1: Demonstration of linear gradient surfaces. Plots (a) and (d) compare the experimental data with the model prediction and desired profiles for 6pl and 30pl drops respectively. Images of the deposited films with 6pl and 30pl drops are given in (b) and (e), respectively. The optimal drop locations with 6pl and 30pl drops are given in (c) and (f), respectively.

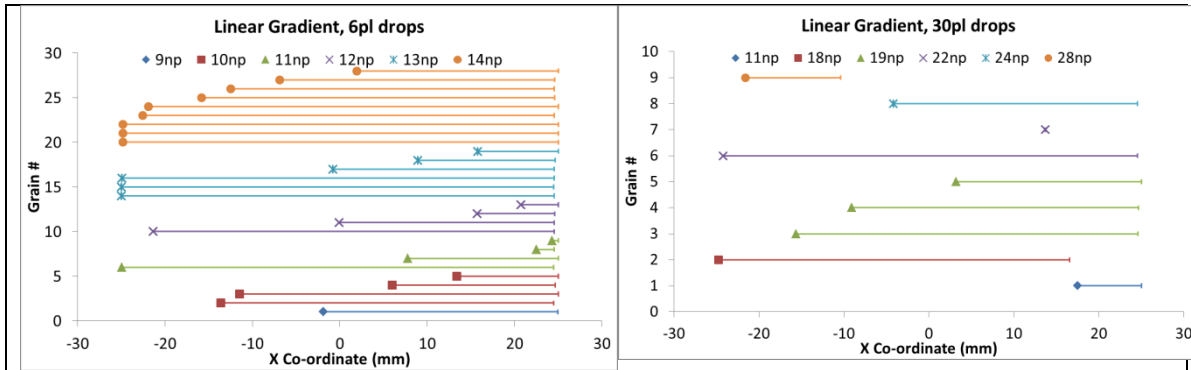


Figure 5.2: Illustration of optimal drop pattern layout for linear gradient surface with 6pl (left) and 30pl (right) drops, with 28 and 9 grains or sub-regions, respectively. In each grain, drops are placed at the same pitch along the lateral extent plotted using the solid horizontal line. The beginning co-ordinate of each grain is marked such that the shape and color of the marker denotes the drop pitch used. In the legend, 'np' signifies the nozzle pitch of 84.5 microns.

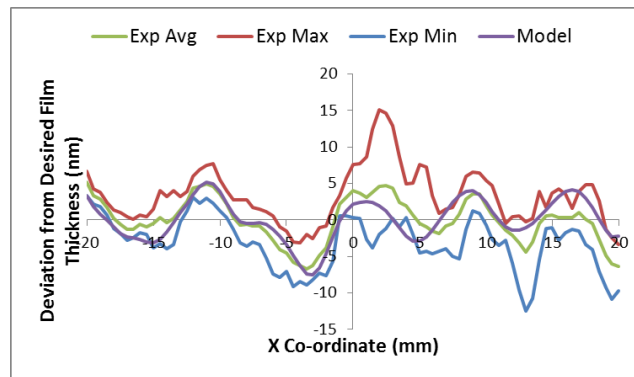


Figure 5.3: Deviation from desired film thickness for the experimental data and model prediction.

A successful demonstration of 1D J-CAST requires the dispensing of drops of same volume throughout the wafer. In practice, however, due to factors such as nozzle clogging and variability in the multi-jet nozzle diameter, the drop volume deviates from the desired value. This is visible in Figure 5.1(b) as horizontal streaks or local changes in color. Also, the reported experimental result is an average of the film thickness across 5 lines (cf. Section 5.1.2). The variability in the experimental data across these 5 lines has been characterized by comparing the maximum, minimum and average deviation of the experimental data from the desired film thickness with the same for the model prediction

in Figure 5.3. Ideally, these plots should exhibit a tendency to be very close to zero. It can be observed that locally, there can be significant deviation from zero or the desired film thickness profile. While the model prediction stays within the bounds of the maximum and minimum experimental deviations almost throughout the wafer, there is significant difference between the experimental maximum and minimum plots. This difference is a result of the variability in drop volume. While causes such as nozzle clogging result in random deviations that can typically be resolved by purging the nozzles to remove any trapped air or ink residue, variability in nozzle diameter leads to systematic errors that can only be eliminated by replacing the inkjet. Moreover, theoretically speaking, these parasitic errors can be accounted for in the J-CAST framework itself to reduce their influence. Such compensation has not been conducted in this work.

Table 5.1: Summary of RMS errors for linear gradient surface with different drop volumes using J-CAST. The cases with 1pl drop volume are only based on simulations and give a measure of the expected errors if such drop resolutions became available.

Drop Volume (pL)	Model – Desired (RMS)	Exp. - Desired (RMS)
30	3.87 nm	3.80 nm
6	2.78 nm	3.04 nm
1	2.41 nm	

The influence of drop volume is further investigated by running an inverse model simulation of a hypothetical case of the same gradient surface with 1pl drops. All results are summarized in Table 5.1, which reveals that with decreasing drop volume, the model prediction matches the desired linear profile more closely. Overall, it can be said that J-CAST can help generate gradient surfaces with zero waste with the help of the inverse model formulation.

5.1.4. Surfaces for X-ray mirrors

The need for surface generation in reflective mirror optics for X-ray based nanoscopy has been reviewed in Section 1.6.2. These surfaces require precise control on their shape and topography to prevent scattering of the short-wavelength X-rays^{47,50}. Given the potential of J-CAST to generate one-dimensional surface profiles, the application of J-CAST for X-ray mirrors was tested for representative elliptical surface profiles with extremely low curvatures. The radius of curvature of the mirrors is typically in the range of one or more kilometer for grazing incidence X-ray optics⁴⁸.

For this purpose, the one-dimensional Cartesian inverse model formulation was invoked, similar to that for the linear gradient surfaces in the previous section. It must be noted that X-ray mirrors require a metallic and not a polymeric surface of the desired figure for proper functioning. Obtaining the same using J-CAST requires the following steps: (i) Metrology of nanotopography of the substrate, (ii) Plugging topography along with the desired figure profile in the inverse model to get the drop pattern, (iii) Deposition of the thin polymer film, (iv) Deposition of a uniform metallic film, and (v) Metrology of the obtained metallic profile. However, for the purpose of demonstrating J-CAST, only step (iii) above was used to deposit the polymeric film, without measuring the topography of the substrate and assuming that it is perfectly flat. This is because the topography of the substrate does not vary in only one dimension. A two-dimensional formulation is needed to compensate for the topography which introduces additional constraints as will be discussed later in Section 5.2.3, and is beyond the scope of this initial demonstration. Hence, as a worst-case scenario, a flat substrate is assumed. Given that the maximum allowable peak-valley variation across the surface for X-ray mirrors is <1nm, this assumption of no topography can be a source of error for this application. The focus of this section is to demonstrate the feasibility of J-CAST for generating low-

curvature surfaces. Subsequent to this preliminary demonstration, true optical flats can be used as substrates to mitigate the influence of parasitic substrate topography and reduce the error caused by the assumption of no topography.

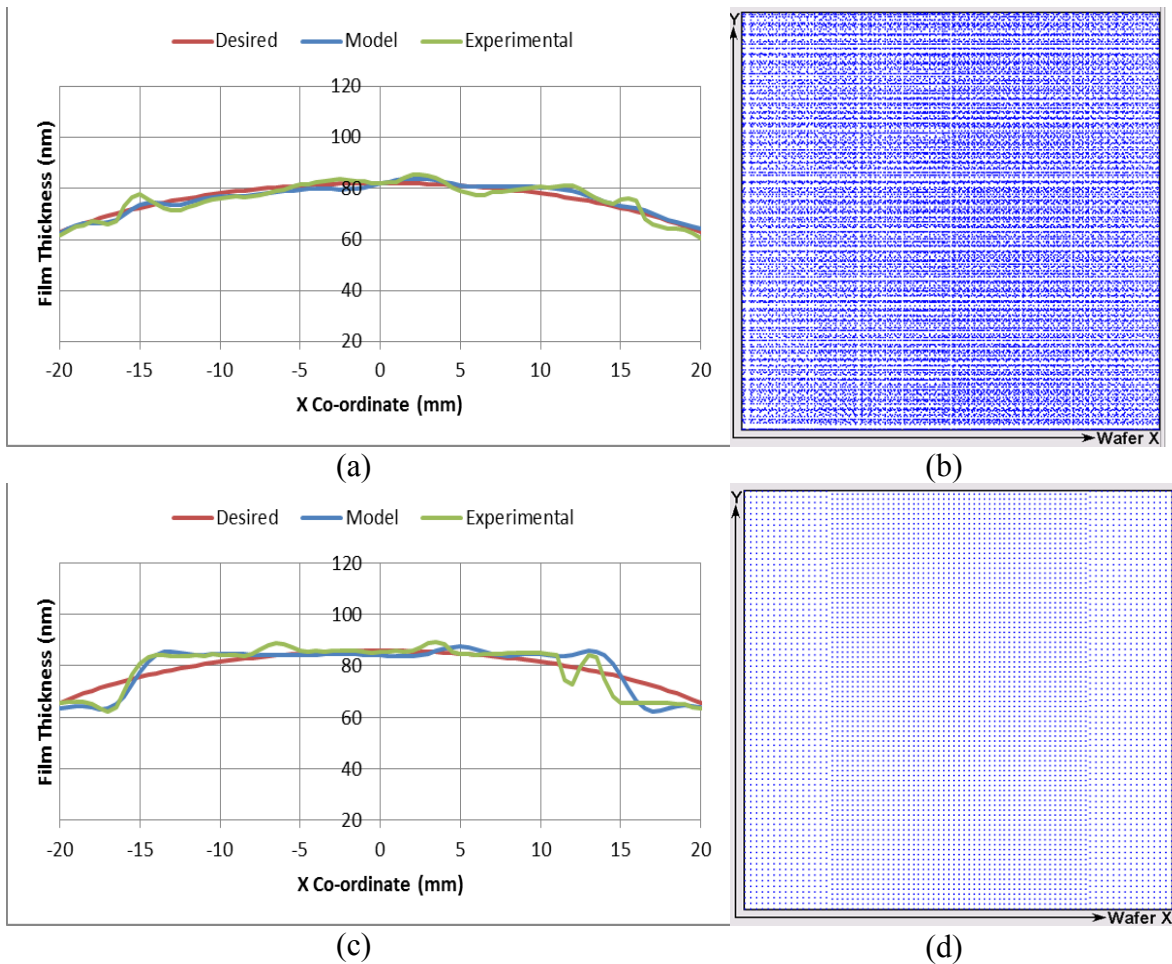


Figure 5.4: Demonstration of $\sim 10\text{km}$ radius of curvature convex elliptical film thickness profile generated using J-CAST. (a) and (c) compare the experimental data with the model prediction and desired variation with 6pl and 30pl drops, respectively. The corresponding optimal drop patterns are given in (b) and (d).

To this end, the optimum transient flow state for a representative low-curvature elliptical film thickness profile in both convex and concave configurations has been obtained from the inverse model. The profiles are given as:

$$\text{Concave: } h_d(x) = 80 - 20 \left(1 - 0.95 \left(\frac{x}{L}\right)^2\right)^{0.5} \text{ nm, and}$$

$$\text{Convex: } h_d(x) = 30 + 50 \left(1 - 0.95 \left(\frac{x}{L}\right)^2\right)^{0.5} \text{ nm, where } L = 25\text{mm and } x \in [-L, L].$$

The convex profile has a radius of curvature of $\sim 10\text{km}$, while the concave profile has a radius of curvature of $\sim 5\text{km}$. Similar to gradient surfaces, both 30pl and 6pl drop volumes have been used to generate the prescribed elliptical film thickness profiles. The experimental results for the convex and concave profiles have been shown in Figure 5.4 and Figure 5.6, respectively.

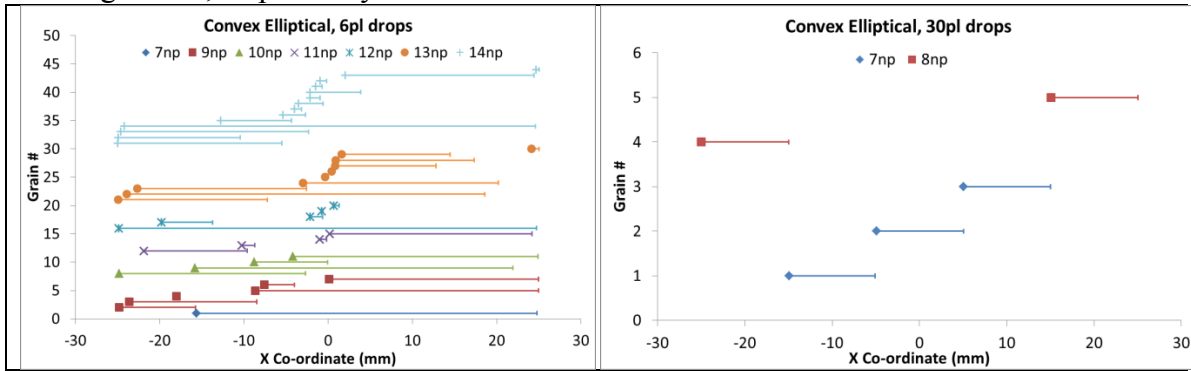


Figure 5.5: Illustration of optimal drop pattern layout for convex elliptical profile with 6pl (left) and 30pl (right) drops, with 44 and 5 grains or sub-regions, respectively. In each grain, drops are placed at the same pitch along the lateral extent plotted using the solid horizontal line. The beginning co-ordinate of each grain is marked such that the shape and color of the marker denotes the drop pitch used. In the legend, 'np' signifies the nozzle pitch of 84.5 microns.

As with the linear gradient surface example, there is very good agreement between the model prediction and the experimentally obtained data for such low-curvature surfaces. Comparing the results across the different drop volumes for both profiles reveals the substantially better surfaces generated with the smaller drop volume of 6pl. In fact, for the lower curvature convex case (Figure 5.4(c)), the optimum film

thickness profile with 30pl drops is very close to a straight line, thereby implying that high volume drops do not have the ability to resolve such low-curvature profiles accurately. For the concave profile with 30pl drops, there are several ripples present that corrupt the curvature locally. These ripples stem from the increased spacing between consecutive drops due to their larger volume. The drop pattern layouts can be compared in Figure 5.5 and Figure 5.7.

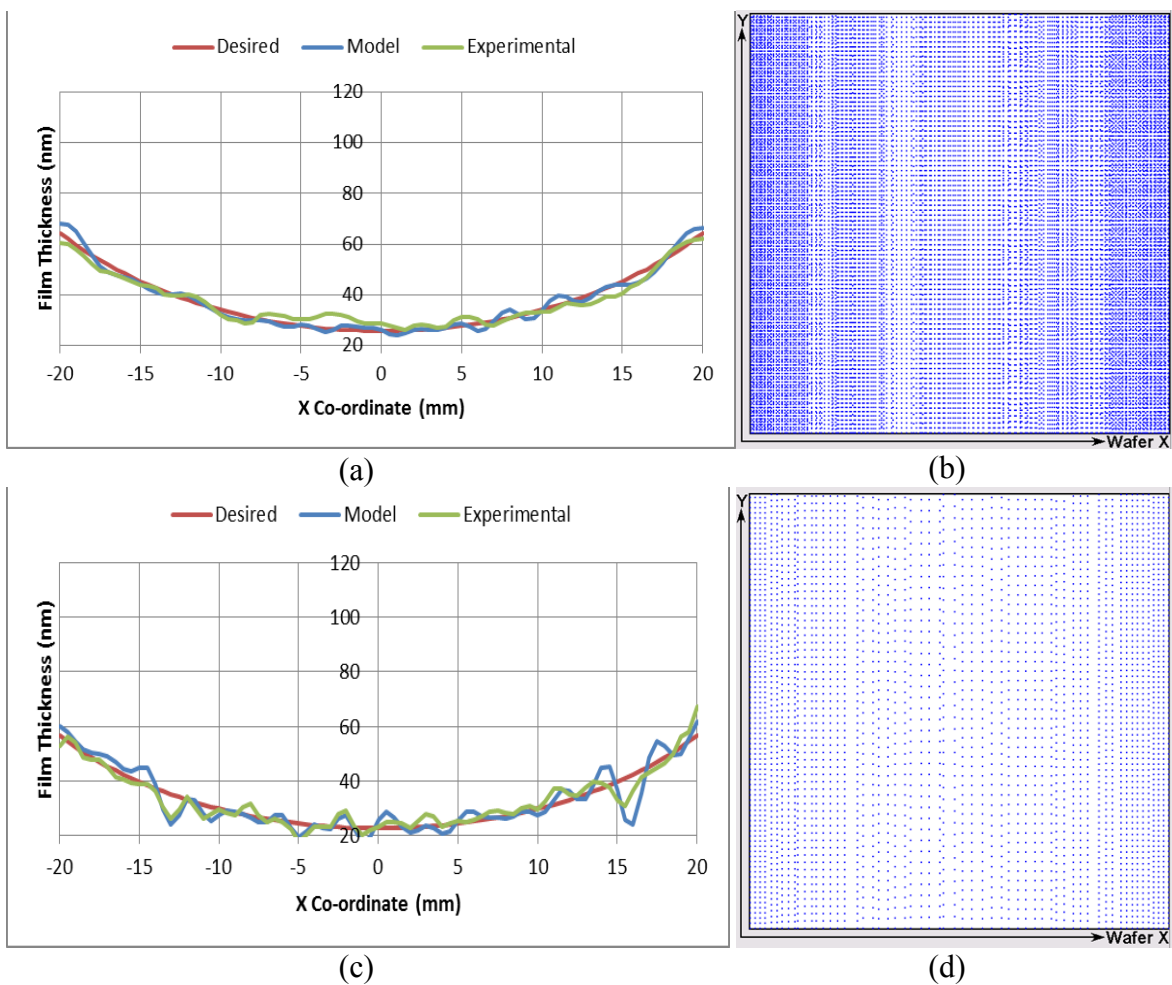


Figure 5.6: Demonstration of $\sim 5\text{km}$ radius of curvature concave elliptical film thickness profile generated using J-CAST. (a) and (c) compare the experimental data with the model prediction and desired variation with 6pl and 30pl drops, respectively. The corresponding optimal drop patterns are given in (b) and (d).

Similar to the gradient surface, a hypothetical case with 1pl drops has also been run. From the summarized results in Table 5.2, it can be seen that smaller drop volumes can indeed lead to a much closer approximation of the desired film thickness profile. In fact, for the low-curvature convex profile, a 1pl drop can approach the surface topography tolerance required for the application of X-ray mirror optics. Thus, overall, J-CAST can be used to create extremely low-curvature film thickness profiles in a single step. Image of the concave profile with 6pl drops has been shown in Figure 5.8.

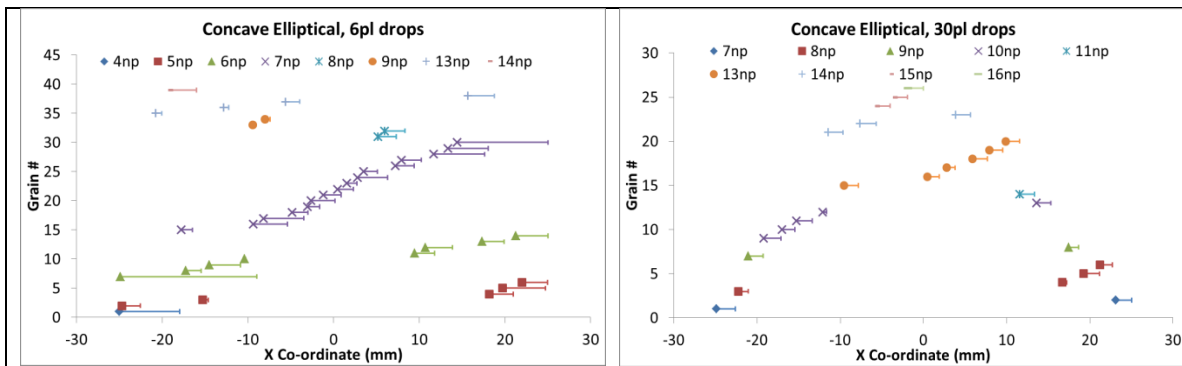


Figure 5.7: Illustration of optimal drop pattern layout for concave elliptical profile with 6pl (left) and 30pl (right) drops, with 39 and 26 grains or sub-regions, respectively. In each grain, drops are placed at the same pitch along the lateral extent plotted using the solid horizontal line. The beginning co-ordinate of each grain is marked such that the shape and color of the marker denotes the drop pitch used. In the legend, ‘np’ signifies the nozzle pitch of 84.5 microns.

Table 5.2: Summary of RMS errors for concave and convex elliptical one-dimensional profiles with different drop volumes using J-CAST. The case with 1pl drop volume is only based on simulations. The approximate desired radius of curvature is given in brackets.

Profile	Drop Volume (pL)	Model – Desired (RMS)	Exp. - Desired (RMS)
Concave (5 km)	30	4.39 nm	3.32 nm
Convex (10 km)	30	4.28 nm	4.28 nm
Concave (5 km)	6	2.02 nm	2.63 nm
Convex (10 km)	6	1.56 nm	2.48 nm
Convex (10 km)	1	0.94 nm	

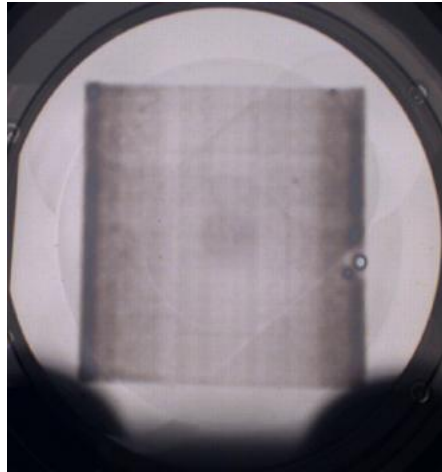


Figure 5.8: Image of the concave profile generated with 6pl drops.

5.2. TWO-DIMENSIONAL J-CAST

One-dimensional and axisymmetric film thickness variations have obvious limitations. Since films are usually deposited over large two-dimensional areas, it is desirable to have a deposition technique that can adaptively cater to two-dimensional film thickness variation. With this motivation, J-CAST has been enhanced to handle such film thickness variations. The targeted application for this version of J-CAST is that of mitigation of wafer topography or polishing of the wafers, where it is required to reduce the two-dimensional topography such that the wafer resembles a flat surface.

5.2.1. Inverse Model Enhancement

For the purpose of implementing J-CAST for two-dimensional film thickness profiles, the inverse model formulation has been augmented in a similar fashion as for one-dimensional profiles. The optimization solver, objective function and primary constraints are similar to those described in Section 4.2. However, there are some key differences for two-dimensional systems that will be described herewith.

The deposition area chosen is a square of side 40mm, although with this formulation, it is also possible to use rectangular areas. The eigenfunctions used are trigonometric in both co-ordinate directions. The boundary conditions, too, are symmetry along all four sides of the deposition area. Unlike the one-dimensional formulation, the drop pitch is not constrained to have the same value in the x and y directions, to allow for variation in either direction individually. The coarse-graining algorithm is also modified for this formulation. While each sub-region in 1D Cartesian co-ordinates consisted of a rectangular strip with the optimization routine solving for the start and end x co-ordinates, the same in 2D is in fact a rectangle, with the optimization routine solving for the x and y co-ordinates of the principal diagonal. This introduces extra output parameters, which adds more expense to the optimization solver. To circumvent this added complexity, the number of sub-regions is held fixed, unlike the 1D and axisymmetric formulations in which the number of sub-regions is allowed to vary from one to a preset maximum. This relieves some of the burden on the optimization solver. At the same time, the presence of a second grid in the y co-ordinate can result in four times the number of grid points if the spatial grid spacing is kept the same. This translates into four times the number of eigenmodes in the eigenfunction expansion, which can add significant computational expense when solving for the ODEs in the eigenmodes as part of the optimization routine. In order to keep computational times reasonable, it thus becomes important to coarsen the grid for 2D co-ordinates. of applications with 1D and axisymmetric profiles was done without accounting for any topography. This allowed for a simple analytical solution of the linearized model as per equation 2.14, which in the absence of topography, is given as:

$$\dot{H}_n = -n^6 H_n \quad \dots 5.1$$

where H_n is the n^{th} eigenmode. This simple formulation enables its use as the core forward model in the inverse optimization scheme without the scheme being prohibitively expensive across multiple iterations. This formulation is also validated by the fact that the predicted profile obtained from the optimization scheme agrees well with the final profile when the optimal initial condition is evolved using the full non-linear model. The presence of topography can, however, complicate this simple analytical solution, even for the linearized model, as can be seen from equation 2.14. It requires at least one matrix inversion per function call, which adds up to substantial computational burden over the duration of a single run of the inverse optimization routine using multiple iterations and function calls for the genetic algorithm solver. Hence, as an approximation, only the sixth-order spatial derivative for the small-amplitude perturbation is considered, while all lower-order derivatives are neglected in equation 2.14. This leads to the following ODE formulation:

$$\frac{\partial \tilde{\epsilon}}{\partial t} = \frac{1}{\pi^6} \tilde{\nabla}^6 (\tilde{\epsilon} + \tilde{w}_s - \tilde{w}_c) \quad \dots 5.2$$

which gives the eigenmode evolution in two dimensions as:

$$\dot{H}_{mn} = -(m^2 + n^2)^3 (H_{mn} + W_{mn}) \quad \dots 5.3$$

where H_{mn} and W_{mn} are film thickness perturbation and topography eigenmodes that correspond to the m^{th} and n^{th} eigenvalues in the x and y co-ordinates, respectively.

Over the course of longer spread times, this approximation leads to significant errors between the profile predicted after the inverse model with this approximation, and that of the full nonlinear model. This shortcoming has been overcome by constraining the spread time to less than 5 seconds, i.e., UV exposure was initiated less than 5 seconds after formation of the contiguous film. This procedure is tantamount to generating an

optimal material distribution based on the topography information with minimal scope for temporal evolution of the substrate-fluid-superstrate sandwich.

Now, the desired goal of the wafer polishing application is to obtain a flat top surface, irrespective of the thickness profile of the underlying film. To this end, the objective function of the optimization scheme has been modified to cancel the effect of the mean film thickness as follows:

$$f = \min \|h_d(x, y) - \bar{h}_d - h^*(x, y, t^*) + \bar{h}^*\| \quad \dots 5.4$$

where h_d is the desired film thickness profile, \bar{h}_d is the mean film thickness of the desired variation, h^* is the optimal transient obtained at the optimal time, t^* and \bar{h}^* is the mean film thickness at the optimal transient. This objective function captures the norm error between the desired and obtained profiles without accounting for the mean film thickness values.

5.2.2. Metrology

The enhancement of the inverse model for 2D co-ordinates has been done to facilitate the application of wafer polishing in which it is desired to mitigate the topography on a wafer surface such that it resembles a flat. In this regard, film thickness metrology is not as important as measuring the surface profile of the wafer before and after the polishing experiment. The surface profile has been measured using the Zygo GPI, an interferometry-based optical surface profiler. It uses a He-Ne laser to measure the reflectance of a nominally flat surface. Since the profiler uses image based processing on a defined number of pixels, the spatial resolution can be made to vary by zooming in and out to decrease or increase the substrate area covered by the number of pixels. For this application, the spatial resolution of the measurements across a full wafer is typically ~ 0.1-0.3 μm .

5.2.3. Wafer Polishing Experiments

For the purpose of preliminary demonstrations of mitigation of wafer nanotopography using J-CAST, three single-side polished Si wafers of 3” diameter have been used. Prior to film deposition, the topography of each wafer has been measured under the Zygo profiler and a square area of side 30mm at the center of each wafer chosen as the desired area over which polishing is desired. The pre-polishing topography for each wafer has been given in Figure 5.9. It can be observed that the peak-valley variation in the wafer topography is substantial, from ~400nm to ~800nm across the three wafers. It is also important to note that all measurements of wafer topography have been carried out with the wafer held by the same chuck that is used on the deposition tool.

This topography field of each wafer is then plugged in the inverse model formulation to obtain the optimal material distribution for a film with a nominally flat surface, irrespective of the mean film thickness. This implies that the film thickness variation across the deposition field is a “negative” copy of the film topography variation. Since substrate topography varies to the order of ~400nm-800nm which is transferred to the film thickness variation, the previously used film thickness metrology setup cannot be used in this exercise to gauge the fidelity of the deposition. This is because of the substantial variation in the film thickness across the spot size of the tool, rendering it unreliable. Hence, a new technique for qualifying the deposition has been used.

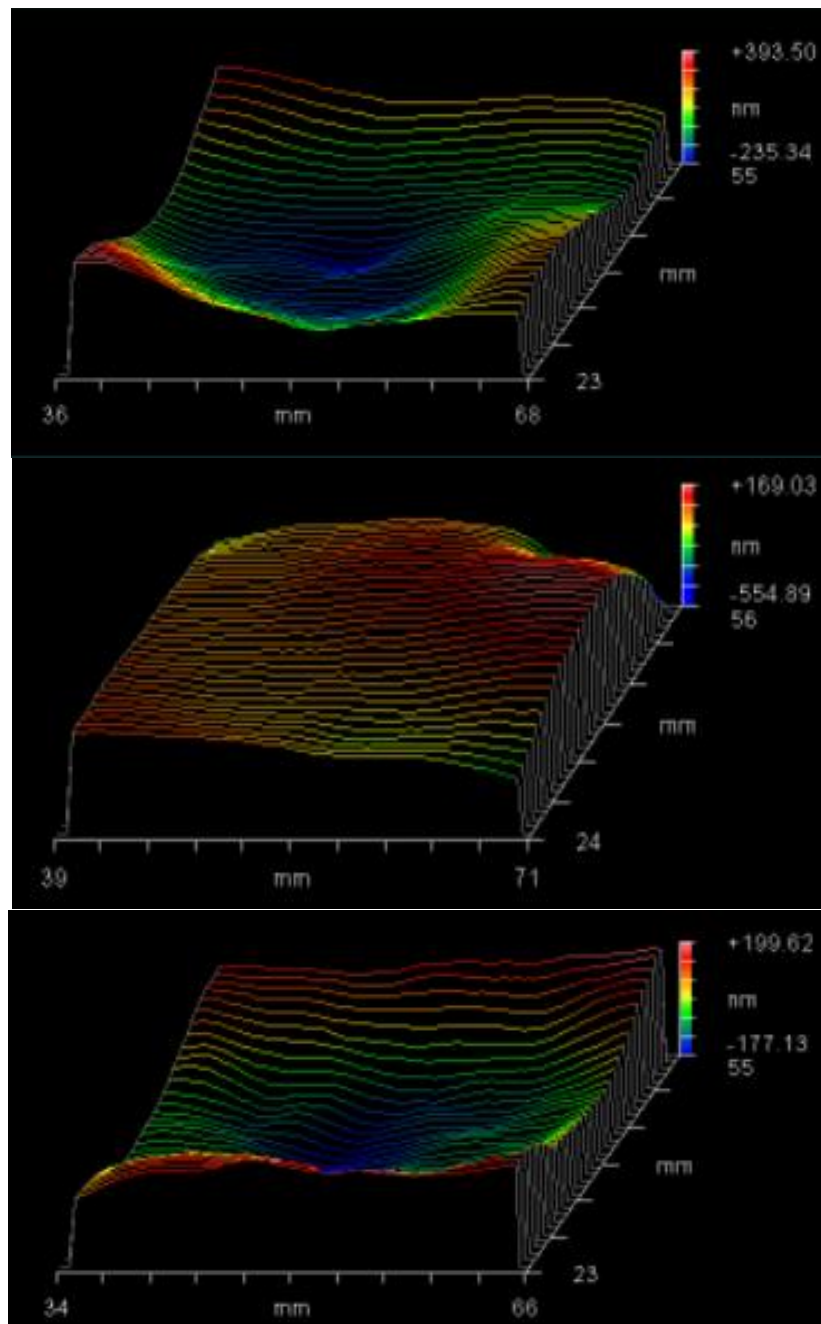


Figure 5.9: Surface topography of Wafers 1-3 (from top to bottom) measured before polishing.

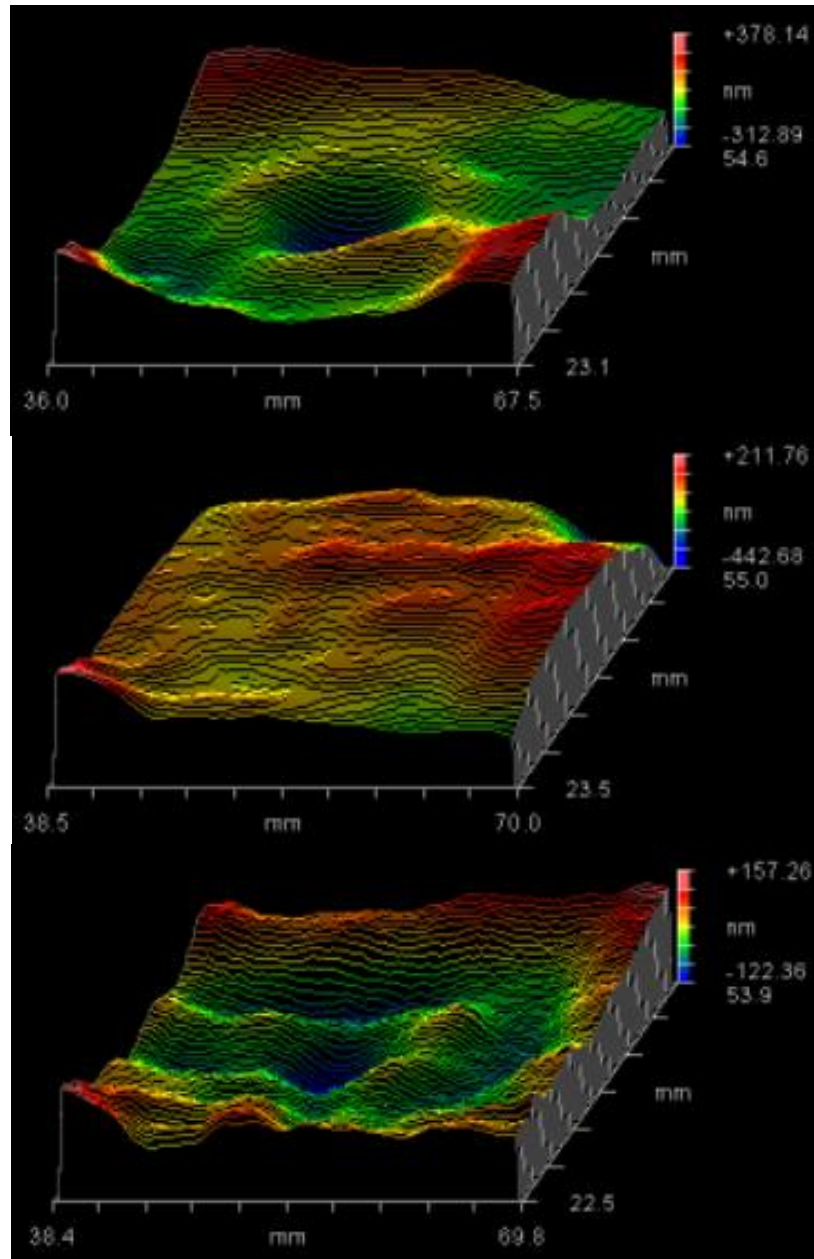


Figure 5.10: Surface topography of Wafers 1-3 (from top to bottom) measured after polishing.

After deposition of the polymer film in accordance with the substrate topography, the deposition of a uniform metallic film on the wafer has been sought. This renders the surface of the polymer film reflective, such that it can be characterized under the Zygo

optical surface profiler. It must be pointed out that this deposition step is not integral to the process flow for wafer polishing, but has only been done to support currently available metrology tools. Now, it is important to keep the thickness of the metallic film sufficiently high such that it has negligible transmittance. This is to avoid any parasitic reflection or interference from the underlying metal-polymer-substrate interfaces. At the same time, the film must be highly uniform so that it does not corrupt the surface profile. To this end, deposition of a ~60nm thick film of Ni was carried out using sputtering, a variant of Physical Vapor Deposition (PVD). The absorption length of Ni for light at 633nm, which is the wavelength of the He-Ne laser used for optical surface profiling, is ~13nm. Hence, a thickness of ~60nm is deemed sufficient to mask the underlying polymer film and prevent parasitic reflection. The measured surface profile for each of the three wafers has been given in Figure 5.10.

While these topography maps are useful to gauge surface profile variations, they do not reveal the effectiveness of the polishing step. For this purpose, the root-mean-square (RMS) deviation from the mean flatness was compared between the surface profiles before polishing and after polishing and metal deposition. The difference between the two RMS deviations has been plotted in Figure 5.11. A positive difference indicates reduction of RMS deviation, indicating a move towards better flatness. It must also be noted that, as compared to the previous demonstrations of J-CAST, this version can be affected by greater number of sources of error. Two major sources of error include:

- (i) Mismatch in the co-ordinate systems between the bare wafer metrology, polymer film deposition and post-metal deposition metrology. This is particularly aggravated in the surface profile metrology, as the substrate loading on the Zygo is done manually.

- (ii) Use of a coarse spatial grid in the inverse model. As mentioned earlier in Section 5.2.1, due to the increased computational burden of solving the inverse model with 2D co-ordinates, the spatial grid needs to be coarsened substantially. The grid spacing used for the computations was $\sim 1.5\text{mm}$, whereas the surface profile was generated with a grid step size of $\sim 0.2\text{-}0.3\ \mu\text{m}$. This mismatch in the spatial resolutions contributed to errors in resolving higher-frequency topography for the inverse model, which ultimately leads to a film thickness profile that does not compensate for the same. An example of such topography is the valley seen close to the center of wafers 1 and 3 in Figure 5.9. The same signature is repeated in Figure 5.10, after polishing, indicating that the coarse grid could not compensate for this feature.

Hence, based on the above discussion, a disagreement between the uncorrected model prediction and the experimental data is expected. This is corroborated by the uncorrected model prediction in Figure 5.11, which yields a much flatter surface, i.e., a greater RMS difference compared to the experimental result. The influence of spatial grid resolution is then studied by refining the spatial grid in the model to match that of the Zygo and regenerating the film thickness profile predicted by the coarse-grid inverse model. The plot of the resolution-corrected model prediction reveals that it reduces the improvement in flatness that had been predicted by the coarse model. Finally, the model prediction after correcting for both, resolution and co-ordinate system reference, has also been plotted in the same figure. It can be seen that the corrected model prediction matches the experimental data much more closely. In general, there is good agreement between the corrected model prediction and the experiment, and a reduction in the RMS deviation is obtained for all cases.

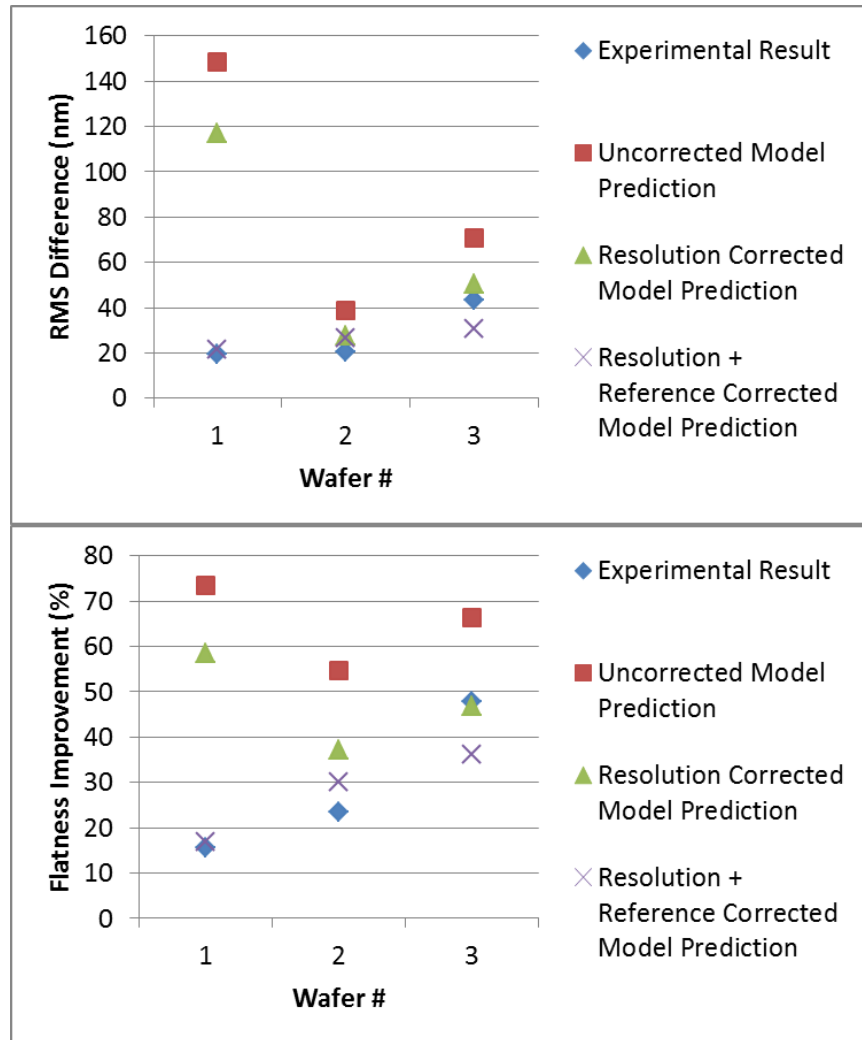


Figure 5.11: Plots of (top) absolute difference of RMS deviation between pre- and post-polishing surface profiles and (bottom) percentage improvement of flatness defined as the ratio of RMS difference with pre-polishing RMS deviation from mean flatness.

Hence, it can be seen that J-CAST can be used for generation of freeform surface profiles that can substantially mitigate the topography of a surface and render it more flat. This can be an alternative to wafer polishing as a significant improvement in the flatness is possible with a single-step of J-CAST. It must be pointed out that the application considered here is different from planarization, which involves mitigation of much higher-frequency topography compared to polishing. From the dynamics of the thin film

evolution as shown in Section 2.1.4, it is evident that the time scale for mitigation of higher-frequency topography is much smaller than the same for lower-frequency topography. Hence, while initially uniform films can lead to a mitigation of high-frequency topography, they find it difficult to reduce low-frequency topography. For the latter, it thus becomes imperative to define the material distribution and prescribe the film thickness variation in accordance with the topography as has been done with J-CAST in this section.

5.3. SUMMARY

In this chapter, demonstration of J-CAST has been done for applications that require prescribed film thickness variation as well as freeform surface profiles. First, the inverse model formulation was augmented to account for non-axisymmetric film thickness variations in one-dimensional Cartesian co-ordinates. Using this formulation, linear gradient surfaces for combinatorial materials research, as well as ultra-low curvature surfaces with radius of curvature approaching 10km for optical elements in X-ray nanoscopy, were generated with excellent agreement between the model prediction and experimental result. Then, the same formulation was further enhanced to incorporate film thickness variations in the second Cartesian co-ordinate as well. This was used to generate freeform film thickness profiles that mitigated the topography of representative wafers and improved upon their flatness.

Chapter 6: Deposition of Uniform Films on Flexible Substrates

Extending J-CAST on R2R systems has the potential of significantly lowering manufacturing costs for commodity products. As opposed to the standard wafer-based processes, R2R processing requires deposition on highly flexible substrates. These substrates, or webs, are typically made of plastic with elastic modulus between 1-10GPa and thickness \sim 100-200 μ m. They are usually held under uniaxial tension as they are being processed. These material properties and loading lend some distinct characteristics to R2R systems that are different from deposition on rigid substrates. The presence of uniaxial tension can introduce possibilities of buckling or wrinkling failure^{93,94}, as well as additional sources of film thickness non-uniformity. Moreover, these webs can also have significant nanotopography due to the presence of surface defects and lack of compatibility of the plastic material with standard polishing techniques. Hence, using similar model-based analyses supported by experimental validation, a preliminary investigation of J-CAST for R2R systems has been conducted.

6.1. WEB BUCKLING

The mean uniaxial tension and its variation along its axis of application introduce an in-plane stress field in the substrate. This tension is necessary to stiffen the flexible substrate, enabling the template or superstrate to initiate drop spreading and merging and for the deposited film thickness to be uniform. Also, any out-of-plane displacement disturbs the well-defined deposition plane and can be catastrophic for the overall process. It is important to note that though the in-plane stress field is mostly tensile parallel to the direction of application, it has a compressive component normal to the application direction, due to the Poisson effect. This can initiate buckling causing significant out-of-plane displacement, as shown in Figure 6.1. From classical solid mechanics, it is known

that buckling leads to catastrophic failure, but only beyond a critical load. Extending this to the nominal system of a web under uniaxial tension, it is important to understand the range of this critical load for typical process conditions and suggest possible measures to avoid buckling failure.

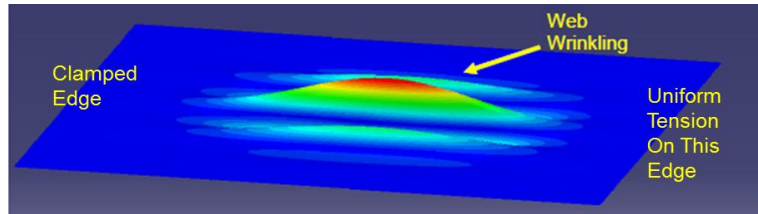


Figure 6.1: Illustration of buckling in a web under uniaxial tension

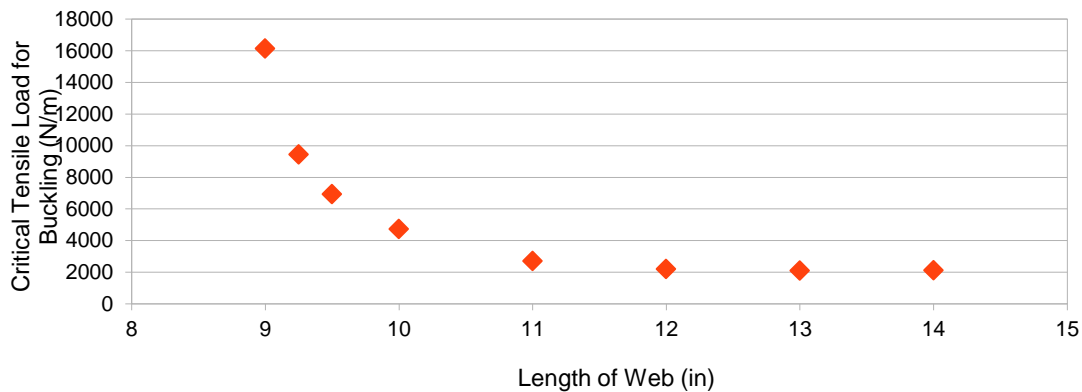


Figure 6.2: Plot showing variation of critical buckling load with varying web length. The width and thickness of the web are constants at 7” and 0.125mm respectively. The material is PET with an elastic modulus of 3GPa and Poisson’s ratio of 0.4.

To this end, finite-element simulations have been conducted using the commercial FEA solver, Abaqus 6.8. The material of the web has been chosen as PET, which is a commonly used plastic substrate. Its elastic modulus and Poisson’s ratio are 3GPa and 0.4 respectively. As representative values for the analysis, the thickness and width of the web has been fixed at 0.125mm and 7” respectively. The length of the web has been

varied upwards of 9” to capture its effect on critical buckling load. The boundary conditions consist of zero spanwise displacement for the edges under applied tension. Results have been plotted in Figure 6.2. As can be seen, the critical buckling load approaches an asymptotic value of 2000N/m for webs with length > 11 ”. For shorter webs, the critical load increases drastically until it is in excess of 16,000N/m for 9” length. Hence, this study implies that the shorter the length of the web, the less likely it is to buckle. At the same time, the asymptotic nature of the critical buckling load marks an upper limit for the applied tension, so that buckling can be completely avoided. While these values will change based on the geometry of the web, it can still be inferred that the ratio of length with width of the web should be kept less than ~ 1.5 to avoid hitting the asymptotic limit of the critical buckling tension.

An important parallel consideration is tensile failure of the web under its current loading scheme. Going with the same example, the typical yield stress for PET is ~ 50 MPa. Given the dynamic nature of loading in a complete R2R system, a safety factor of 5 is considered appropriate from standard design principles. This implies that the tensile stress in the web cannot exceed 10MPa, which translates into a line load of 1250N/m for a 0.125mm thick web. This is much lower than the asymptotic critical buckling load of 2000N/m and hence, reveals that buckling is not a concern for the given geometry under uniaxial tension. These rules can be used as guidelines for designing the web loading schemes in R2R systems.

6.2. THIN FILM EVOLUTION MODEL

The evolution of the superstrate-fluid-substrate sandwich can be modeled similar to the baseline model in Chapter 2. The primary departure from the previously discussed model is that the substrate is now no longer rigid and can flex under the action of the

fluid pressure, similar to the superstrate. While the flexural rigidity determines the bending deformation of the superstrate, the substrate is primarily held under uniaxial tension and has negligible resistance to bending. The basic modeling of this system has been discussed next. This is followed by a qualitative experimental validation of the trends established by the model. The experiments have been conducted on the LithoFlex 100, which is a 1st generation J-FIL tool designed specifically for flexible substrates in a R2R configuration.

6.2.1. Basic Modeling

The evolution of the superstrate-fluid-substrate sandwich proceeds with similar dynamics as that in the baseline case, which is given by:

$$12\mu \frac{\partial h}{\partial t} = \frac{\partial}{\partial x} \left(h^3 \frac{\partial p}{\partial x} \right) \quad \dots 6.1$$

where the symbols have their usual meaning. This is the same as equation 2.4. Now, the pressure field causes deformation of both the superstrate and the substrate. The superstrate deformation is given as:

$$p = D \frac{\partial^4 y_c}{\partial x^4} \quad \dots 6.2$$

where $y_c(x, t)$ is the deformation field on the superstrate. From classical membrane theory⁶⁷, the deformation field on the substrate is given as:

$$-p = -T \frac{\partial^2 y_s}{\partial x^2} \quad \dots 6.3$$

where $y_s(x, t)$ is the deformation field on the substrate and T is a line tension (force per unit length) applied to the flexible substrate or web. It must be noted that the pressure field on the substrate reverses sign as compared to that on the superstrate, although the absolute value stays the same. This is because the fluid pressure is the same in all directions. Combining equations 6.2 and 6.3 gives:

$$D \frac{\partial^4 y_c}{\partial x^4} = T \frac{\partial^2 y_s}{\partial x^2} \quad \dots 6.4$$

which when integrated twice gives:

$$\frac{D}{T} \frac{\partial^2 y_c}{\partial x^2} = y_s + c_0(t) + c_1(t)x \quad \dots 6.5$$

The substrate and superstrate deformations can then be related to the fluid film thickness, $h(x, t)$ and the time-invariant substrate and superstrate topography, $w_s(x)$ and $w_c(x)$, respectively. This is illustrated in Figure 6.3 and given below:

$$-y_s + y_c = h + w_s - w_c \quad \dots 6.6$$

Substituting equation 6.5 for y_s in equation 6.6 gives:

$$h + w_s - w_c - y_c = \frac{D}{T} \frac{\partial^2 y_c}{\partial x^2} - c_0(t) - c_1(t)x \quad \dots 6.7$$

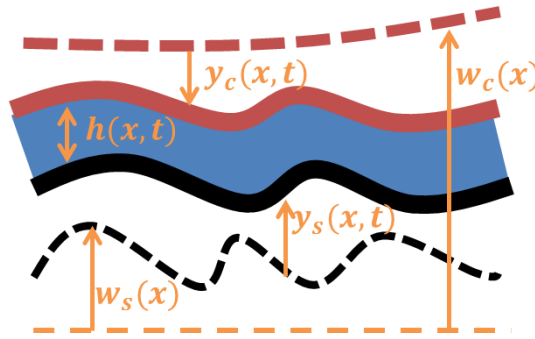


Figure 6.3: Illustration of superstrate-fluid-substrate sandwich for a flexible substrate. The superstrate is given in red, fluid in blue and substrate in black. The solid lines represent instantaneous positions of the superstrate and substrate, while the dashed lines indicate the equilibrium topography to which the system tends to relax. All measurements are made against a reference flat shown as a dashed orange line.

Next, homogeneous symmetry boundary conditions similar to the baseline case are assumed which allows the expression of the important variables in the spectral domain as given below:

$$h(x, t) = \sum_n H_n \cos(\lambda_n x) \quad \dots 6.8$$

$$w_s(x, t) - w_c(x, t) = \sum_n W_n \cos(\lambda_n x) \quad \dots 6.9$$

$$y_c(x, t) = \sum_n Y_n \cos(\lambda_n x) \quad \dots 6.10$$

Substituting the above equations 6.8-6.10 in equation 6.7 gives:

$$Y_n = \frac{H_n + W_n}{1 + \frac{D\lambda_n^2}{T}}, \text{ such that } y_c(x, t) = \sum_n \frac{H_n + W_n}{1 + \frac{D\lambda_n^2}{T}} \cos(\lambda_n x) \quad \dots 6.11$$

The pressure field, as given by equation $p = D \frac{\partial^4 y_c}{\partial x^4}$...6.2, is therefore given as:

$$p(x, t) = D \sum_n \frac{H_n(t) + W_n(t)}{1 + \frac{D\lambda_n^2}{T}} \lambda_n^4 \cos(\lambda_n x) \quad \dots 6.12$$

On the other hand, the pressure field in the baseline case from equations 2.5 and 2.11 was given by:

$$p(x, t) = D \sum_n (H_n(t) + W_n(t)) \lambda_n^4 \cos(\lambda_n x) \quad \dots 6.13$$

Comparing the two cases reveals that the only difference is the presence of a denominator that is greater than 1. This essentially implies that the amplitude of the pressure field is lowered when the deformation of the flexible substrate is also considered. Overall, when substituted in the governing equation, this translates into an increase in the process time scale, which is defined by the characteristic time scale of evolution of the longest spatial wavelength, as:

$$\tau = \frac{12R^6\mu}{\pi^6 D h_0^3} \left(1 + \frac{D\pi^2}{TR^2} \right) \quad \dots 6.14$$

The corresponding non-dimensional spread time is thus $\tilde{t} = \frac{t}{\tau}$. Increasing non-dimensional spread time leads to increasing non-uniformity as explained in Chapter 2 and Chapter 3. An increase in the process time scale compared to the baseline case can be explained by observing that $T \rightarrow \infty$ for a rigid substrate. Hence, the ratio of D with T is negligibly small, thereby keeping the bracketed term in equation 6.14 close to 1 and approaching the time scale for the baseline case. For the physical process, this implies that the “infinite” rigidity of the substrate results in an instantaneous relaxation of the substrate to its time-invariant equilibrium state. Hence, there is no contribution of this relaxation to the process time-scale. On the other hand, with a flexible substrate, the finite

rigidity leads to a finite non-zero relaxation time, which manifests as an increase in the overall process time scale compared to the baseline. This relative increase, which essentially translates to $\left(1 + \frac{D\pi^2}{TR^2}\right)$, has been plotted in Figure 6.4 for $R = 33.5\text{mm}$. For low values of T , the increase in process time scale is substantial, while at high values of T , the relative value approaches 1, particularly for lower D .

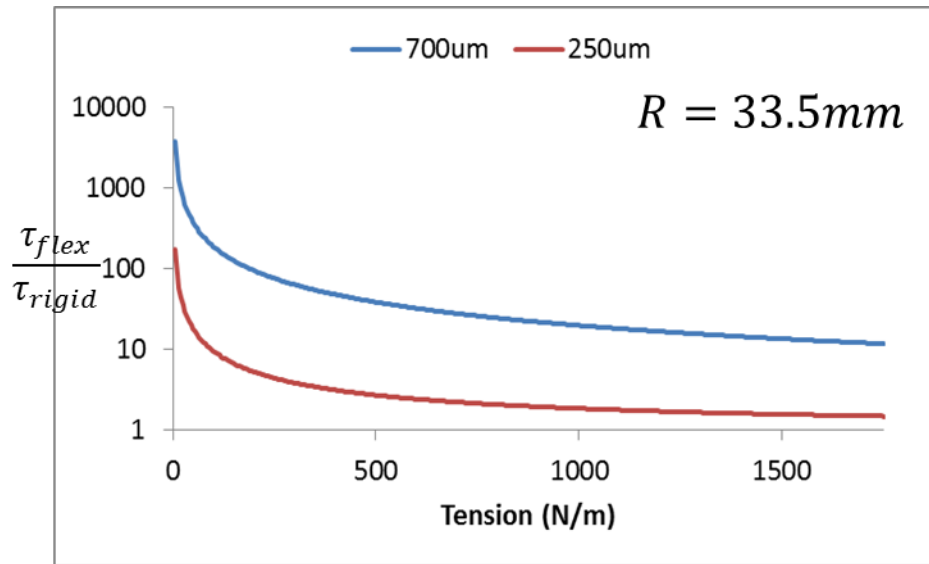


Figure 6.4: Plot showing the ratio of time scale for flexible versus rigid substrate for $R = 33.5\text{mm}$ and superstrate thicknesses of 700um and 250um with varying web tension.

6.2.2. Qualitative Validation

Preliminary experiments have been conducted on the LithoFlex 100 to verify the parameter dependence of the process time scale in the presence of a flexible substrate. Firstly, web buckling is not a concern for the tool, because the length to width aspect ratio is 1.2, which is lower than the value of ~ 1.5 needed to reach the asymptotic lower limit of critical tension. Secondly, web tension is applied only during the web loading and unloading stages and the web used is relatively thick, $\sim 175\mu\text{m}$. Hence, buckling is not a concern and is not evident during operation of the tool. The plastic substrates are

protected on the active side by a very thin protective film. This helps keep the surface clean. The protective film is peeled off on the tool itself prior to the deposition step. The active surface is also pre-treated to enhance wetting and spreading of the monomer drops prior to formation of the contiguous film and also facilitates separation of the superstrate. This pre-treatment is done by the vendor itself, which eliminates the need of an adhesion layer such as the one used on rigid wafers.

Although it is ideal to conduct quantitative validation of the thin film evolution model, there are significant metrology constraints that impede the same. The current film thickness metrology tool is only applicable for films deposited on nominally flat reflective surfaces. For plastic substrates, such as PET or PC, both these conditions do not apply. This is because they are translucent and can have significant departure from nominal flatness due to variations in thickness, which again is difficult to quantify because the Zygo optical surface profiler too relies on reflective surfaces. Local film thickness can be obtained through cross-section scanning electron microscopy (SEM), which is useful for studying patterns locally, but has limited feasibility towards analyzing large areas.

Metal-coated flexible substrates are a way to get a reflective surface, but this introduces additional constraints. These substrates do not have a protective film covering the active side, as with the non-metal coated ones. This leads to significant contamination due to particles and scratches related to handling of the substrates, which again is not desirable for the process as it can cause permanent damage to the superstrate. Moreover, these substrates are not pre-treated to increase their surface energy, thereby causing problems during wetting and separation of the superstrate.

An additional issue is the lack of knowledge of the exact value of applied tension, which is necessary to calculate the modified process time scale as per equation 6.14. This

is because there are no sensors or load cells directly attached to the rollers between which the substrate is supported during the deposition step. The tool control system cannot modulate tension across continuous analog values. There are only four preset slabs across which tension can be varied. They are zero, low, medium and high tension. The values for these slabs are modulated according to the torque on the motors. There is no direct calibration of the motor torque to tension values because of the presence of several parasitics such as machine compliance, friction torque etc. Because of these multiple reasons, quantitative metrology and subsequent validation is infeasible with the given tool infrastructure.

Hence, qualitative validation has been done by analyzing images of different thickness films deposited on the same roll of a poly-carbonate film of 175 μ m thickness under different process conditions. Like with rigid wafers in Section 2.2, enhanced granularity implies an increase in the non-dimensional process time. A summary of the experimental results has been presented in the images in Figure 6.5. These images lack good contrast because of the translucent substrate, but some features of the non-uniformity can be gleaned from the same.

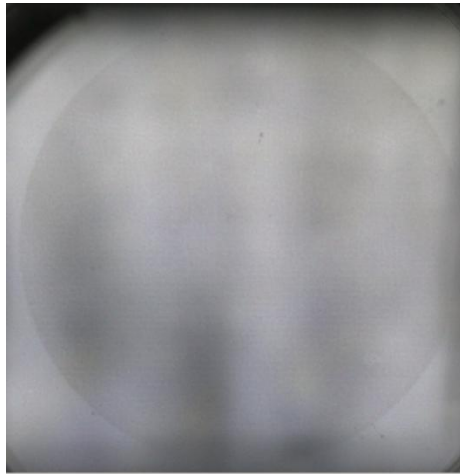
The basic trends predicted by the model can be seen in the set of images. Comparing Figure 6.5 (a) and (c), and (b) and (d) respectively, it can be seen that increasing the mean film thickness (or total dispensed volume) leads to increasing granularity. Increasing the spread time also leads to increasing non-granularity. This is evident when Figure 6.5 (c) and (d), and (e) and (f), respectively, are compared. This is less evident, however, when Figure 6.5 (a) and (b) are compared, implying that the non-dimensional spread time is on the lower side even for the long spread time case of Figure 6.5 (b).

An interesting comparison is observed between Figure 6.5 (c) and (e), and (d) and (f), respectively, with respect to the effect of change in superstrate thickness from 700um to 250um. For the baseline case, this change is significant enough to cause a marked change in the visually observed granularity, as seen in Figure 2.9 and Figure 3.3. However, with the flexible substrate, there is negligible change in the observed granularity. This can be explained by rearranging the terms in equation 6.14 to:

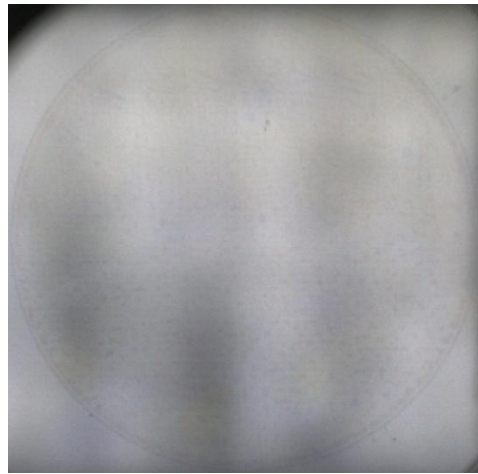
$$\tau = \frac{12R^4\mu}{\pi^4Th_0^3} \left(1 + \frac{TR^2}{D\pi^2}\right) \quad \dots 6.15$$

Given that the applied substrate tension is very small during the deposition step, the ratio of the same tension with superstrate rigidity remains low across varying superstrate rigidity. Hence, for varying superstrate rigidity, D , the bracketed term $\left(1 + \frac{TR^2}{D\pi^2}\right)$ essentially remains constant. This implies that the process time scale does not change significantly by changing the superstrate thickness, at least across the values permissible by the experimental setup.

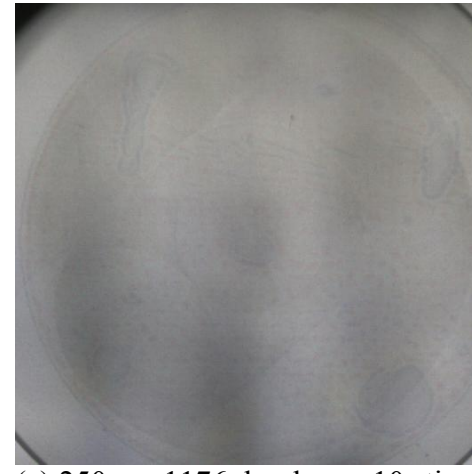
This has also been explained through Figure 6.6, where the effect of changing superstrate thickness from 700um to 250um on the process time scale has been plotted as a ratio of the process time scale at 250um with the same at 700um, which translates to $\frac{\left(1 + \frac{TR^2}{D_{250}\pi^2}\right)}{\left(1 + \frac{TR^2}{D_{700}\pi^2}\right)}$. The effect has been captured across different tension values for the flexible substrate and the baseline rigid substrate for $R = 33.5\text{mm}$. The plot reveals that changing superstrate thickness for the baseline rigid substrate results in a substantial 22-fold increase in the time scale, thereby providing a sound basis to the thinning of superstrates to slow down the dynamics. However, for the flexible substrate, this increase is much more modest, as the ratio varies from ~ 1 for low tensions to ~ 2.75 when the applied tensile stress approaches the yield stress. Hence, there is no significant benefit to be had by reducing the superstrate thickness for depositing films on flexible substrates.



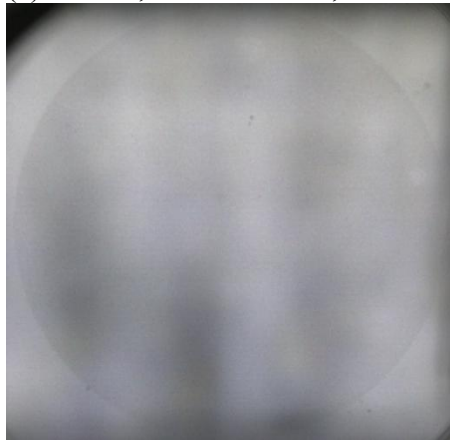
(a) 700um, 392nl volume, 10s time



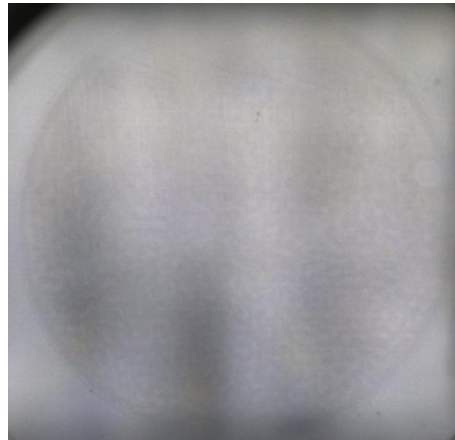
(c) 700um, 1176nl volume, 10s time



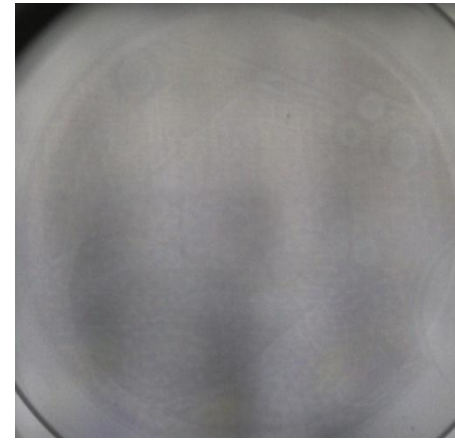
(e) 250um, 1176nl volume, 10s time



(b) 700um, 392nl volume, 100s time



(d) 700um, 1176 nl volume, 100s time



(f) 250um, 1176nl volume, 100s time

Figure 6.5: Images of various films deposited on the flexible substrate with varying superstrate thickness, mean film thickness and time.

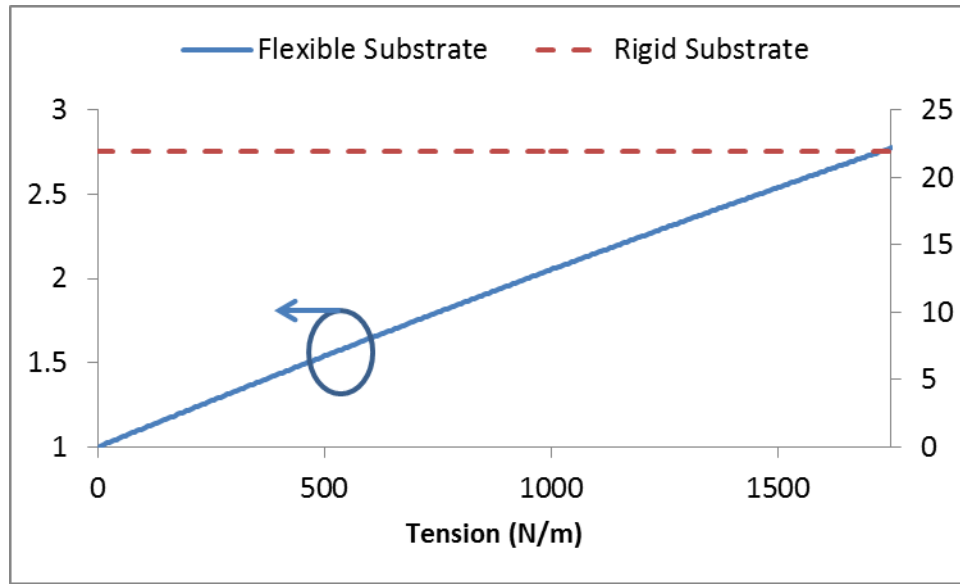


Figure 6.6: Plot depicting the relative value of process time scale for 250 μ m superstrate against the 700 μ m superstrate for both flexible and rigid substrates with increasing tension. The flexible substrate case has been plotted on the left y-axis, whereas the rigid substrate case has been plotted against the right y-axis.

6.3. SUMMARY

In this chapter, a preliminary investigation of uniform film deposition using J-CAST has been conducted for flexible substrates in a roll-roll configuration. These substrates can suffer from catastrophic buckling failure if the applied tension exceeds a critical value. Moreover, the ability of the substrate to also deform modifies the evolution dynamics of the superstrate-fluid-substrate sandwich. As opposed to the baseline case of rigid substrates, the superstrate thickness does not have a substantial influence on the process time scale. This allows the use of thick superstrates to achieve the desired uniformity levels. Given the lack of quantitative metrology for these substrates, qualitative experimental validation has been conducted to confirm the influence of process parameters such as film thickness, spread time and superstrate thickness on the deviation from uniformity.

Chapter 7: Conclusions

This dissertation demonstrates a novel zero-waste process called Jet-and-Coat of Adaptive Sustainable Thin Films or J-CAST for the deposition of nanoscale polymer thin films. The demonstrated process has the ability to deposit uniform films from ~20nm to ~500nm with the RMS error from uniformity not exceeding 2% of the mean film thickness. Moreover, J-CAST can also be used for the deposition of films with prescribed variation in film thickness across mm-scale spatial wavelengths with no physical changes to the system used for depositing nominally uniform films. Films with (i) linear gradients in thickness, (ii) ultra-low curvatures with radius of curvature of the order of 10 km as well as (iii) non-monotonic sinusoidal variations in thickness have been demonstrated using J-CAST. This ability of the process has been enabled by an inverse optimization scheme that is based on an experimentally validated forward model.

7.1. INTELLECTUAL MERIT

The novelty of the research conducted in this dissertation can be broadly classified as the development of a modeling and simulation framework for J-CAST, which has been implemented in a process control and optimization scheme.

The J-CAST process involves the dynamics of a thin film of fluid sandwiched between a superstrate and a substrate, of which the superstrate can flex under the action of fluid pressure. Hence, a novel baseline model has been developed that captures this coupling of thin film fluid flow (based on lubrication theory) with elastic bending (based on thin plate deformation) and identifies a characteristic process time scale that lumps the different process parameters, such as fluid viscosity, thin plate in one quantity. This baseline model has also been experimentally validated.

From the model, it was revealed that shorter time scales lead to rapid equilibration of the system and consequently, a greater influence of parasitics such as any nominal time-invariant topography on the superstrate or substrate. Hence, it was desired to move away from equilibrium by purposely slowing down the dynamics of the system by thinning the superstrate. For films with prescribed thickness profiles, this also opened up the possibility of exploiting a plethora of non-equilibrium transients to attain the desired profiles, without the influence of parasitics. This is contrary to conventional approaches in similar sandwiched fluid systems that rely on equilibration to achieve a singular end objective, and hence, cannot cater to different film thickness profiles adaptively.

The ability to capture an optimum non-equilibrium transient rests on determining an appropriate initial condition for the system and subsequently, evolving the same initial condition to the desired non-equilibrium state. This has been enabled with the help of an inverse optimization approach, which optimizes the initial placement of material in accordance with the desired profile. In fact, the final film thickness profile is primarily governed by this initial material distribution rather than any topography on the substrate or superstrate. This allows the J-CAST process to be versatile across various film thickness profiles, as has been demonstrated in this research.

Extending the baseline model to flexible substrates held under tension in a roll-roll configuration reveals that, indeed, similar to rigid substrates, a reduction in process time scale is imperative to reduce the influence of parasitics. However, compared to rigid substrates, the dependence of this process time scale on superstrate thickness is rather modest for allowable values of applied tension. This result is novel and can preclude the thinning of superstrates for achieving better uniformity on flexible substrates.

7.2. BROAD IMPACT

Deposition of nanoscale thickness films is ubiquitous in micro- and nano-scale device manufacturing. The ability and versatility of J-CAST to deposit films across a range of uniform thicknesses as well as prescribed thickness variations, without any additional hardware, enables its use over a broad spectrum of applications, including those for freeform surface generation. Some of these applications in the areas of ultra-low curvature optics, combinatorial materials science and semiconductor manufacturing have been discussed and demonstrated in this dissertation. J-CAST substantially leverages tool infrastructure already commercialized for Jet-and-Flash Imprint Lithography (J-FIL). In addition, its intrinsic zero-waste characteristics and compatibility with high-throughput roll-roll systems, also render J-CAST attractive for integration in a manufacturing framework. This can have extremely high impact in the fabrication of a variety of commodity and high-end products.

7.3. FUTURE WORK

This dissertation serves as a seminal exploration into the physics and operation of the J-CAST process. With additional effort, J-CAST can be made into a one-stop manufacturing solution for a much broader variety of applications. This involves exploring J-CAST with different inkjettable materials, including metal nanoparticles, polymer blends or even Si-based dispersions. The fundamental evolution dynamics of the sandwiched thin film can be used to adaptively deposit a range of different materials amenable for the desired application. For example, an optimal thickness profile of single-layer or even multi-layer anti-reflection coatings made of different materials can be deposited on high-end Si device wafers to compensate for parasitics, such as topography or illumination non-uniformity in subsequent photolithography steps⁹⁵. This can potentially lead to lower consumable cost, higher yield and may even lead to a relaxation

of the stringent constraints on allowable wafer topography. In addition to the use of different materials, its versatility can be extended by exploring J-CAST in conjunction with nano-patterning to obtain prescribed variation in feature dimensions on a single substrate. This can have potential utility in photonics, where for example, varying quantum dot dimensions can lead to a programmed variation in the plasmonic response⁹⁶.

Even in its current form, there are several technical challenges that need to be overcome to improve upon the reliability and accuracy of J-CAST. These challenges mostly stem from a process control perspective. Perhaps, the most significant challenge is in developing an optimization framework such that the location and volume of each dispensed drop can be optimized without any coarse-graining. This will enable the deposition of films with sub-1mm characteristic wavelengths. Such an optimization framework is not trivial, given that deposition of sub-100nm films over entire wafers may need in excess of 10,000 such drops. Moreover, this can give rise to systematic and random uncertainty related to variations in drop volume or drop location that can influence the behavior of the system. Hence, a simultaneous analysis of uncertainty quantification and propagation is also imperative. Moreover, for J-CAST to be an adaptive manufacturing solution, the inverse optimization scheme needs to work in real-time, ideally. This implies that the drop patterns need to be generated on the fly upon knowledge of the desired film thickness profile and any parasitics, such as surface topography, which can be a technical challenge, especially in conjunction with control over each individual drop.

Further improvements in the J-CAST process can be conducted by understanding and quantifying fundamental process limits. These limits are influenced by hardware constraints, such as nozzle pitch; material constraints, such as volume and spreading radius of an individual drop as well as parasitics such as substrate topography wavelength

and amplitude. In its current form, the process relies on the optimization framework with a coarse-graining algorithm that results in a loss of resolution in the film thickness amplitude and wavelength achievable by the process. With an enhanced optimization framework, the relation between the process limits discussed above as well as what can be fundamentally achieved given the propensity of the superstrate to dissipate its strain energy through the fluid viscosity can be obtained. Such a relation is not possible analytically and obtaining the desired result requires a stochastic Bayesian or Monte-Carlo type simulation without any losses from the computational framework. This is potential future work for J-CAST.

References

1. Sreenivasan, S. V., Choi, B. J., Schumaker, P. D. & Xu, F. Status Of UV Imprint Lithography For Nanoscale Manufacturing. *Comprehensive Nanoscience And Technology* **4**, 83–116 (2011).
2. Sreenivasan, S. Nanoscale manufacturing enabled by imprint lithography. *MRS BULLETIN* **33**, 854–863 (2008).
3. Glangchai, L. C., Caldorera-Moore, M., Shi, L. & Roy, K. Nanoimprint lithography based fabrication of shape-specific, enzymatically-triggered smart nanoparticles. *Journal of Controlled Release* **125**, 263–272 (2008).
4. Naughton M. J. *et al.* Efficient nanocoax-based solar cells. *physica status solidi (RRL)* **4**, 181–183 (2010).
5. Battaglia, C. *et al.* Nanoimprint Lithography for High-Efficiency Thin-Film Silicon Solar Cells. *Nano Letters* doi:10.1021/nl1037787
6. Huang, R. & Zhu, J. Silicon nanowire array films as advanced anode materials for lithium-ion batteries. *Materials Chemistry and Physics* **121**, 519–522 (2010).
7. Ling, M. M. & Bao, Z. Thin Film Deposition, Patterning, and Printing in Organic Thin Film Transistors. *Chem. Mater.* **16**, 4824–4840 (2011).
8. Jung, J.-Y., Kang, Y. T. & Koo, J. Development of a new simulation model of spin coating process and its application to optimize the 450 mm wafer coating process. *International Journal of Heat and Mass Transfer* **53**, 1712–1717 (2010).
9. Cecchi, M., Smith, H. & Braun, D. Method to optimize polymer film spin coating for polymer LED displays. *Synthetic Metals* **121**, 1715–1716 (2001).
10. Yonkoski, R. K. & Soane, D. S. Model for spin coating in microelectronic applications. *J. Appl. Phys.* **72**, 725 (1992).
11. Kim, S.-K., Yoo, J.-Y. & Oh, H.-K. Resist distribution effect of spin coating. *J. Vac. Sci. Technol. B* **20**, 2206 (2002).
12. Perçin, G., Lundgren, T. S. & Khuri-Yakub, B. T. Controlled ink-jet printing and deposition of organic polymers and solid particles. *Applied Physics Letters* **73**, 2375 (1998).
13. Lin, M. W. *et al.* Planarization for reverse-tone step and flash imprint lithography. *Emerging Lithographic Technologies X* **6151**, 61512G–12 (2006).
14. Hoth, C. N. *et al.* Topographical and morphological aspects of spray coated organic photovoltaics. *Organic Electronics* **10**, 587–593 (2009).
15. Sukanek, P. C. A Model for Spin Coating with Topography. *J. Electrochem. Soc.* **136**, 3019–3026 (1989).
16. PEURRUNG, L. & GRAVES, D. FILM THICKNESS PROFILES OVER TOPOGRAPHY IN SPIN COATING. *JOURNAL OF THE ELECTROCHEMICAL SOCIETY* **138**, 2115–2124 (1991).
17. Singh, M., Haverinen, H. M., Dhagat, P. & Jabbour, G. E. Inkjet Printing—Process and Its Applications. *Advanced Materials* **22**, 673–685 (2010).
18. Tekin, E., Smith, P. J. & Schubert, U. S. Inkjet printing as a deposition and patterning tool for polymers and inorganic particles. *Soft Matter* **4**, 703–713 (2008).
19. Tekin, E., de Gans, B.-J. & Schubert, U. S. Ink-jet printing of polymers ? from single dots to thin film libraries. *J. Mater. Chem.* **14**, 2627 (2004).
20. Olziersky, A., Vila, A. & Morante, J. R. Multicomponent oxide thin-film transistors fabricated by a double-layer inkjet printing process. *Thin Solid Films* doi:10.1016/j.tsf.2011.04.149

21. Ren, M., Gorter, H., Michels, J. & Andriessen, R. Ink-Jet Technology for Large Area Organic Light-Emitting Diode and Organic Photovoltaic Applications. *Journal of Imaging Science and Technology* **55**, 040301-1 – 040301-6 (2011).
22. Krebs, F. C. Fabrication and processing of polymer solar cells: a review of printing and coating techniques. *Solar Energy Materials and Solar Cells* **93**, 394–412 (2009).
23. Krebs, F. Polymer solar cell modules prepared using roll-to-roll methods: Knife-over-edge coating, slot-die coating and screen printing. *SOLAR ENERGY MATERIALS AND SOLAR CELLS* **93**, 465–475 (2009).
24. Stafford, C. M., Roskov, K. E., Epps, T. H. & Fasolka, M. J. Generating thickness gradients of thin polymer films via flow coating. *Review of Scientific Instruments* **77**, 023908–023908–7 (2006).
25. Ashley, K. M., Carson Meredith, J., Amis, E., Raghavan, D. & Karim, A. Combinatorial investigation of dewetting: polystyrene thin films on gradient hydrophilic surfaces. *Polymer* **44**, 769–772 (2003).
26. Turcu, F. *et al.* Ink-Jet Microdispensing for the Formation of Gradients of Immobilised Enzyme Activity, Ink-Jet Microdispensing for the Formation of Gradients of Immobilised Enzyme Activity. *Macromolecular Rapid Communications, Macromolecular Rapid Communications* **26**, **26**, 325, 325–330, 330 (2005).
27. Ratcliff, E. L. & Hillier, A. C. Directed Electrodeposition of Polymer Films Using Spatially Controllable Electric Field Gradients. *Langmuir* **23**, 9905–9910 (2007).
28. Nolte, A. J. *et al.* Thin Film Thickness Gradients and Spatial Patterning via Salt Etching of Polyelectrolyte Multilayers. *Macromolecules* **40**, 5479–5486 (2007).
29. Genzer, J. *Soft Matter Gradient Surfaces: Methods and Applications*. (John Wiley & Sons: 2012).
30. Boudou, T., Crouzier, T., Ren, K., Blin, G. & Picart, C. Multiple Functionalities of Polyelectrolyte Multilayer Films: New Biomedical Applications. *Advanced Materials* **22**, 441–467 (2010).
31. Liu, Y., Klep, V., Zdyrko, B. & Luzinov, I. Synthesis of High-Density Grafted Polymer Layers with Thickness and Grafting Density Gradients. *Langmuir* **21**, 11806–11813 (2005).
32. Liu, C. *et al.* Profile coatings and their applications. *Journal of Vacuum Science & Technology A: Vacuum, Surfaces, and Films* **21**, 1579 (2003).
33. Alcock, S. G. & Cockerton, S. A preferential coating technique for fabricating large, high quality optics. *Nuclear Instruments and Methods in Physics Research Section A: Accelerators, Spectrometers, Detectors and Associated Equipment* **616**, 110–114 (2010).
34. Handa, S. *et al.* Highly accurate differential deposition for X-ray reflective optics. *Surface and Interface Analysis* **40**, 1019–1022 (2008).
35. Yumoto, H. *et al.* Fabrication of elliptically figured mirror for focusing hard x rays to size less than 50 nm. *Review of Scientific Instruments* **76**, 063708–063708–5 (2005).
36. Raymond A., A. Intentionally patterned and spatially non-uniform film profiles in chemical vapor deposition processes. *Surface and Coatings Technology* **201**, 9025–9029 (2007).
37. Colburn, M. *et al.* Step and flash imprint lithography for sub-100-nm patterning. *Proceedings of SPIE* **3997**, 453 (2000).
38. Dong, H., Carr, W. W. & Morris, J. F. An experimental study of drop-on-demand drop formation. *Phys. Fluids* **18**, 072102 (2006).
39. Liang, X., Tan, H., Fu, Z. & Chou, S. Air bubble formation and dissolution in dispensing nanoimprint lithography. *NANOTECHNOLOGY* **18**, (2007).

40. Steinhaus, B., Spicer, P. T. & Shen, A. Q. Droplet Size Effects on Film Drainage between Droplet and Substrate. *Langmuir* **22**, 5308–5313 (2006).
41. Savva, N. & Kalliadasis, S. Two-dimensional droplet spreading over topographical substrates. *Phys. Fluids* **21**, 092102–16 (2009).
42. Eggers, J. Contact line motion for partially wetting fluids. *Phys. Rev. E* **72**, (2005).
43. Shikhmurzaev, Y. D. Singularities at the moving contact line. Mathematical, physical and computational aspects. *Physica D: Nonlinear Phenomena* **217**, 121–133 (2006).
44. Reddy, S. & Bonnacaze, R. Simulation of fluid flow in the step and flash imprint lithography process. *MICROELECTRONIC ENGINEERING* **82**, 60–70 (2005).
45. Müller, T. *et al.* Techniques for analysing nanotopography on polished silicon wafers. *Microelectronic Engineering* **56**, 123–127 (2001).
46. Boning, D. & Lee, B. Nanotopography issues in shallow trench isolation CMP. *MRS Bulletin(USA)* **27**, 761–765 (2002).
47. Sakdinawat, A. & Attwood, D. Nanoscale X-ray imaging. *Nat Photon* **4**, 840–848 (2010).
48. Pivovarov, M. J. *et al.* Small-animal radionuclide imaging with focusing gamma-ray optics. *Proceedings of SPIE* **5199**, 147–161 (2004).
49. Bergemann, C., Keymeulen, H. & van der Veen, J. F. Focusing X-Ray Beams to Nanometer Dimensions. *Phys. Rev. Lett.* **91**, 204801 (2003).
50. Mimura, H. *et al.* Breaking the 10[thinsp]nm barrier in hard-X-ray focusing. *Nat Phys* **6**, 122–125 (2010).
51. Morawe, C., Guigay, J.-P., Mocella, V. & Ferrero, C. An analytical approach to estimating aberrations in curved multilayer optics for hard x-rays: 2. Interpretation and application to focusing experiments. *Opt. Express* **16**, 16138–16150 (2008).
52. Gubarev, M. V., Kilaru, K. & Ramsey, B. D. An investigation of differential deposition for figure corrections in full-shell grazing-incidence X-ray optics. *Nuclear Instruments and Methods in Physics Research Section A: Accelerators, Spectrometers, Detectors and Associated Equipment* **616**, 273–276 (2010).
53. Kilaru, K., Ramsey, B. D. & Gubarev, M. V. Development of differential deposition technique for figure corrections in grazing incidence x-ray optics. *Proceedings of SPIE* **7437**, 743719–743719–9 (2009).
54. Tosaka, A., Sakai, Y., Tsuru, T. & Yamamoto, M. Development of an Ion Milling System for Figure Error Correction of a Soft X-ray Multilayer Mirror. *Journal of the Vacuum Society of Japan* **51**, 115–117 (2008).
55. Ice, G. E., Chung, J.-S., Tischler, J. Z., Lunt, A. & Assoufid, L. Elliptical x-ray microprobe mirrors by differential deposition. *Review of Scientific Instruments* **71**, 2635–2639 (2000).
56. Bakshi, V. *EUV lithography*. (SPIE Press: 2008).
57. Rizvi, S. *Handbook of photomask manufacturing technology*. (CRC Press: 2005).
58. Hector, S. & Mangat, P. Review of progress in extreme ultraviolet lithography masks. *The 45th international conference on electron, ion, and photon beam technology and nanofabrication* **19**, 2612–2616 (2001).
59. Madou, M. J. *Fundamentals of microfabrication*. (CRC Press: 2002).
60. Chang, A. *et al.* Nanoimprint planarization of high aspect ratio nanostructures using inorganic and organic resist materials. *JOURNAL OF VACUUM SCIENCE & TECHNOLOGY B* **27**, 2877–2881 (2009).
61. Büyükköse, S., Vratzov, B. & van der Wiel, W. G. High-quality global hydrogen silsequioxane contact planarization for nanoimprint lithography. *Journal of Vacuum Science & Technology B: Microelectronics and Nanometer Structures* **29**, 021602 (2011).

62. Shih, W.-S., Neef, C. J. & Daffron, M. G. A planarization process for multilayer lithography applications. *Advances in Resist Technology and Processing XXI* **5376**, 664–672 (2004).
63. Prybyla, J. A. Device fabrication involving surface planarization. (2000).
64. Shih, W.-S., Yota, J. & Itchhaporia, K. CON-TACT Planarization Process of Spin-on Dielectrics for Device Fabrication. *J. Electrochem. Soc.* **155**, G65–G71 (2008).
65. Reddy, S., Schunk, P. & Bonnecaze, R. Dynamics of low capillary number interfaces moving through sharp features. *PHYSICS OF FLUIDS* **17**, (2005).
66. Colburn, M., Choi, B., Sreenivasan, S., Bonnecaze, R. & Willson, C. Ramifications of lubrication theory on imprint lithography. *MICROELECTRONIC ENGINEERING* **75**, 321–329 (2004).
67. Ventsel, E. & Krauthammer, T. *Thin plates and shells*. (CRC Press: 2001).
68. ROY, R. V., ROBERTS, A. J. & SIMPSON, M. E. A Lubrication Model of Coating Flows Over a Curved Substrate in Space. *Journal of Fluid Mechanics* **454**, 235–261 (2002).
69. KIM, H.-Y. & MAHADEVAN, L. Capillary Rise Between Elastic Sheets. *Journal of Fluid Mechanics* **548**, 141–150 (2006).
70. Py, C. *et al.* Capillary Origami: Spontaneous wrapping of a droplet with an elastic sheet. *PHYSICAL REVIEW LETTERS* **98**, (2007).
71. Py, C. *et al.* Capillarity induced folding of elastic sheets. *The European Physical Journal - Special Topics* **166**, 67–71 (2009).
72. Kwon, H., Kim, H., Puell, J. & Mahadevan, L. Equilibrium of an elastically confined liquid drop. *JOURNAL OF APPLIED PHYSICS* **103**, (2008).
73. de Langre, E., Baroud, C. N. & Reverdy, P. Energy criteria for elasto-capillary wrapping.
74. Flitton, J. & King, J. Moving-boundary and fixed-domain problems for a sixth-order thin-film equation. *EUROPEAN JOURNAL OF APPLIED MATHEMATICS* **15**, 713–754 (2004).
75. Verma, R., Sharma, A., Banerjee, I. & Kargupta, K. Spinodal instability and pattern formation in thin liquid films confined between two plates. *JOURNAL OF COLLOID AND INTERFACE SCIENCE* **296**, 220–232 (2006).
76. Sellier, M. Substrate design or reconstruction from free surface data for thin film flows. *Phys. Fluids* **20**, 062106–4 (2008).
77. Sellier, M. & Panda, S. Beating capillarity in thin film flows. *INTERNATIONAL JOURNAL FOR NUMERICAL METHODS IN FLUIDS* **63**, 431–448 (2010).
78. Heining, C. & Aksel, N. Bottom reconstruction in thin-film flow over topography: Steady solution and linear stability. *Phys. Fluids* **21**, 083605–10 (2009).
79. Kalliadasis, S., Bielarz, C. & Homsy, G. Steady free-surface thin film flows over topography. *PHYSICS OF FLUIDS* **12**, 1889–1898 (2000).
80. Khayat, R. & Welke, S. Influence of inertia, gravity, and substrate topography on the two-dimensional transient coating flow of a thin Newtonian fluid film. *PHYSICS OF FLUIDS* **13**, 355–367 (2001).
81. Mazouchi, A. & Homsy, G. M. Free surface Stokes flow over topography. *Phys. Fluids* **13**, 2751 (2001).
82. DECREÉ, M. M. J. & BARET, J.-C. Gravity-Driven Flows of Viscous Liquids Over Two-Dimensional Topographies. *Journal of Fluid Mechanics* **487**, 147–166 (2003).
83. Sreenivasan, S. V. *et al.* Step and repeat imprint lithography processes. (2010).at <http://www.google.com/patents/about/7727453_Step_and_repeat_imprint_lithogra.html?id=G1vnAAAAEBAJ>
84. Alleborn, N. & Raszillier, H. Local perturbation of thin film flow. *ARCHIVE OF APPLIED MECHANICS* **73**, 734–751 (2004).

85. Moin, P. *Fundamentals of Engineering Numerical Analysis*. (Cambridge University Press: 2010).
86. Fornberg, B. *A Practical Guide to Pseudospectral Methods*. (Cambridge University Press: 1998).
87. Coleman, H. W. & Steele, W. G. *Experimentation, validation, and uncertainty analysis for engineers*. (John Wiley and Sons: 2009).
88. Panga, A. Adaptive Imprint Planarization. (2008).
89. Chen, D. Anti-reflection (AR) coatings made by sol-gel processes: A review. *Solar Energy Materials and Solar Cells* **68**, 313–336 (2001).
90. Park, E.-M. *et al.* Investigation of the effects of bottom anti-reflective coating on nanoscale patterns by laser interference lithography. *Thin Solid Films* **519**, 4220–4224 (2011).
91. Hiller, J., Mendelsohn, J. D. & Rubner, M. F. Reversibly erasable nanoporous anti-reflection coatings from polyelectrolyte multilayers. *Nat Mater* **1**, 59–63 (2002).
92. Shikhmurzaev, Y. D. *Capillary Flows with Forming Interfaces*. (Chapman & Hall/CRC: 2007).
93. Friedl, N., Rammerstorfer, F. G. & Fischer, F. D. Buckling of stretched strips. *Computers & Structures* **78**, 185–190 (2000).
94. Jacques, N., Elias, A., Potier-Ferry, M. & Zahrouni, H. Buckling and wrinkling during strip conveying in processing lines. *Journal of Materials Processing Technology* **190**, 33–40 (2007).
95. Zhang, T. Scanner Dose and Illumination Control in Nano-Lithography. (2011).
96. Mamedov, A. A., Belov, A., Giersig, M., Mamedova, N. N. & Kotov, N. A. Nanorainbows: Graded Semiconductor Films from Quantum Dots. *Journal of the American Chemical Society* **123**, 7738–7739 (2001).